Design and fabrication of Mems-based, vibration powered energy harvesting device using electrostatic transduction

Ayyaz Mahmood Paracha

UNIVERSITÉ PARIS-EST

UNIVERSITÉ PARIS-EST

ÉCOLE DOCTORALE

Thèse de doctorat

Electronique, Optronique et Systèmes (CNU 63)

Ayyaz MAHMOOD PARACHA

Conception et réalisation d'un micro-système pour la récupération de l'énergie vibratoire du milieu ambiant par transduction électrostatique

Thèse dirigée par
M. Tarik BOUROUINA
et suivie par
M. Philippe BASSET

Soutenue le 11/12/2009

Jury :

Jean-Marc LAHEURTE	Professeur, Université de Paris – Est, MLV	Président
Skandar BASROUR	Professeur, UJF, TIMA	Rapporteur
Carole ROSSI	Chargé de rechercher CNRS LAAS	Rapporteur
Fabrice VERJUS	Président CAPVRF	Examinateur
Dimitri GALAYKO	Maître de conférence, Université de Paris 6	Invité
Tarik BOUROUINA	Professeur, ESIEE, Paris	Directeur
Philippe BASSET	Professeur associé, ESIEE, Paris	Co-encadrent

Acknowledgements

My utmost gratitude goes to my thesis advisor, ***Prof. Tarik BOUROUINA*** *for allowing me to join his team, for his expertise, kindness, and most of all, for his patience. I believe that one of the main gains of this 4-years program was working with him.*

My special thanks are for my thesis supervisor ***Dr. Philippe BASSET****, his continuous help, proposals, data handling and analysis, reviewing my research manuscripts and for his friendly attitude. Without his help, guidance and cooperation nothing was possible. His patient explanations were the key to the successful finish of this research work. One of my biggest gains during this research work is the professional experience I gained with him. I am really thankful to you for all.*

I would like to thank my thesis manuscript reviewers, ***Prof. Skandar BASROUR*** *and* ***Prof. Carole ROSSI*** *to give a time read my manuscript. Special thanks to* ***Dr. Fabrice VERJUS*** *and* ***Prof. Jean-Marc LAHEURTE*** *to become a part of my defence jury.*

I am also grateful to ***Dr. Dimitri GALAYKO*** *for guiding me continuously with the patience and friendly attitude during the last year of my thesis.*

My thanks and appreciation also goes to ***Prof. Odile PICON*** *for her dedicated and continues support since my masters*

I wish to express my warm and sincere thanks to ***Mr. Frederic MARTY*** *for his expertise, and help in clean room and especially in DRIE. Fred I am really thankful and grateful to you, the way you have always helped me with a smiling face.*

I also like to thanks to ***Kamran, Lionel, Bruno M., Patrick, Sylvie, Pascal, Serge and Bruno C.*** *to be there whenever I needed them in clean room. To work with* ***SMM*** *is one of the wonderful experiences of life.*

I am also thankful to the members of ***ELMI****,* ***Yeves, Laurie, Anne, Patrick P., Patrick S., and Corrine*** *for their help and support. I am greatly indebted to three persons who helped me a lot in my research and teaching career a lot,* ***Lionel, Laure*** *and* ***Gilles****. I can never forget the help you guys have always provided me. I like to thank and wish all the best to my other PhD colleagues* ***Jaya, Kinda and Kim.***

I like to thank ***Dr. Vinod KUMAR*** *of Alcatel and Université de Paris Est. His guidance turned my life and gave me new dimension. I can never forget your advices and helps during masters.*

In Pakistan and France I saw many friends with whom I had some wonderful times. I just want to mention their names and thank them. Ahsan, Tuaha, Shahbaz, Sheraz, Ali Anwar, Aurangzeb, Thao, Rahim, Shehla, Cheema, Kamel, Farhan, Aamer Khan, Rizvi, Faiz, Sohail, Hassan, Mirza, Kaku, Ghufran bhai, Aamer bhai, Mahwish bhabhi, Abdullah, Bushra, Kashif, Abdelhamid etc... I am sorry if I forget any one name. I am thankful to all of you for your continuous guidance, support, help in very difficult periods of life. I love you all and wish you all the best for future.

I also want to thanks my company colleagues from "PROGIS", for supporting me a lot during the last six months.

Above all, I thank my dad, mom, grand mother and sis Rabia for their love and help.

I also want to thank my fiancée Nadia, I love you a lot!!

In the end my special thanks to my God for giving me everything in life.

Résumé

Avec la réduction de l'énergie consommée par les capteurs miniatures, a émergé le nouveau concept de capteurs autonomes. Il s'agit de capteurs dont l'alimentation ne dépend pas d'une source embarquée de type batterie, dont la durée de vie est limitée. Ils ont en effet la capacité de puiser l'énergie nécessaire à leur fonctionnement à partir de l'environnement dans lequel ils se trouvent. Ce concept présente de nombreux avantages, notamment la diminution des coûts de maintenance des capteurs par l'absence d'une nécessité de remplacement des piles et par conséquent une facilité accrue du déploiement des réseaux de capteurs sans fil.

Parmi les sources d'énergie envisageables, les vibrations mécaniques ambiantes comptent parmi les plus prometteuses puisqu'elles sont présentes dans un grand nombre de structures : véhicules, avions, bâtiments, etc. La conversion des vibrations mécaniques en énergie électrique est réalisée en deux étapes. Dans un premier temps, un résonateur mécanique, constitué d'une masse mobile associée à un ressort, est couplé avec les vibrations de l'environnement. Grâce à ce couplage, la masse oscille dans le système de référence et accumule une énergie mécanique. La deuxième étape est la conversion de cette énergie en énergie électrique. Un transducteur électromécanique est le siège d'une force d'amortissement sur la masse en résonance, et effectue donc un travail négatif sur le système mécanique.

Notre choix de transducteur électromécanique s'est arrêté sur les transducteurs électrostatiques et piézoélectriques car ils présentent l'avantage d'être compatibilité avec le procédé CMOS et adaptés à la miniaturisation. Nous avons ensuite conçu et fabriqué un transducteur électrostatique utilisant une technologie silicium verre, qui a nécessité le développement d'un procédé *ad hoc* de gravure DRIE. Le dispositif a été testé en utilisant un circuit électronique de type pompe de charge. Nous avons obtenu une conversion d'énergie mécanique en énergie électrique de 61 nW au moyen d'un dispositif dont la surface est de

seulement 66 mm², la sollicitation vibratoire étant à la fréquence de résonance mécanique de la microstructure, qui est de 250 Hz et avec une accélération externe de 0,25 g ainsi qu'une tension initiale de 6V. Le résultat a été confronté avec des simulations effectuées sur la base d'un modèle VHDL-AMS. L'écart avec les mesures est inférieur à 3%. Ce dispositif est le premier convertisseur miniature d'énergie basé sur une transduction électrostatique, fabriqué dans un procédé collectif à base de silicium et sans l'adjonction d'un électret. Afin de procéder à une comparaison pertinente de notre travail avec les autres dispositifs rapportés dans la littérature et qui utilisent la transduction électrostatique, nous proposons une nouvelle figure de mérite (FOM) définie comme une puissance convertie normalisée. Bien que l'état de l'art actuel montre que notre réalisation présente l'un des meilleurs facteurs de mérite, la puissance produite n'est cependant pas suffisante pour alimenter un microsystème réel, à cause notamment d'une tension de « pull-in » trop basse. Quelques pistes d'amélioration sont proposées, notamment l'exploitation de non-linéarités mécaniques pour augmenter la bande passante du spectre énergétique exploitable par le micro-dispositif.

Table of contents

List of figures

Chapter 3: Fabrication and characterization of the energy harvester…..…65

List of tables

List of abbreviations

IC..... Integrated Circuit
CVD..... Chemical Vapor Deposition
PVD..... Physical Vapor Deposition
VLSI..... Very Large Scale Integration
TPMS ..... Tire Pressure Monitoring System
VDRG .....Velocity Damped Resonant Generator
CDRG .....Coulomb Damped Resonant Generator
CFPG .....Coulomb Force Parametric Generator
IPOC .....In-Plane Overlap Comb
IPGC .....In-Plane Gap-closing Comb
OPGP..... Out-of-Plane Gap-closing Plate
IPOP .....In-Plane Overlap Plates
DRIE .....Deep Reactive Ion Etching
PC..... Proof mass Configuration
CC .....Comb Configuration
HF..... Hydrofluoric acid
PECVD..... Plasma Enhanced Chemical Vapor Deposition
RIE ..... Reactive Ion Etching
ICP..... Inductively Coupled Plasma
RF..... Radio frequency
LF..... Low frequency
CD .....Critical Dimension
ARDE .....Aspect Ratio Dependent Etching

Chapter 1
Introduction to energy harvesting

In the middle of the 20th century, electronics industry had been revolutionized with the discovery of Integrated Circuits (ICs). Two main advantages of ICs over discrete circuits are cost and performance. Fabrication cost is low as the chips are fabricated collectively. Performance is high since the components switch quickly and consume little power due to their small size. From 1947 to 2007 the area of the IC chip and the obtainable minimum feature size due to the fabrication technology shrinks, along with a huge increase in number of transistors per mm². In 1971 *INTEL*^{tm} released 4004 processor whose manufacturing technology was 10 μm and it contained 2300 transistors, where as they released dual core Xeon using 65 nm manufacturing technology containing 820,000,000 transistors [1]. The electronics are fabricated using the IC process sequences (e.g., CMOS, Bipolar, or BICMOS processes).

The CMOS fabrication process consists basically of three fundamental steps which are:

1) *Deposition* of thin film materials either chemically (CVD) or physically (PVD) or even by *Doping* the semiconductor surface by controlled introduction of impurities.

2) *Photolithography* for patterning at the micro-scale

3) *Etching,* which can be either dry (Plasma etching) or wet etching

Micro-Electro-Mechanical Systems (MEMS) is a step forward from the IC technology. It is the integration of micro-mechanical structures, on a silicon substrate through micro-fabrication techniques, i.e. "micromachining" processes. An industrial motivation is to process these MEMS structures with the IC technologies to improve cost factor. Various works have also been reported in order to integrate both the CMOS with the MEMS together in the same fabrication process [2]. Apart from IC fabrication steps, MEMS fabrication also involves the micro machining processes, which are basically of two types:

1) *Surface micro machining*: To etch different structural layers deposited on the top of the silicon substrate to produce thin freestanding movable micro-structures.
2) *Bulk micro machining*: The process where selective areas of the silicon substrate are etched through the bulk silicon substrate to produce the movable mechanical structures within the substrate volume.

Fig. 1.1 reports the business turnover by the MEMS based devices in the recent years and the prediction of the MEMS market for couple of coming years. This graph shows the business around $6 billion in 2006 with a 14% annual growth [3]. Three major consumer applications in the market are inkjet heads, pressure sensors and MEMS based μ-displays. The future of other MEMS-based applications, related to RF-MEMS, μ-Fluidics, Optical MEMS, inertial MEMS (gyroscopes and accelerometers) and silicon-based microphones in the market also looks quiet promising, as the demand of these applications is increasing with every passing year. The presence of μ-Fuel cells as one of the promising businesses in the MEMS industry shows the need for the power sources at the micro scale. For the time being the vibration powered energy harvesters do not exist in the MEMS market, but one can become optimistic about their future by looking how other MEMS sensors applications like gyroscopes and accelerometers make their way in the business in the recent past. To further

continue their deployment successfully, MEMS sensors in general will definitely require a source of energy of reduced dimensions.

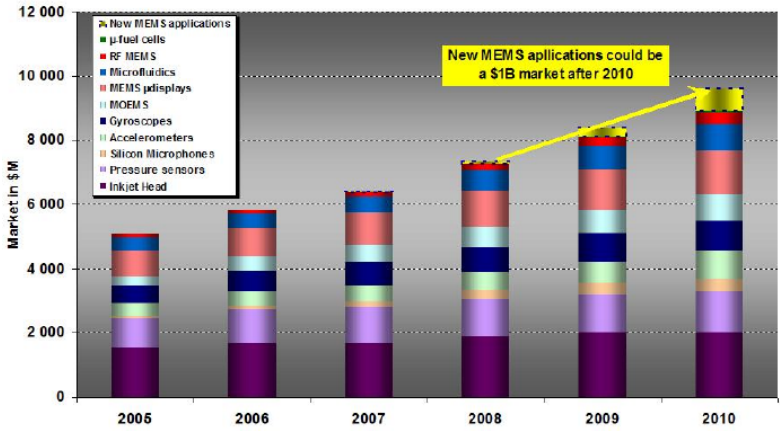

Fig. 1.1 Study report of yole development about the MEMS market [3]

This chapter presents an introduction of renewable energy resources, mechanically powered energy scavengers, reported vibrations powered electrostatic based energy harvesters having a power rating from few nano to milli Watts range and finally a novelty of the fabricated device with respect to the existing ones.

1.1 Renewable energy resources

One form of energy can be converted into another form. Naturally, energy exists in many forms like wind, solar, hydraulic, thermal, tidal energies etc… Renewable energy is defined as electrical energy generated from these natural resources. In year 2006, the non-negligible ratio of 18% of global power consumption came from the renewable power sector [4]. Fig. 1.2 shows some of the renewable energy resources used for the power generation from Mega-Watts to Nano-Watts range to energize various appliances. The figure has been divided in three sections based upon the generated power ratings which further depend upon the desired applications i.e.

1) Mega-watt power generation sources

2) Milli-watt to micro watt power generation sources

3) Sources based on nanotechnologies

1.1.1 Megawatts applications

These power resources supply the power needs for domestic uses in residential areas and industrial applications. Three shown renewable energy resources are hydraulic energy, solar panels (light energy) and wind energy. One of the most considered ways is a ***hydropower*** i.e. the generation of electricity by using the gravitational force of falling water. The hydroelectric power is converted by the potential energy of water stored in a reservoir (called as dam) at certain height. When water is allowed to fall from such a height, it drives a water turbine and generator. In this case the energy extracted from the water depends on the height of the water stored.

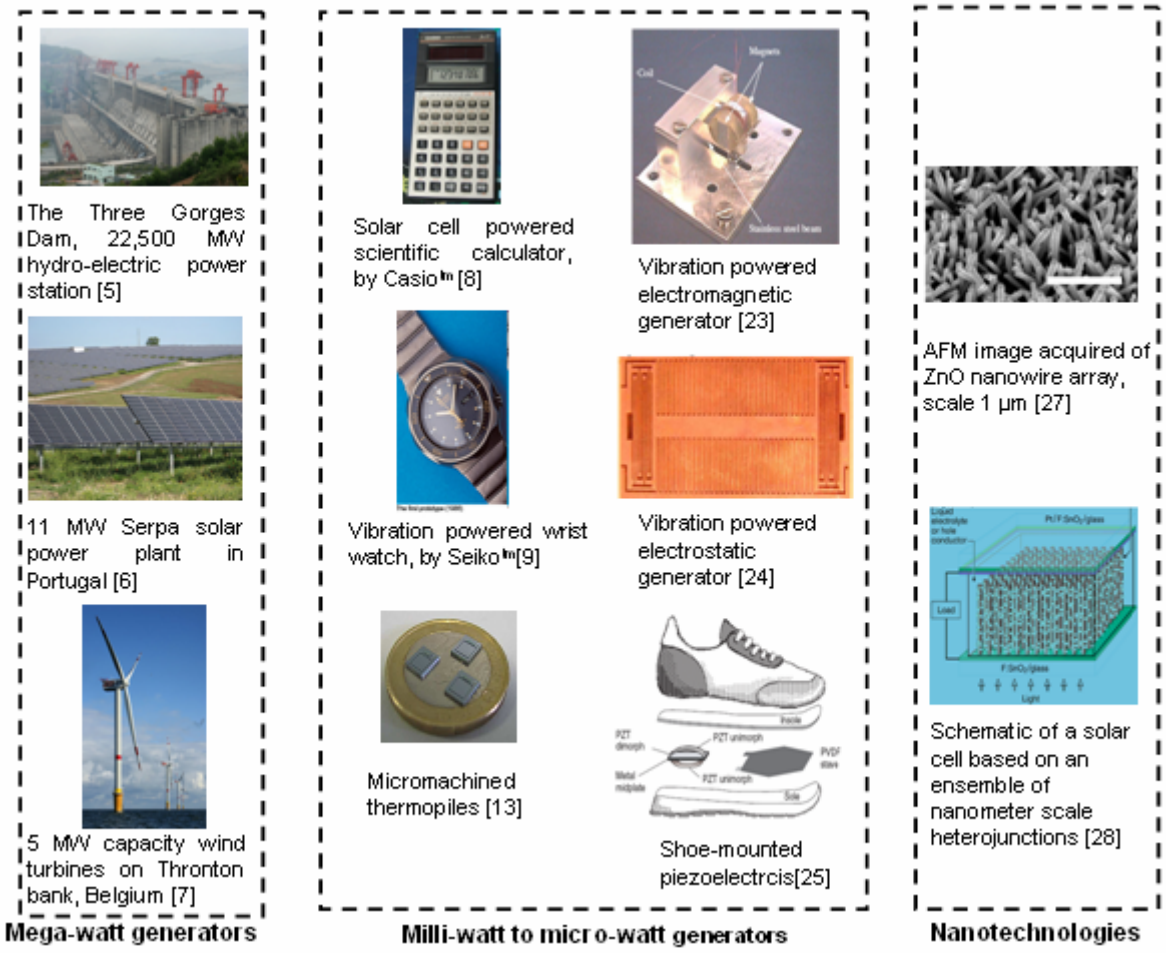

Fig.1.2 Some existing renewable energy resources, divided in three blocks

The hydro-electric power station shown in the Fig. 1.2 is "The Three Gorges Dam", the largest hydro-electric power station in the world. This dam will be fully operational until 2011 and the total electric generating capacity of the dam will reach 22,500 MW [5]. Other renewable energy resource which is being widely used in commercial sector is the ***solar energy***. Solar cell works on the principle of photovoltaic effect. Photons of sunlight hit the solar panel (a combination of various solar cells) and are absorbed by semiconductor materials, such as silicon, within PN junctions. Hence electron-hole pairs are generated within the PN junction, allowing these electrical charge carriers to flow through the material to produce electricity. Fig. 1.2 shows the Serpa power plant used to generate 11 MW power in Portugal [6]. Apart from these two, another renewable energy resource is the ***wind energy***. Most of the energy stored in these wind movements can be found at high altitudes where continuous wind speeds of over 160 km/h (100 mph) occur. These winds can be utilized for the power generation using wind turbines. They convert kinetic energy of the wind into mechanical energy by rotational motion. This converted mechanical energy is converted into electrical energy, by using this energy to energize electricity generator. Fig. 1.2 shows three of the sixty 5 MW each capacity windy turbines. These 60 × 5MW turbines are constructed on the Thornton bank and have been linked to the Belgian power grid [7].

1.1.2 Milliwatt to microwatt applications

There exist certain low power applications in the market, like calculator and wrist watches, which get powered from the renewable energy resources. The calculators are powered by the ***solar cells*** which work on the photovoltaic principle as explained above. Human body is also the renewable source of energy as it generates heat energy and performs mechanical activities. The automatic watches are powered using these two types of energies from human wrist. The mechanical powered wrist watches contain semicircular rotor that

turns on a pivot, within the watch case. The normal movements of the user's arm and wrist cause the rotor to pivot back-and-forth, which is attached to a ratcheted winding mechanism. The motion of the wearer's arm is thereby translated into the circular motion of the rotor that through a series of mechanical gears, eventually winds the mainspring [10, 11]. The heat energy can also be used to generate the electric energy using ***thermoelectric effect***. The thermoelectric effect is a conversion of temperature differences (gradients) to electrical voltage. This phenomenon can be understood on the atomic scale: If a temperature difference is created it causes charged carriers in the material, to diffuse from the side having high temperature to the lower temperature, hence an electrical current is thermally-induced [12, 13]. The charge carriers can be electrons or holes. The heat energy flow from the surface of the skin is also used to power the wrist watches [11].

Apart from these applications, there are other applications to miniature devices which require renewable energy resources. These applications include MEMS-based sensors like pressure sensors, temperature sensors etc… During the past decade, efforts have been made to reduce the power consumption of sensors and the Very Large Scale Integration (VLSI) design. It is expected that power consumption for these applications will be reduced from tens of *mWs* to a few μWs. Reference [14] gives a review of different reported works about the decrease in power consumption of various applications (cf. ref. Fig. 1.3). The decreases in sensors power consumption highlight the concept of autonomous sensors i.e. to make them independent of externally attached power sources, by generating electrical energy from the renewable energy resources. Various techniques of harvesting energy from the environment to energize these sensors have been studied [15-17]. This concept can be helpful in many ways:

1) It reduces the bunch of wires used for the electrical connections in between the power source and different sensors, thus facilitating the deployment of wireless sensors,
2) Device's lifetime increases as compared to the limited lifetime when using batteries,
3) Cost maintenance decreases as there is no need to replace the external batteries.
4) In addition, environmental polluting chemical materials can be reduced or even eliminated.

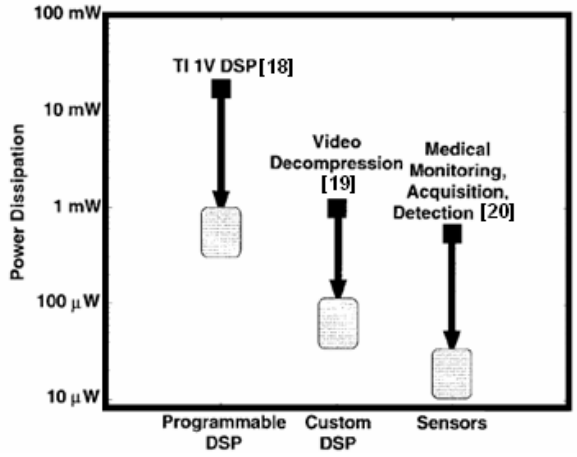

Fig.1.3 Reported reduced power consumption in various applications [14]

This concept can be extremely useful in order to provide autonomous nodes in the distributed sensor networks (cf. ref Fig. 1.4). Each node consists of a sensor, a chip-size antenna [21], an IC and a power source (the vibration-to-electricity converter can be the power source for nodes). The sensor senses the environment, and sends the data towards main control server via antenna. The ICs performs signal conditioning of the sensor and RFID/ZigBee tagging. Fig. 1.5 shows various sensors present in the car [22]. They all are connected to the car's battery. There micro machined transducers can be taken as distributed sensor network where renewable energy resources like mechanical vibrations, solar light, thermal energies etc… can be used to power these sensors.

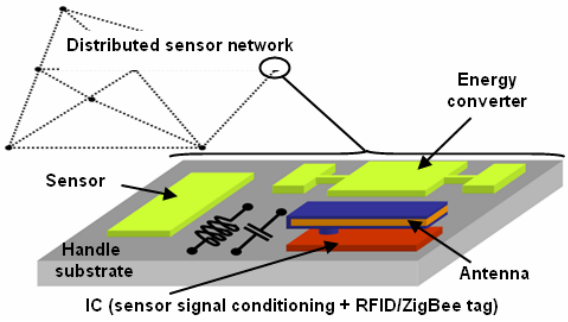

Fig. 1.4 The vibration-to-electricity converter takes the place of the power source for nodes in a distributed network. Each node includes a sensor, a chip-size antenna [21] and an IC.

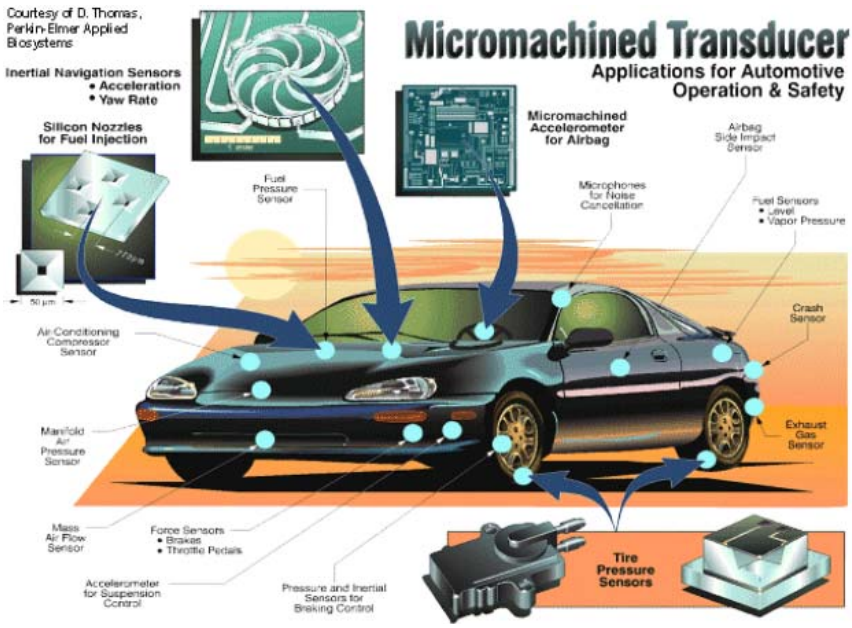

Fig. 1.5 Micro machined transducers present in the automotive applications [22]

1.1.3 Nanotechnologies

Along with the MEMS-based energy harvesting prototypes, the nanotechnologies based solutions (having size between molecular and microscopic dimensions) are also being presented. In this emerging technology, the piezoelectric (vibration powered) and photovoltaic effect (light energy) based ideas and some other implementations are being presented using nano-wires [26-28]. A nanowire is a wire having the diameter of the order of a nanometer (10^{-9} meters). The fabrication of nano pillars of ZnO uses nano-fabrication techniques, which combine different methods of lithography, etching, growth, CVD and electroplating, electron beam lithography, ion beam, nanoimprint [29], etc…

Nanostructures are of high interest in general due to their unique properties resulting namely from their favorable (very high) surface to volume ratio, ease of stress relaxation and confinement effects, which impact on their electrical, thermal and optical transport properties.

When considering production of energy, nanostructures including nanowires in particular, have already demonstrated their superior performances when integrated in micro fuel-cells or in Lithium batteries. Beside their superior performances, nanowires provide an economical interest because they are good candidates for the substitution of the high-cost platinum catalysts.

In the area of vibration based energy harvesting, recent reports from Yang et al. [30, 31] gave the evidence of producing a voltage of 10 mV through the deformation (by an AFM probe) of a single ZnO nanowire, which appear to exhibit extraordinary piezoelectric properties. According to this result, and when considering a dense array of ZnO nanowires, it is theoretically possible to obtain a power density of up to 10 mW/cm^2.

When considering the foreseeable extinction of fossil resources, solutions based on energy scavenging appear *a priori* more promising than the alternatives based on micro fuel-cells. Furthermore, regarding the theoretical predictions, solutions based on nanotechnologies will certainly take the lead.

1.1.4 Discussion

We have made a brief review of various renewable energy resources from Megawatts to Nanowatts. Small size renewable energy resources are already used to energize portable applications (wrist watches and calculators), making them fully autonomous. Further successful implementation of the miniaturized renewable energy resources can result in the autonomous nodes in distributed sensor networks.

In reference [15] a comparative study of the commonly existing renewable energy resources has been made. It has been shown that the generated electrical power density from the solar energy and the mechanical vibrations is quite reasonable for long lifetimes. In the sunny day, the predicted generated power density from solar energy is *15,000 $\mu W/cm^3$*. It reduces to *150 $\mu W/cm^3$* in the cloudy day. Inside the buildings and closed compartments the power density reduces to *6 $\mu W/cm^3$*. Hence for the applications which are permanently installed in dark areas having no direct access to light energy, the solar energy is not a feasible solution. Power is generally provided by means of wires. In order to provide autonomous nodes in a sensor network and to power smart-dusts [32], ambient vibration is a power source that is largely considered, as there exist broadband vibration spectrum in applications like automotives [24], airplanes [33], buildings [34] etc…

Hence the mechanical vibrations are being chosen as the renewable energy source in the contest of this research work. Various studies have been made to measure the vibration frequencies, their bandwidths and amplitudes of different applications. According to [35], the frequencies of domestic applications like Heating Ventilating and Air Conditioning (HVAC), blender, washing machine, CD writer, etc… lies up to 120 Hz with acceleration ranging from 0.2 m/s² to 9,8 m/s^2 (1g). For car engines the vibration spectrum is around 200 Hz with an acceleration of 12 m/s², whereas for car compartment it is around 13-33 Hz with an acceleration of around 3 to 6 m/s² [24, 35]. Another automotive application is Tire Pressure Monitoring System (TPMS) with wide frequency range from 5 Hz to 1 kHz and acceleration ranging from 4000g to 5000g [36]. Reference [37] reports the peak vibration frequency of 329 Hz with an acceleration of 0.2 m/s² in a machine shop. Similarly a broadband vibration spectrum exists in aircrafts. Reference [33] reports the spectrum of noise in the cabin, related to the engine vibrations. The observed spectrum has vibration peaks at 100 Hz and 200 Hz.

Various collaborative projects like PicoRadio [38] at UC Berkeley, μAMPS [39] at MIT, VIBES [40] in collaboration amongst various European teams and ORESTEIA [41] at Imperial College, had been conducted regarding different energy scavenging techniques for distributed sensor network.

1.2 State of art of Vibration based energy harvesting

The electrical power generation from mechanical vibrations is achieved in two stages. At first, a proof mass is coupled with the environmental vibrations through an elastic link (spring): the mass and the spring constitute a mechanical resonator present in almost all vibration energy harvesters. Thanks to this coupling, the mass oscillates in the reference system and accumulates a mechanical energy. The second stage is the conversion of this energy into electric energy. For this, an electromechanical transducer should apply on the mass a damping force, i.e., should perform a negative work on the mechanical system. The damping force has two components; one is related to the inertia of the mass which corresponds to the energy losses and the second is related to the force induced by the electromechanical transduction. In case of electromagnetic, electrostatic and piezoelectric transducers, the electromechanical damping force is created by magnetic field, electric field and straining piezoelectric material respectively [16, 42]. A conditioning circuit is needed to manage the electrical energy flow towards the electric load. The architecture of the electronics depends upon the adopted transduction mechanism. The architecture of a vibration powered energy harvester is shown in the Fig. 1.6.

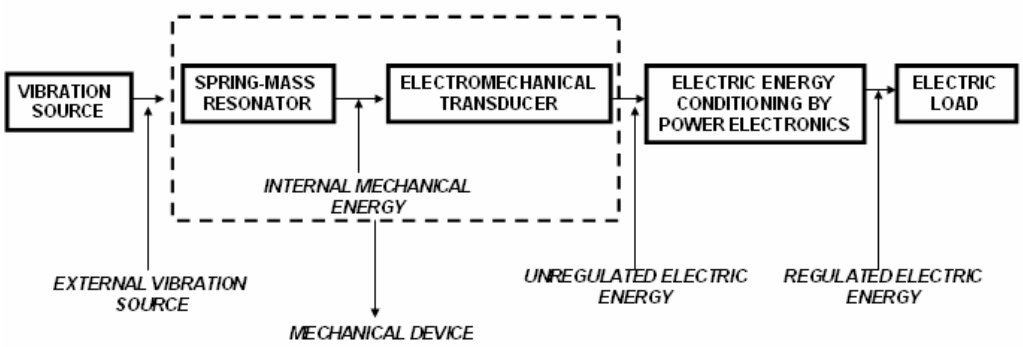

Fig. 1.6 General architecture of a mechanical vibrations powered energy harvester

1.2.1 Resonant and non-resonant generators

Energy harvesters can be resonant or non resonant. The resonant generators are intended for the applications when the source amplitude is small compared to the possible proof mass displacement and works only for a specific narrow band of frequencies. In literature the resonant generators have been classified as Velocity Damped Resonant Generator (VDRG) and Coulomb Damped Resonant Generator (CDRG) [42]. The first one deals when the electromechanical force is proportional to velocity, whereas the later is applicable when electromechanical force is a constant force. The maximal power generation at the resonance frequency for both generators is same. Non resonant generators are used in applications where the external vibration power is spread in a large band (at low-frequency) and the vibration amplitude is large as compared to the allowable proof mass displacement, e.g. harvesting the energy from the human body movement for which the vibration spectrum is from 1 Hz to a few tens of Hz [43]. Non resonant generators are called as Coulomb Force Parametric Generator (CFPG) [42].

1.2.2 Maximal power generation for resonant transducer

An ideal resonant generator can be modeled by second order spring, mass and damper systems as shown in the Fig. 1.7. By ideal we mean that the electrical damping is strictly

proportional to the proof mass velocity, which is true for only specific cases. Along with the mechanical representation the electrical equivalent of the system is also represented. The available power can be estimated using the dynamic equation for the mass, spring and damper system (mechanical domain), which can be given as:

$$m\frac{d^2x}{dt^2}+(b_m+b_e)\frac{dx}{dt}+k_m x=-m\frac{d^2y}{dt^2}, \tag{1.1}$$

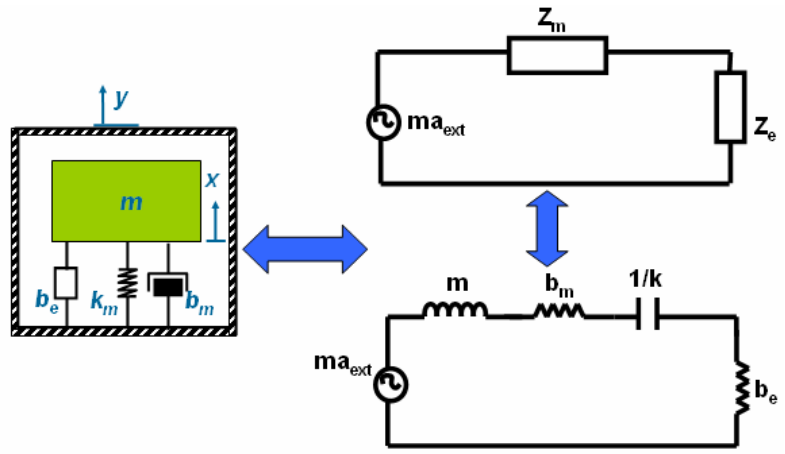

Fig. 1.7 Mass spring damper and an equivalent RLC representation of an ideal energy harvester

where m is the mass of the system, b_m is mechanical damping due to the air damping, b_e is electrical damping which represents the conversion mechanism between the kinetic and electrical energy, k_m is the spring stiffness, x is the displacement of the proof mass and y is external excitation. Energy losses within the system comprise the losses in the damper b_m. Assuming a sinusoidal external excitation (let $y=Y\,sin(\omega t)$, the equation (1.1) can be solved to get the solution for the mass displacement x [44- 46]:

$$x=\frac{m\omega^2 Y}{\sqrt{\left(k_m-m\omega^2\right)^2+\left((b_m+b_e)\omega\right)^2}}, \tag{1.2a}$$

The output power is the average power converted by the damper b_e i.e. [45]

$$P_e=\frac{b_e\omega^2x^2}{2}, \tag{1.2b}$$

Using equation (1.2a) in (1.2b) gives us the following relation:

$$P_e = \frac{b_e m^2 \omega^6 y^2}{2\left(\left(k_m - m\omega^2\right)^2 + \left((b_m + b_e)\omega\right)^2\right)}, \tag{1.3}$$

Power losses can be given as across b_m:

$$P_m = \frac{b_m m^2 \omega^6 y^2}{2\left(\left(k_m - m\omega^2\right)^2 + \left((b_m + b_e)\omega\right)^2\right)}, \tag{1.4}$$

Fig. 1.8 (a) and (b) shows the normalized power generated using the above power generation model for different Q-factors (keeping everything else same for both curves). The Q-factor of the resonator is defined as the ratio between the mechanical resonance frequency and bandwidth of the resonator. Mathematically it can also be described as:

$$Q = \frac{\sqrt{mk_m}}{b}, \tag{1.5}$$

Here b is the sum of electrical and mechanical damping. In Fig. 1.8 (b) the value of the Q-factor is 1/3rd of the value taken in Fig. 1.8 (a). The power of Fig. 1.8 (b) is also normalized with the maximum power generated for Fig. 1.8 (a). The frequency is normalized with the resonance frequency. Along the y-axis, the ratio of the electrical to mechanical damping is taken. It can be seen that increasing the mechanical damping (i.e. decrease in the Q-factor cf. Fig. 1.8 (b)) makes the system much sensitive to higher bandwidth but resulting in decrease in the power generation.

The system generates maximum power when:

1) The vibration source frequency matches with the resonance frequency of the energy harvester that's why there are termed as resonant generators.
2) The electrical damping of the system is equal to the mechanical damping.

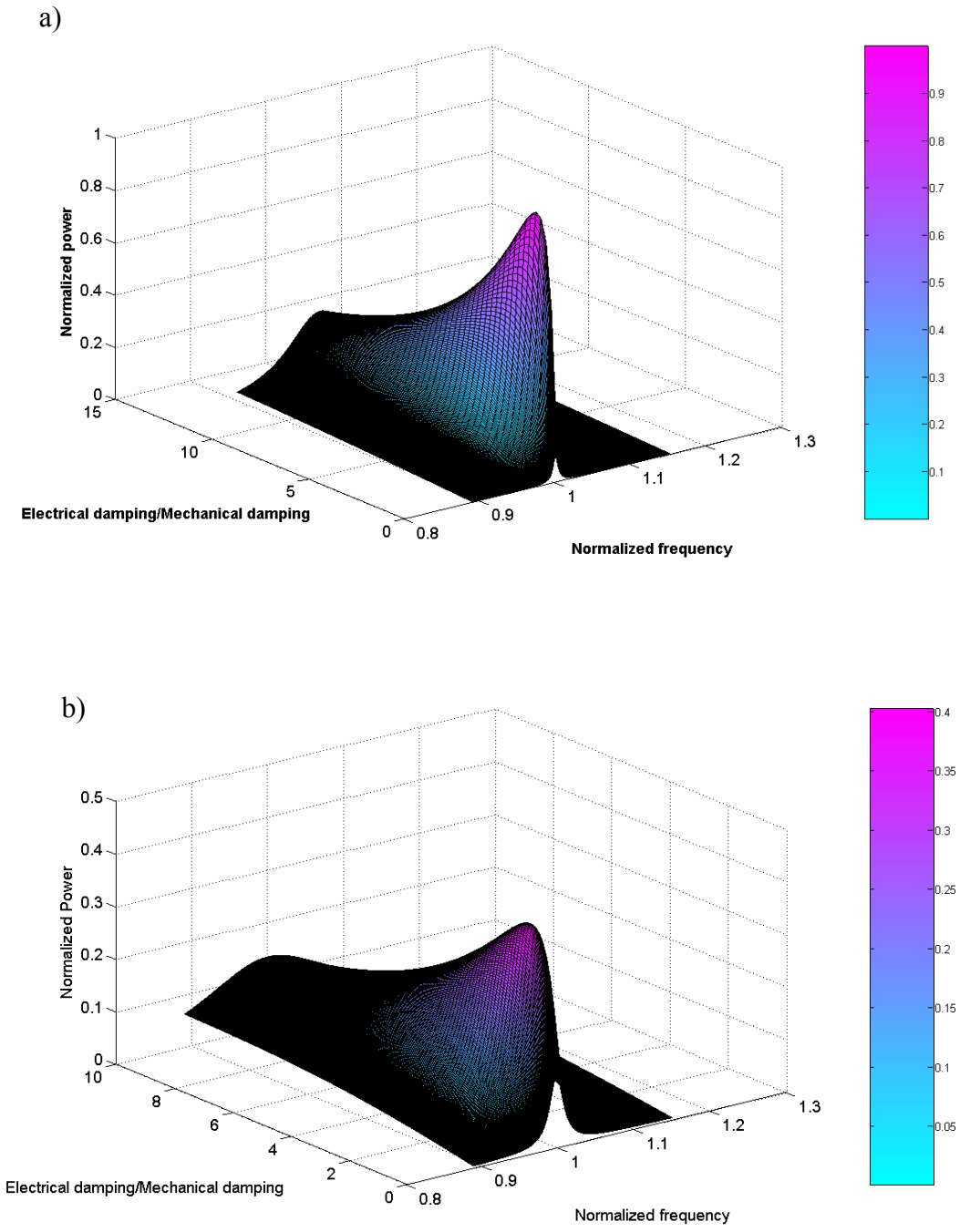

Fig. 1.8 a) Normalized power for system shown in Fig. 1.7 and using equation (1.3) b) Normalized power for system shown in Fig. 1.7 and using equation (1.3) with 1/3rd the Q-factor, normalization is done with the maximum power generated in Fig. 1.8 (a)

1.2.3 Power generation for non ideal resonant generator with displacement constraints

In this section we will derive an expression for the maximal power generation with the limited displacement, as in the real applications the proof mass displacement cannot be infinite. For that purpose we use an electrical impedance network analogy. Consider the electrical equivalent of the mechanical system in Fig. 1.7. Z_m represents the mechanical impedance of the resonator and is defined by m, b_m and k_m. Z_e represents the mechanical impedance of the transducer. ma_{ext} is the external mechanical vibration force which can be represented as the voltage source in the impedance network. With this method, we can study transducers having a complex Z_e i.e. non ideal transducer.

From the electromechanical analogy, the power absorbed by a dipole is the real part of the complex power, defined as the half square of module of the current times the impedance of the load. In the mechanical domain, the current is equivalent to the velocity and can be found by dividing the voltage source (external force) by total impedance of network. The power absorbed can be given as:

$$P = \frac{1}{2}\left|\frac{ma_{ext}}{Z_m + Z_e}\right|^2 \mathrm{Re}(Z_e), \tag{1.6}$$

The displacement can be given as the net charge of the electrical network i.e.

$$x = \left|\frac{ma_{ext}}{Z_m + Z_e}\right|\frac{1}{\omega} \le x_l, \tag{1.7}$$

Here ω is the vibration frequency and x_l is the displacement constraint.

Using the equality in equation (1.7) we can derive the following relation:

$$Z_m + Z_e = \frac{ma_{ext}}{\omega x_l}, \tag{1.8}$$

Now the right hand side can be expanded as:

$$(\mathrm{Re}(Z_m + Z_e))^2 + (\mathrm{Im}(Z_m + Z_e))^2 = \left(\frac{ma_{ext}}{\omega x_l}\right)^2$$

$$\mathrm{Re}(Z_e) = \sqrt{\left(\frac{ma_{ext}}{\omega x_l}\right)^2 - (\mathrm{Im}(Z_m + Z_e))^2} - \mathrm{Re}(Z_m)$$

Z_e should be chosen to have $\mathrm{Im}(Z_m) = -\mathrm{Im}(Z_e)$, the above equation becomes:

$$\mathrm{Re}(Z_e) = \left(\frac{ma_{ext}}{\omega x_l}\right) - \mathrm{Re}(Z_m), \tag{1.9}$$

The real part of mechanical impedance Z_m is composed of b_m i.e.:

$$\mathrm{Re}(Z_m) = b_m$$

Using these representations, equations (1.8) and (1.9) in (1.6), the maximum power within the displacement constraint can be given as [47]:

$$P_{\max} = \frac{1}{2}\left|x_l\omega\right|^2\left(\frac{ma_{ext}}{x_l\omega} - b_m\right), \tag{1.10}$$

Let $b_m = 0$ and $a_{ext} = y_{ext}\omega^2$, a_{ext} is the external acceleration then equation (1.10) becomes:

$$P_{\max} = \frac{1}{2}x_l y_{ext}\omega^3 m = \frac{1}{2}x_l a_{ext}\omega m, \tag{1.11}$$

Equation (1.11) exactly matches with the expression which is being developed for the limited displacement for the VDRG case in reference [42], with an assumption that b_m is zero.

1.2.4 Existing energy harvesting techniques from mechanical vibrations

The three main existing techniques to harvest energy from environmental ambient vibrations are based on electrostatic [24, 48], piezoelectric [48-50] and electromagnetic [14, 23] electromechanical transducers (schematics of all are shown in Fig. 1.9). Piezoelectric energy harvesters give good power density and there is no need of extra energy source for starting [35]. However, they are not the best candidates for miniaturization in a sense that

most efficient existing piezoelectric materials are not compatible with CMOS clean rooms. Electromagnetic energy harvesters work on the principle of Faraday's law of electromagnetic induction. They have good power density but there is again the problem of compatibility with CMOS process and especially, they are not well suitable for miniaturization since they require high-volume inductors and often thin film ferromagnetic materials as well as magnets. Electrostatic energy harvesters have the advantage of CMOS process compatibility and are considered to be the more suitable for miniaturization and, in spite of their known drawbacks (relatively low energy yield and the need for a start-up energy source), they are seen as the most promising candidates for the future full-integrated and miniaturized autonomous embedded systems [51]. Apart from these existing techniques, more recent approach is to use Villari effect in magnetostrictive material. Magnetostrictive materials can convert magnetic energy into kinetic energy, or vice versa. The problem with this technique is again the miniaturization and CMOS compatibility issues of the thin film materials [52].

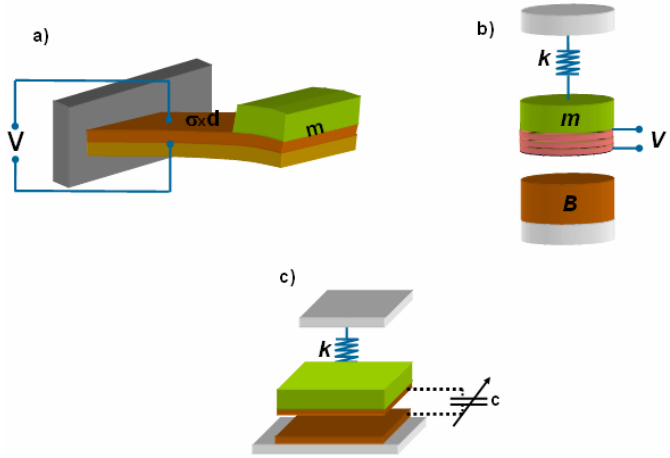

Fig. 1.9 Three ways to harvest electric energy powered from the vibrations a) Piezoelectric, b) Electromagnetic (inductive) and c) Electrostatic (capacitive)

1.3 State of art of electrostatic harvesters

The electrostatic resonant energy harvester includes a mechanical resonator associated with a capacitive transducer as shown in Fig. 1.9 (c). A capacitive transducer is a device with two electrodes. The first one is attached to the proof mass which is coupled with the vibrating reference frame, the second electrode is being fixed to the frame and submitted to the external vibrations. Hence the transducer capacity varies because of the relative motion of the two electrodes set. A variable capacitor can generate energy if it is charged when its capacity is high, and discharged when it is low, following the formula for the capacitor energy $E= Q^2/(2C)$. This cycle increase an electrical energy across the capacitor due to increase in voltage, and the energy elevation for a conditioning electronic allowing the QV cycle in Fig. 1.10 is given by [51]:

$$\Delta E = E_O\left(\frac{C_{\max}}{C_{\min}} - 1\right), \tag{1.12}$$

where E_0 is the starting energy used to charge the C_{max} capacitance to a charge Q. Hence, the converted electrical energy is (C_{max}/C_{min}-1) times higher than this initially provided electrical energy. At point A (Fig. 1.10) the capacitance is at the position of C_{max}, the capacitor is charged until the voltage becomes V_0 as shown by point B. At this moment by means of the mechanical vibrations, the capacitance reduces from C_{max} to C_{min} and voltage increases in the inverse fashion as shown by point D, as a result of which a net energy is generated, which is shown by the equation (1.12). Finally the capacitance discharges into some reservoir and the system is again at point A. This is the process where net charge of the system is kept constant. The area of the cycle is numerically equal to the generated energy, which is same as equation (1.12) [51]. This is generated electrical energy in an ideal case where the charge is constant associated electronics is lossless and the starting point A is identical at all cycles. Apart from the constant charge cycle, there is also voltage constant cycle, where there is a charge

variation as a result of capacitance change, leading to better conversion efficiency. The charge constant process is preferred over the voltage constant process as the later requires two separate voltage sources to maintain the constant voltage as compared to the former [35, 51].

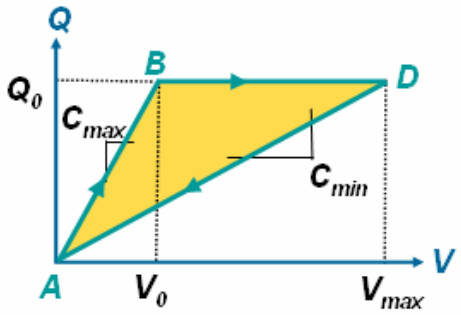

Fig. 1.10 QV diagram of constant charge process [51]

From the mechanical point of view, during this cycle, the transducer generates on the mass an average electrical damping force, tending to attenuate the vibrations. However, such an energy generation requires a starting energy E_0 which can be provided by many ways. The most popular solution is the use of an electret, located below the proof mass, which has been reported in the recent times [53, 54]. Electret is the material which can maintain constant electrical field. Another idea which has been presented is to make the system hybrid i.e. to use electrostatic mechanism to harvest energy and to use piezoelectric phenomena to provide initial charge [55]. The idea of using thermoelectric effect to generate an initial voltage has also been reported [56]. Another proposed solution is to utilize materials with different work functions for the two electrodes. As soon as the two electrodes are electrically contacted, the Fermi levels are equilibrated and acquire an electronic current [57]. Apart from these techniques, some of the resonant generators use an initially charged buffer capacitor to provide E_o and uses externally controlled switches to charge and discharge the capacitor [24, 45, 58, 59]. In order to calculate the harvested power from equation (1.12), we multiply the mechanical frequency of the resonant electrostatic energy harvester with the harvested energy.

1.3.1 Major geometrical topologies used for electrostatic energy harvesters

It is said that the electrostatic based energy harvester is based upon the variable capacitor. Equation (1.12) can be written as:

$$\Delta E = \frac{1}{2} V_O{}^2 \left(C_{\max} - C_{\min}\right)\left(\frac{C_{\max}}{C_{\min}}\right), \tag{1.13}$$

Here V_0 is the voltage which corresponds to the energy E_0 stored in C_{max}. The equation shows that maximizing the generated energy requires the variable capacitor to have maximum value as well as maximum span -to maximize the capacitance difference $\left(C_{\max} - C_{\min}\right)$ along with its ability to support high voltage V_0 without reaching the electrostatic instability (pull-in) [60]. The typical four geometries of resonator-transducers for electrostatic energy harvesters are: In-Plane Overlap Comb (IPOC) [48, 51], In-Plane Gap-closing Comb (IPGC) [24, 48], Out-of-Plane Gap-closing Plate (OPGP) [48, 61] and In-Plane Overlap Plates (IPOP) [54, 62]. IPOC configuration is the one in which the capacitance variation is due to change in overlap area of comb-drive electrodes. IPGC type has the same mechanical comb drive architecture as in the previous case, but the capacitance variation is due to change in transversal gap between the comb-drive electrodes. OPGP architecture is also gap closing type, but in contrast to previous type it has the conventional parallel plate architecture and exhibits an out of plane motion of proof mass. The IPOP mechanism also has the parallel plate capacitor structure, but the capacitance variation is related with the change in overlap area due to the in-plane movement of proof mass. All these topologies are shown in Fig. 1.11.

Table 1.1 shows the formulae for the capacitance variation and the electrostatic force (F_e) for each topology, for the constant charge case. F_e is calculated by the relation:

$$F_e = -\frac{Q^2}{2}\frac{d}{dx}\left(\frac{1}{C(x)}\right), \tag{1.14}$$

Where Q is electrical charge and $C(x)$ is the capacitance variation.

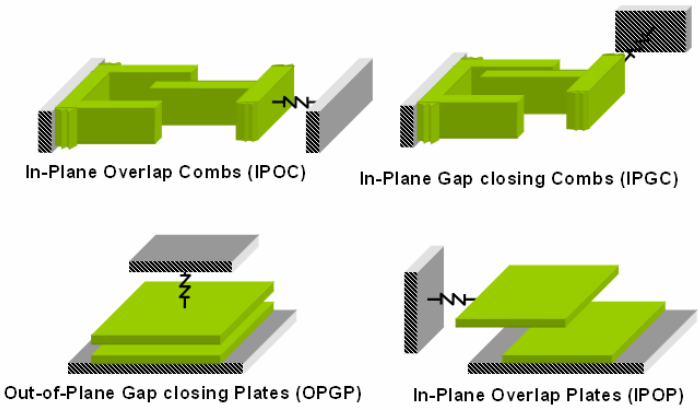

Fig.1.11 Major topologies used for electrostatic energy harvesters

Structure	***Capacitance C(x)***	***Electrostatic Force F_e***
IPOC	$\frac{\varepsilon_O N w(l+x)}{h}$	$\frac{Q^2 h}{2\varepsilon_O N w(l+x)^2}$
IPGC	$\frac{2\varepsilon_O N w l}{h^2 - x^2}$	$\frac{Q^2 x}{2\varepsilon_O N w l}$
OPGP	$\frac{\varepsilon_O w l}{h+x}$	$\frac{Q^2}{2\varepsilon_O w l}$
IPOP	$\frac{\varepsilon_O N l(w-x)}{h}$	$\frac{Q^2 h}{2\varepsilon_O N l(w-x)^2}$

Table.1.1 Capacitance variation and electrostatic force for constant charge system

In the above table *l, w, N, h,* ε_o, and *x* are length, width, number of electrodes, gap between two electrodes, permittivity of free space and displacement of the movable electrode. It can be seen that the electrostatic force for OPGP is constant whereas for IPGC the force varies linearly with the displacement. For IPOC and IPOP the force varies as the reciprocal of the square of the displacement. For the case of the present study, IPOP has been chosen for the reasons to be explained in chapter 2.

The expression of F_e can be helpful in order to estimate the generated power. As it was already explained above that for an electromechanical transducer, there should be an

application of a damping force on the mass i.e., should perform a negative work on the mechanical system. In the case of electrostatic based energy harvester that damping force is the electrostatic force. The power from F_e can be given as:

$$P = nf_m \Delta E \,, \tag{1.15}$$

Where

$$\Delta E = \int_{x_n}^{x_m} F_e(x)dx \,, \tag{1.16}$$

and n represents the number of electrical cycles in one mechanical cycle, f_m is the vibration frequency, E is the energy generated and x_m and x_n is the maximum and the minimum displacement respectively which correspond to the one variation cycle of the capacitance from C_{max} to C_{min}.

Now we will calculate the net energy generated for the IPOP configuration, hence using the expression of F_e for IPOP configuration in equation (1.16).

$$\Delta E = \int_{x_n}^{x_m} \frac{Q^2 h}{2\varepsilon_O Nl(w-x)^2} dx \,, \tag{1.17}$$

For $x = x_n$, the capacitance is maximum i.e. C_{max}, the equation can be given as:

$$C_{\max} = \frac{\varepsilon_O Nl(w-x_n)}{h} \,, \tag{1.18}$$

For $x = x_m$, the capacitance is minimum i.e. C_{min}, the equation can be given as:

$$C_{\min} = \frac{\varepsilon_O Nl(w-x_m)}{h} \,, \tag{1.19}$$

For Q (we are considering the constant charge case) we have:

$$Q = C_{\max} V_O \,, \tag{1.20}$$

here V_o is the initial voltage. Solving the integral in equation (1.17)

$$\Delta E = \frac{Q^2 h}{2\varepsilon_O Nl}\left(\frac{1}{w-x_m} - \frac{1}{w-x_n}\right), \tag{1.21}$$

Using equations (1.18), (1.19) and (1.21), gives us the following result:

$$\Delta E = \frac{1}{2} V_O^{\,2} \left(C_{\max} - C_{\min}\right)\left(\frac{C_{\max}}{C_{\min}}\right)$$

The obtained result is the same as equation (1.13). For the other topologies we can get the same expression of ΔE using the expression of F_e. Using equation (1.13) in (1.15) gives net power generated by the energy harvester using electrostatic transduction.

The net power generated given by equation (1.15) is different from (1.3). Equation (1.3) is the net power generated by the mass, spring, damper system. This equation is not intended for any specific system. The power generation depends on the factor b_e, which depends on the way of transduction. On the other hand, equation (1.15) is the power generated by the system based on the electrostatic transduction. It is based on the hypothesis of an ideal system returning all the electrical charges when the capacitance returns from the minimum to the maximum capacitance position.

1.4 Review on constant charge electrostatic based resonant energy harvesters

Table. 1.2 shows reported resonant constant charge electrostatic micro-generators. The idea of using an electret with IPOP configuration is quite popular, as it solves the problem of initial charge storage and it also simplifies associated electronics [53, 54, 63, 64, 65, 66]. But IPOP devices have the problem of pull-in [60]. Apart from electret-based IPOP generators, according to our knowledge, only three resonant functional generators have been reported, based upon the principle of constant charge using an external pre-charge [24, 58, 59]. Three of them are not micro-machined. Also there are huge in area, as micro-generator reported in [24] the surface area is 18 cm² and it is made of Tungsten. The one reported in [58] is made of Steel and Aluminum with 6.6 cm² surface area. Next generator presented in [59] is made up of

metal [16]. We can hardly compare the performance of different micro generators by a single parameter, as each micro generator is intended for a specific application having their own frequency and vibration amplitude. Nevertheless, an attempt of comparison will be presented in chapter 4 through different figures of merit.

Year	Initial voltage	Type	P(μW)	Freq (Hz)	Mass (gm)	Surface Area or Volume	Ext. Disp. (m/s)	Material	Comments	Cmax /cm²	ΔC/ cm²
2006 Yen et al., [58]	*6 V*	*OPGP*	*1.8 μW*	*1.6 kHz*	*-*	*6.6 cm²*	*-*	*Steel + Aluminum*	*Charge pump with flyback with 20 MΩ load*	*-*	*52.73 pF/cm²*
2005 Despesse et al., [24]	*150 V*	*IPGC*	*1052 μW*	*50 Hz*	*104 gm*	*18 cm² x 1 cm*	*116 μm*	*Tungsten*	*Transformer with switches*	*200 pF/cm²*	*150 pF/cm²*
2003 Miyazaki et al., [59]	*-*	*OPGP*	*120 nW*	*45 Hz*	*-*	*-*	*1 μm*	*Steel*	*10 MΩ load*	*350 pF*	*320 pF*

Table. 1. 2 Examples of non-electret, constant charge electrostatic based, resonant energy harvesters

1.5 Intended work

Keeping in view the details, information and the list provided above (cf. table 1.2), this section will define the intended work of this thesis.

1) Among the renewable energy resources, solar energy is considered superior in performance to others. However, the power generation in the dark compartments is quite low [15]. Hence in the applications like automotives, aeronautical and civil engineering, where the applications are not directly in the range of solar light, the vibration based energy harvesting can be sometimes more useful as compared to the solar energy.

2) Amongst four existing techniques of vibration powered energy harvesting, electrostatic-based transduction has the best compatibility with CMOS process.

3) Looking at the list of the functioning resonant non-electret generators, we see that none of them are batch fabricated. So the intended work should be a design and fabrication of the

energy harvester which is "CMOS compatible" and fabricated from silicon on glass technology.

4) All of them are quite huge in size. We impose a constraint of 1 cm² in our case. The harvester should be enclosed in this dimension.

5) The targeted ambient vibration frequency should be kept as low as possible to make system apt for low frequency vibration sources.

Up to our knowledge no silicon based vibration powered resonant micro-machined electrostatic transducer without using an electret layer is functioning at the low frequency, in a range of few hundred Hz, with such a small surface area.

1.6 Conclusion

This chapter is started with some of the market trends in MEMS. Then we discussed renewable energy resources from the large scale to the nano scale. Due to the low power generation in the dark compartments by solar energy, vibration-based renewable resources are selected. Among various techniques of vibration-based energy harvesting, the electrostatic based transduction is selected due to its CMOS compatible nature. We also developed the optimum power generation model for the vibration powered energy harvesting. The formulae for the power generation for non-ideal resonant generator with displacement constraints are derived. Two cases are presented without and with taking into account the mechanical damping. With the applied method, we can also study the transducers having a complex electrical damping i.e. non ideal transducer. In the light of this discussion we laid down the parameters of our intended work, which is vibration powered, electrostatic transduction based, batch fabricated in silicon on a glass technology and within 1 cm² surface area.

Reference:

[1] "60 years of the transistor: 1947 - 2007", http://www.intel.com/technology/timeline.pdf, site visited 23/07/2009

[2] J. H. Smith, *et al.*, "Embedded Micromechanical Devices for the Monolithic Integration of MEMS with CMOS", *Proc. IEDM*, 1995, *pp. 609-612*

[3] Jean-Christophe Eloy, "MIS-07 Status of the MEMS industry", Yole development report, latest update June 2007

[4] Global status report by Renewable energy policy network for the 21st century, "Renewables 2007", http://www.ren21.net/pdf/RE2007_Global_Status_Report.pdf, site visited 01/04/2009

[5] "The top 100, the world's largest power plants", http://www.industcards.com/top-100-pt-1.htm, site visted 23/07/2009

[6] "Serpa Solar Power Plant, Portugal", http://www.power-technology.com/projects/Serpa/, site visited 01/04/2009

[7] "Wind", *Global water and power – solutions for a renewable future*, http://globalwaterandpower.com/wind/, site visited 23/07/2009

[8] Wikipedia, "Solar cell", *Free online encyclopedia*, http://en.wikipedia.org/wiki/Solar_cell, site visited 01/04/2009

[9] http://www.seikowatches.com/technology/kinetic/index.html, site visited 01/04 2009

[10] Wikipedia, "Automatic watch" , *Free online encyclopedia*, http://en.wikipedia.org/wiki/Automatic_watch, site visited 01/04/2009

[11] Ivan Stojmenovic, "Handbook of sensor networks", Published by John Wiley and Sons, 2005

[12] Wikipedia "Thermoelectric effect", *Free online encyclopedia*, http://en.wikipedia.org/wiki/Thermoelectric_effect, site visited 01/04/2009

[13] Z. Wang *et al.,* "Characterization of poly-$si_{70\%}ge_{30\%}$ for surface Micromachined thermopiles" *Proc. of MEMS'08*, pp. 23-26, 2008

[14] R. Amirtharajah *et al.,* "Self-Powered Signal Processing Using Vibration-Based Power Generation", *Proc. of IEEE Journal of Solid-State Circuits,* vol. 33, no. 5, May 1998, *pp. 687-695*

[15] Shadrach Joseph Roundy, "Energy Scavenging for Wireless Sensor Nodes with a Focus on Vibration to Electricity Conversion", PhD thesis, 2003, University of California Berkeley

[16] S. P. Beeby *et al.,* "Energy Harvesting Vibration Sources for Microsystems Applications", *Review Article Proc. of Measurement Science and Technology (IOP),* pp.R175-R195, 2006

[17] Paradiso *et al.,* "Energy scavenging for mobile and wireless electronics", *Pervasive computing,* pp. 18-27, 2005

[18] W. Lee, *et al.*, "A 1V DSP for wireless communications," in *ISSCC 1997 Dig. of Tech. Papers,* Feb. 1997, *pp. 92–93*

[19] A. Chandrakasan, *et al.*, "A low power chipset for multimedia applications," in *ISSCC 1994 Dig. of Tech. Papers,* Feb. 1994, *pp. 82–83*

[20] E. A. Vittoz, "Low-power design: Ways to approach the limits," in *ISSCC 1994 Dig. Tech. Papers,* Feb. 1994, *pp. 14–18*

[21] P. Basset *et al.*, "Chip-size antennas for implantable sensors and smart dusts", *Proc. of Transducers'05*, Seoul, Korea, 2005

[22] Lecture notes "An introduction to Microsystems MEMS", Prof. Jean-Pierre RASKIN, Université catholique de Louvain, site: http://www.emic.ucl.ac.be/Courses/Elec2560/MEMS_introduction.pdf

[23] P. Glynne-Jones, "An electromagnetic, vibration-powered generator for intelligent sensor systems", Proc. of *Sensors and Actuators A 110 (2004)*, pp. 344–349

[24] G. Despesse *et al.,* "Fabrication and Characterization of High Damping Electrostatic Micro Devices for Vibration Energy Scavenging", *Proc. of DTIP'05*, pp. 386-390, 2005

[25] N. S. Shenck, "Energy scavenging with shoe-mounted piezoelectrics", *Proc. of IEEE Micro, May-June 2002*, pp. 30 – 42

[26] Z. L. Wang, "Energy Harvesting Using Piezoelectric Nanowires–A Correspondence on ''Energy Harvesting Using Nanowires'' by Alexe et al.", *Proc. of Advanced materials 2008, 20,* pp. 1-5

[27] "Nanoscience and the Mobile Device"*http://research.nokia.com/files/insight/NTI_Nanoscience_-_Dec_2008.pdf*, site visited 01/04/2009

[28] E. S. Aydil, "Photovoltaic Devices Based on Nanoparticles and Nanowires", *Proc. of NSF Nanoscale Science and Engineering Grantees Conference*, 2006

[29] S.Y. Chou, P.R. Krauss and P.J. Renstrom, *Appl. Phys.Lett.* 67, 3114, 1995

[30] Yong Qin, *et al.,* "Microfibre–nanowire hybrid structure for energy scavenging", Nature 451, *pp.* 809-813 (14 February 2008)

[31] Rusen Yang *et al.,* "Power generation with laterally packaged piezoelectric fine wires" Nature Nanotechnology Published online: 9 November 2008 | doi:10.1038/nnano.2008.314

[32] Warneke *et al.,* "Exploring the Limits of System Integration with Smart Dust", *Proc. of IMEC'02*, New Orleans, USA, 2002

[33] Jesse Depriest, "Aircraft Engine Attachment and Vibration Control", *Lord Library of Technical Articles*, LL-6505

[34] http://www.mellesgriot.com/pdf/CatalogX/X_31_3-7.pdf, "Sources of Vibration", *Catalogue on Fundamentals of vibration isolation*, pp. 31.3-31.7

[35] S. Roundy *et al.*, "A study of low level vibrations as a power source for wireless sensor nodes", *Proc. of Computer Communications 26 (2003)*, pp. 1131-1144

[36] M. Löhndorf *et al.,* "Evaluation of Energy Harvesting Concepts for Tire Pressure Monitoring Systems", *Proc. of PowerMEMS2007*, Freiburg, Germany, *pp. 331-334,* 2007

[37] H. Okamoto *et al.,* "Efficient Energy Harvesting from Wideband Vibrations by Active Motion Control", *Proc. of PowerMEMS2007*, Freiburg, Germany, *pp. 101-104,* 2007

[38] http://bwrc.eecs.berkeley.edu/Research/Pico_Radio/, site visited 01/04/2009

[39] http://mtlweb.mit.edu/researchgroups/icsystems/uamps/, site visited 01/04/2009

[40] http://www.vibes.ecs.soton.ac.uk/, site visited 01/04/2009

[41] http://www.disappearing-computer.net/projects/ORESTEIA.html, site visited 01/04/2009

[42] Paul D. Mitcheson *et al.,* "Architectures for Vibration-Driven Micropower Generators", *Proc. of Journal of Microelectromechanical Systems,* vol. 13, no. 3, June 2004, pp. 429-440

[43] Von Buren, "Optimization of inertial micropower Generators for human walking motion", *Proc. of IEEE Sensors Journal*, vol. 6, issue 1, Feb 2006, pp. 28-38

[44] Ghislain Despesse, "Etude des phénomènes physiques utilisables pour alimenter en énergie électrique de microsystèmes communicants", PhD thesis, June 2005, Institut National Polytechnique de Grenoble (INPG)

[45] José Oscar Mur Miranda, "Electrostatic vibration to electric energy conversion", PhD thesis, February 2004, Massachusetts Institute of Technology (MIT)

[46] C. B. Williams and R. B. Yates, "Analysis of a micro-electric generator for Microsystems*", Sens. and Act. A: Phys.,* Vol. 52, No 1, pp. 8-11, 1996

[47] A. Mahmood Paracha *et al.,* "MEMS DC/DC converter for 1D and 2D vibration-to-electricity power conversion", Transducers 2009, pp. 2098-2101, 2009

[48] S. Roundy *et al.*, "Micro-electrostatic vibration-to-electricity converters", *Proc. of IMEC'02*, New Orleans, USA, 2002

[49] M. Marzencki *et al.*, "Design and fabrication of piezoelectric micro power generators for autonomous microsystems", *Proc. of DTIP'05*, pp. 299-302, 2005

[50] D. Shen *et al.,* "The design, fabrication and evaluation of a MEMS PZT cantilever with an integrated Si proof mass for vibration energy harvesting", *Proc. of Journal of Micromechanics and Microengineering,* April 2008*, pp. 1-7*

[51] S. Meninger *et al.*, "Vibration-to-electric energy conversion", *IEEE Trans. on VLSI*, vol. 9, no. 1, pp. 64-76, 2001

[52] Wang L, Yuan FG, "Energy harvesting by magnetostrictive material (MsM) for powering wireless sensors in SHM", *SPIE Smart Structures and Materials & NDE and Health Monitoring, 14th International Symposium (SSN'07)*, 2007

[53] T. Sterken, *et al.,* "A newpower MEMS component with variable capacitance", *Proc. of Pan Pacific Microelectronic Symposium, Hawaii*, 2003, *pp. 27–34*

[54] Y. Arakawa *et al.*, "Micro seismic power generator using electret polymer film", *Proc. of PowerMEMS 2004*, 2004

[55] M. Khbeis *et al.,* "Design of a Hybrid Ambient Low Frequency, Low Intensity Vibration Energy Scavenger", *Proc. of PowerMEMS2006*, Berkeley, USA, 2006, pp. 287-290

[56] Norio Sato *et al.,* "Novel MEMS Power Generator with Integrated Thermoelectric and Vibrational Devices", *Proc. of Transducers 2005*, Seoul, Korea 2006, pp. 295-298

[57] I. Kuehne et al., "Power MEMS - A capacitive vibration-to-electrical energy converter with built-in voltage", *Sens. Actuators A: Phys. (2007)*

[58] B. C. Yen, H. L. Jeffery, "A variable capacitance vibration-to-electric energy harvester", *IEEE trans. on circuits and systems*, vol. 53, no. 2, Feb. 2006, *pp. 288-295*.

[59] M. Miyazaki *et al.,* "Electric-energy generation using variable-capacitive resonator for power-free LSI: efficiency analysis and fundamental experiment" *ISLPED'03* pp 193–198.

[60] T. Sterken *et al.*, "Motion based generators for industrial applications", *Proc. of DTIP'06*, 2006

[61] P. Miao *et al.*, "Micro-machined variable capacitors for power generation", *Proc. of Electrostatic'03,* 2003

[62] A. Mahmood Paracha *et al.*, "A MEMS DC/DC Converter for autonomous vibration-to-electrical energy harvester", *Trans. on Electron Device Letters*, Vol-30, no.5, pp. 481-483, 2009

[63] H. Lo and Y. C. Tai, "Parylene-HT-based electret rotor generator", *Proc. of MEMS'08*, pp. 984-987, 2008

[64] H. Lo *et al.,* "A simple micro electret power generator", *Proc. of MEMS'07*, pp. 859-862, 2007

[65] Sakane *et al.*, "High-performance perfluorinated polymer electret film for micro power generation",*Proc. of PowerMEMS 2007*, pp. 53-56, 2007

[66] Jinwen Zhang *et al.*, "PECVD SiO2/Si3N4 double layers electrets for application in mems power generator", *Proc. of PowerMEMS 2007*, pp. 105-108, 2007

Chapter 2
Design of the energy harvester

A vibration-powered resonant mechanical energy harvester is primarily composed of three different parts; a mechanical resonator, an electromechanical transducer and an associated electronics conditioning circuit. In this chapter we will focus on design, modeling and simulation of a MEMS-based energy harvester which utilizes an electrostatic transduction. This part of the work eventually leads to our choice of an original architecture as well as the dimensions of the MEMS part of our designed energy-harvester. Before going into the details, it is necessary to define the design constraints. Table 1.2 in previous chapter highlights the features of three working resonant energy harvesters, excluding those using an electret. The two major problems with all three reported resonant energy harvesters [1- 3], are that they are huge in size (about 6 to 20 cm^2) with reference to surface area, and the second is that they are made up of non-silicon material (i.e. tungsten [1] and steel [2, 3]). Keeping in view the above mentioned problems and discussion made in section 1.5 related to our intended work, we have considered the following constraints while designing energy harvester:

1) As discussed in chapter 1, the proposed energy harvester will be electret free, silicon-based and batch fabricated.

2) In the light of discussion we have in section 1.5, the surface area of the resonator should be kept as small as possible. We decide that the whole footprint, including the surface area for a proof mass, contact pads to access

the electrodes and mechanical springs which are used to suspend the proof mass, should not exceed from the size of 1 cm^2.

3) The frequency of the resonator should be kept as low as possible (a few 100 Hz), since higher vibration frequencies are less common in the ambient environment [2, 4]. But this achievement depends upon technology constraints imposed by Deep Reactive Ion Etching (DRIE). The aspect ratio of DRIE varies throughout the wafer as our mask contains spacing of different size, from 50 µm (gaps between springs and electrodes) to few millimeters (the contact pads to access electrodes). In order to make the resonant system compatible with low frequency applications, while staying within the realistic limits of DRIE technology at the same time, we have decided to use a thick substrate layer of 400 µm to maximize the mass of the system. With this thickness, the realized beam width is 30 µm with minimal *notching effect* and the achievable mechanical resonance frequency is around 250 Hz. (Analytical calculations will be discussed later in the chapter)

4) As we have already explained in chapter 1, the proof mass of energy harvester based on IPOP topology vibrates horizontally. Hence the vertical resonance frequency of a mechanical resonator should be, at least, 10 times higher than the lateral frequency. This provides stability to the transducer against the out-of-axis vibrations. Indeed, such vibrations might cause a contact of top and bottom electrodes resulting in an electrode stiction, which could possibly collapse the system.

The chapter is divided in four sections. In the first section, an overview of the global system will be discussed. Primarily we will focus on energy harvester along with its associated electronics and the performance of overall system. Then in the second section, in order to select the topology of our energy harvester, different criteria will be laid down. The reasons behind our selection of In-Plane Overlap Plate (IPOP) configuration will be highlighted as well. The third section will be oriented towards the mechanical dimensioning of the resonator. It also includes the study of capacitance variation, based on FEM simulations results, for the proposed designs. The last section will conclude all the discussion.

2.1 Global system overview

This section focuses on the global system i.e. the mechanical transducer and the associated electronics. As explained in chapter 1, the energy harvesting using electrostatic transduction while maintaining a constant charge, consists of three steps: 1) to charge the transducer when the variable capacitance C_{Var} is maximum (C_{MAX}) either by some external voltage source or by some already charged reservoir capacitor C_{Res}, 2) due to the vibration-induced in-plane motion of the mass and the corresponding electrode, to allow the capacitance C_{Var} to attain the minimum capacitance state (C_{MIN}) while maintaining a constant charge which increases the net energy stored across C_{Var} and 3) to discharge C_{Var} in the same reservoir when it attains this minimum value (C_{MIN}). One idea to make associated electronics capable of performing the above mentioned functions is the use of two MOS switches [3] as shown in Fig. 2.1. *L* in Fig. 2.1 represents an inductance, which is an intermediary element for energy storage between the reservoir and the transducer. It is an element responsible for "flyback" which means the discharging of C_{var} towards the reservoir. The operation of this circuit can be summarized as follows:

1) Supposing that C_{res} is initially charged. In the first step NMOS is closed and C_{res} is discharged in L.
2) In the second step PMOS is closed and L is discharged in C_{var}.
3) In the next step the capacitance C_{Var} attains the minimum capacitance state (C_{MIN}) while maintaining a constant charge which increases the net energy stored across the transducer.
4) The transducer discharges in the vice versa manner as compared to the charge step.

Here the switches are controlled by an external controller, which generates the control signal for them. So the external controller should be programmed according to the resonance frequency (vibration frequency) of the transducer. First drawback of the system is difficulty in the precise control of transistor's commutation. Secondly, due to transistors' losses the net power consumption of the system increases.

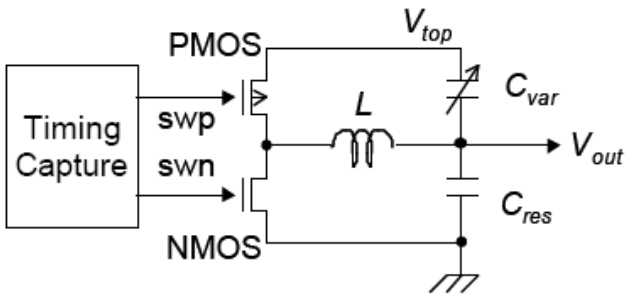

Fig. 2.1 Global system presented by Miyazaki et al. [3]

Another idea to achieve the electrostatic transduction is the detection of maximum and minimum capacitance externally using a comparator circuit (cf. Fig. 2.2a) and achieving the flyback by inductive transformation as schematically shown in Fig. 2.2b [2]. During the charge cycle K_p is closed which gives energy to primary winding L_p, then K_s is closed which transfers the net energy stored in magnetic windings towards C. During the discharge cycle

first K_s is closed followed by K_p which transfers the energy towards energy storage unit E. The disadvantages of this system are: 1) the comparator circuit uses an operational amplifier which contributes towards power losses, 2) the inductive core is not easy to integrate with the CMOS process and 3) there are two switches present in the flyback circuit, which increase the net power consumption of the system.

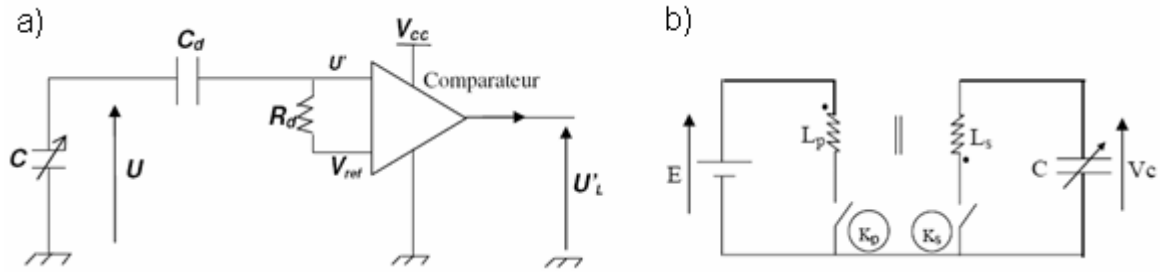

Fig. 2.2a) Capacitance detection block, b) Flyback circuit presented by Despesse et al., [2]

The associated electronics chosen for our application has been presented in [1] and the global system is shown in Fig. 2.3. The operation of the conditioning circuit consists of two phases: energy accumulation (charge pump) and recharge of a reservoir capacitor C_{Res} (flyback), the explanation of these two phases will be presented later in the section. The commutation between the two phases is achieved by the switch *Sw,* which should be OFF while the charge pump is being in operation. The load resistance R_{load} is attached in parallel to C_{Res}. During the recharge process, C_{Res} is charged. On the other hand charge is continuously discharged into R_{load}. The first advantage of this configuration is that we need only one switch to control instead of two and that the switch activates only after a certain number of vibration's period, secondly, in addition it does not require a separate capacitance detection block. These advantages will lead us to the minimization of overall power loss. In the following subsection we will discuss the operation of this system.

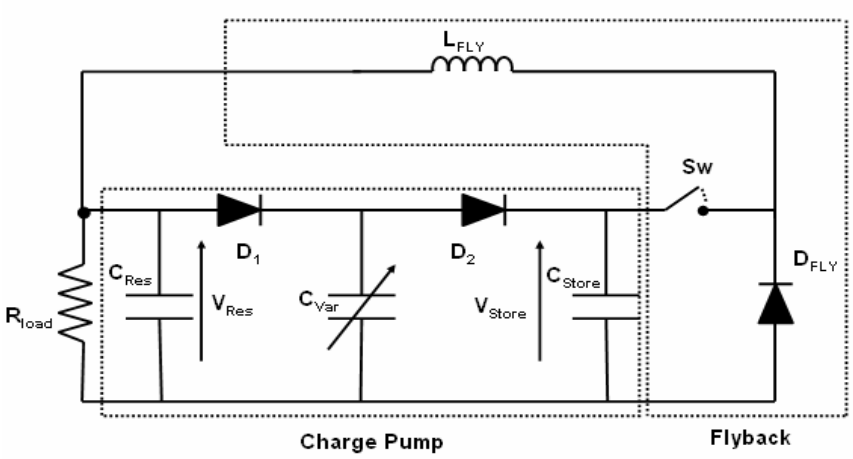

Fig. 2.3 Energy harvesting system [1]

2.1.1 Charge pump operation

The charge pump presented in Fig. 2.3 achieves the electromechanical energy conversion as well as it defines the harvested power. It has three capacitors and two diodes. The capacitors include; the reservoir capacitor (C_{Res}) which provides an initial energy to the system, the variable capacitor C_{Var} (variable between the maximum capacitance C_{MAX} and the minimum capacitance C_{MIN} following the external vibrations phase) and the storage capacitor C_{Store} which is used for temporary storage of an electrical charge during the electromechanical conversion process. The diodes D_1 and D_2 act as "passive" electrical switches.

Let the initial conditions of the charge pump as follows:

$$V_{Res} = V_{store} = V_{var} = V_0 > 0,$$

$$C_{Var} = C_{MAX}$$

D_1 and D_2 are OFF

For the time being we suppose that the voltage drop across D_1 and D_2 is zero in the closed state and infinity in open state (ideal switch). When the resonator vibrates, C_{Var} decreases as a result of which the voltage across the transducer (V_{var}) increases, which switches ON the diode D_2 (while D_1 remains OFF) hence the electric charge flows from C_{Var} to C_{store}. Once reaching its minimum, C_{Var} starts increasing, and conversely V_{var} decreases

which switches OFF the diode D_2. When V_{var} reduces to the level of V_{Res}, D_1 becomes ON and the electric charge of C_{Res} flows toward C_{Var}. Iterations of C_{Var} variations get V_{Store} increase and V_{Res} decrease, keeping the total charge constant. To keep V_{Res} constant during the harvesting operation, C_{Res} should be higher than C_{Store} and C_{Var} . The voltage build up across C_{Store} is given as [1]:

$$\left(V_{store}\right)_n = V_O\left[\left(1-\frac{C_{\max}}{C_{\min}}\right)\left(\frac{C_{Store}}{C_{Store}+C_{\min}}\right)^n + \frac{C_{\max}}{C_{\min}}\right], \tag{2.1}$$

Here n is the number of cycles (pump cycles of charge pump). For n approaching ∞ the voltage across C_{Store} reaches the saturation level which means that the constant voltage level is achieved. In this scenario the above mentioned relation can be expressed by the simplified form and the saturation voltage can be given as:

$$V_{sat} \approx \frac{C_{\max}}{C_{\min}} V_O, \tag{2.2}$$

The number of cycles required to achieve the saturation level can be derived from equation (2.1) and is given as:

$$n = \log_{\frac{C_{Store}}{C_{\min}+C_{Store}}} \frac{V_{sat}/V_O - C_{\max}/C_{\min}}{1-C_{\max}/C_{\min}}, \tag{2.3}$$

The energy build up across C_{Store} is the energy of an equivalent series capacitance made of C_{Res} and C_{Store} and charged equal to the voltage difference between C_{Res} and C_{Store}:

$$\Delta E_{1\to n} = \frac{C_{Res}C_{Store}}{2\left(C_{Res}+C_{Store}\right)}\left(\left(V_{store}\right)_n - \left(V_{Res}\right)_n\right)^2, \tag{2.4}$$

As V_{Res} is nearly constant during the harvester's operation and since C_{Res} is larger than C_{Store}, it simplifies the equation to the form:

$$\Delta E_{1\to n} = \frac{C_{Store}}{2}\left(\left(V_{store}\right)_n - V_{Res}\right)^2, \tag{2.5}$$

Fig. 2.4 represents the evolution of voltage and energy build up across the capacitor C_{Store} as a function of the number of pump cycles using equations (2.1) and (2.5). The losses and voltage drop across the diodes are neglected here. The components values used to generate these curves are: C_{Res} =1 µF, C_{store} = 3.3 nF, C_{MAX} = 200 pF, C_{MIN} = 100pF and V_O = 5 V. The criteria used to determine the component values are explained in next sub-section.

V_1 and V_2 (as marked on the Fig. 2.4), are the voltage levels between V_O and V_{sat}, which correspond to the pump cycles n_1 and n_2 respectively. If the flyback operation is initiated from V_2 (when *Sw* is 'ON') to V_1, the energy stored across C_{Store} will also be reduced from E_2 to E_1. This energy reduction is used to provide power to the load resistance and to recharge C_{Res}. These voltage levels are the main circuit design parameters and their optimization means the maximization of the harvested power. Neglecting the flyback operation time, the mean harvested power can be given as:

$$P = \frac{E_2 - E_1 - E_{Flyback,loss}}{(n_2 - n_1)T}, \tag{2.6}$$

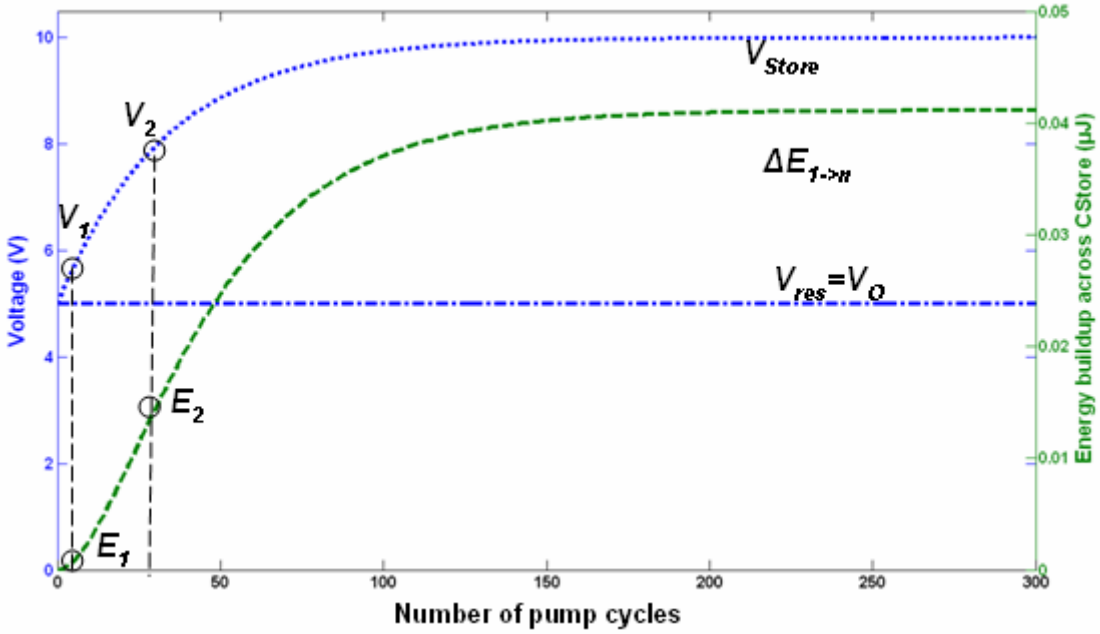

Fig. 2.4 Energy across the C_{store} and voltages on C_{store} and C_{Res} capacitors versus the number of the pump cycle

Where $E_{Flyback,loss}$ is the loss of energy during flyback and T is the duration of one charge pump cycle. The losses associated with diodes are neglected here. To find optimal values of V_1 and V_2, the power as given by equation (2.6) has to be maximized. The flyback should be active in this optimal zone, the region between the optimal values of V_1 and V_2, for maximum power generation. If the values chosen are not optimum, the harvested power can be reduced. This will be discussed in the QV diagram of the charge pump later on.

2.1.1.1 Optimization of the capacitance values

Reservoir capacitance (C_{Res}):

Ideally there should be a DC source in place of the C_{Res} or some condenser with an infinite capacitance value so that its electric charge remains unaffected for long life times. Thus we have chosen the value of 1 μF for C_{Res} which is around 1000 times larger than chosen C_{store} and 10^6 times larger than C_{Var} so that we can maintain V_{Res}.

Storage capacitance (C_{Store}):

The value of C_{store} defines the number of pump cycles required to saturate the charge pump. V_{store} evolves in discrete steps which depend on the ratio of C_{MAX} to C_{MIN} as well as on V_O (ref. equation (2.1)). Fig. 2.5 shows the relationship of V_{store} with the number of cycles and the value of C_{store}. When the value of C_{store} is small, the number of quantized levels to achieve V_{sat} becomes small, limiting the choice of the optimal operation region. The higher the value of C_{store}, the larger the number of pump cycles required to achieve V_{sat}. Fig. 2.6 shows the relationship of harvested energy equation (2.5) with C_{store} and with the number of cycles. The harvested energy increases with the increase in the value of C_{store}, keeping the number of pump cycles constant, however after a certain level the harvested energy start decreasing as the number of pump cycles are not sufficient to bring enough energy to C_{store}. In order to

increase the energy level for larger values of C_{store} we have to increase the number of pump cycles. *So as a conclusion we can say that when C_{store} >> C_{MAX}, the value of C_{store} does not have significant impact on maximal harvested power. The selection of C_{Store} will depend upon the mechanical vibration frequency and the optimal values of V_1 and V_2.* The component values used to generate these curves are: C_{Res} =1 µF, C_{MAX} = 200 pF, C_{MIN} = 100pF and V_O = 5 V.

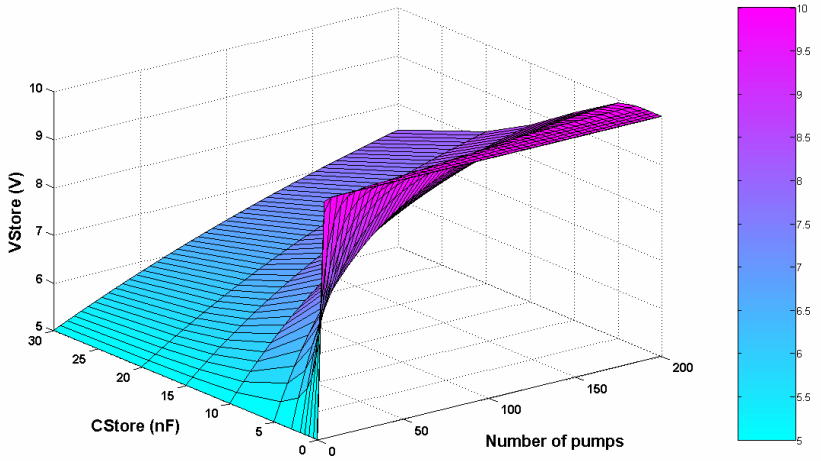

Fig. 2.5 Evolution of V_{Store} with C_{store} and number of pump cycles (C_{Res} = 1 µF, C_{min} = 100 pF)

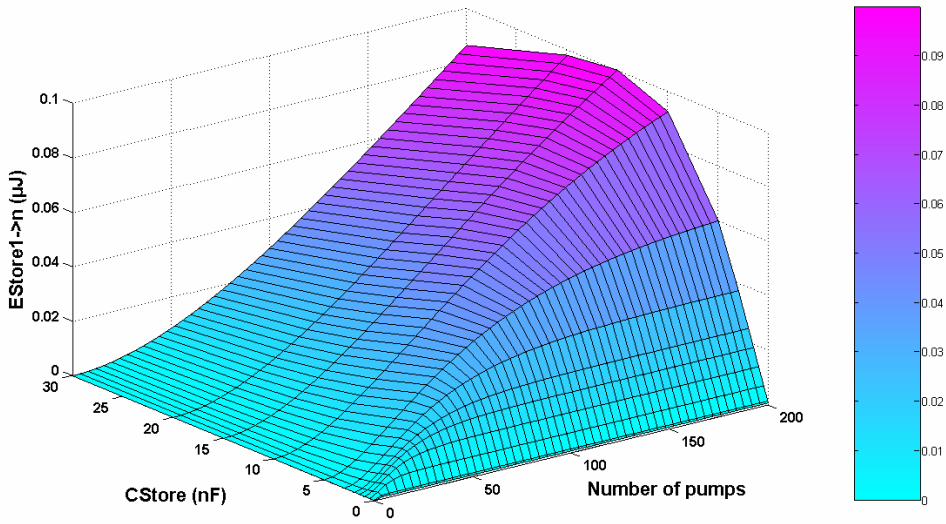

Fig. 2.6 Evolution of $\Delta E_{1->n}$ with C_{store} and number of pump cycles (C_{Res} = 1 µF, C_{min} = 100 pF)

Variable Capacitance (C_{Var}):

C_{Var} varies in between C_{MAX} and C_{MIN}. The value of C_{MAX} should be as high as possible since it defines the energy and the electric charge acquired by C_{Var} from C_{Res} during a pump cycle. As discussed in chapter 1, in an ideal constant charge case with lossless electronics, the energy harvested is directly proportional to the ratio C_{MAX} / C_{MIN} and the difference of C_{MAX} and C_{MIN}.

Now we will study the impact of C_{MIN} on harvested power. Let us suppose that C_{Var} varies with a fixed magnitude between C_{MAX} and C_{MIN} and the value of C_{MIN} is zero. The charge stored on C_{Var} is:

$$Q_o\big|_{C\min=0} = C_{MAX}V_{\mathrm{Re}s}, \tag{2.7}$$

In this case each mechanical cycle brings net charge to C_{Store}. The voltage increase across C_{Store} at each charge pump cycle can be given as:

$$\Delta V_{Store}\big|_{C\min=0} = \frac{C_{MAX}V_{\mathrm{Re}s}}{C_{Store}}, \tag{2.8}$$

The linear increment in voltage is perpetual as the saturation voltage level is infinite (cf. equation (2.2)), this will result in a quadratic increase in the energy build up across C_{Store}. Thus the optimal values of V_1 and V_2 are infinite.

A technological limitation on the value of C_{MIN} is also imposed by the voltage allowed on the chip and the pull-in voltage of the electrostatic transducer. If C_{MIN} is close to zero, the voltage across C_{Var} will approach very high value and can cause destruction of device. Also this high voltage elevation can cause damage to the associated electronics.

Now we will study the impact of C_{MIN} on the energy required to transfer the electric charge from C_{Var} to C_{Store}. Once $C_{Var} = C_{MAX}$, charged at V_{Res} then it should be elevated up to V_{Store} at $C_{Var} = C_{MIN}$. As the charge is kept constant, the energy required for such a potential elevation is:

$$E_{req} = Q_o (V_{Store} - V_{Res}), \tag{2.9}$$

Q_O is the constant charge of the system. If C_{MIN} approaches zero, V_{Store} will also be very high and as a result, more energy will be required for the charge displacement. This energy should be compensated by the mechanical vibrations, but if the energy generated by C_{Var} and the energy described by equation (2.9) are in comparable range, there will be no more energy generation. Fig. 2.7 shows the impact of C_{MIN} on V_{Store}, by elaborating the case where C_{MIN} is approaching to minimum value and the V_{Store} is increasing. Increment in V_{Store} is expected but it also imposes a major technological constraint over the C_{MIN}, as it can cause a pull-in effect. The components values used to generate these curves are: C_{Res} =1 µF, C_{MAX} = 200 pF, C_{Store} = 3.3 nF and V_O = 5 V.

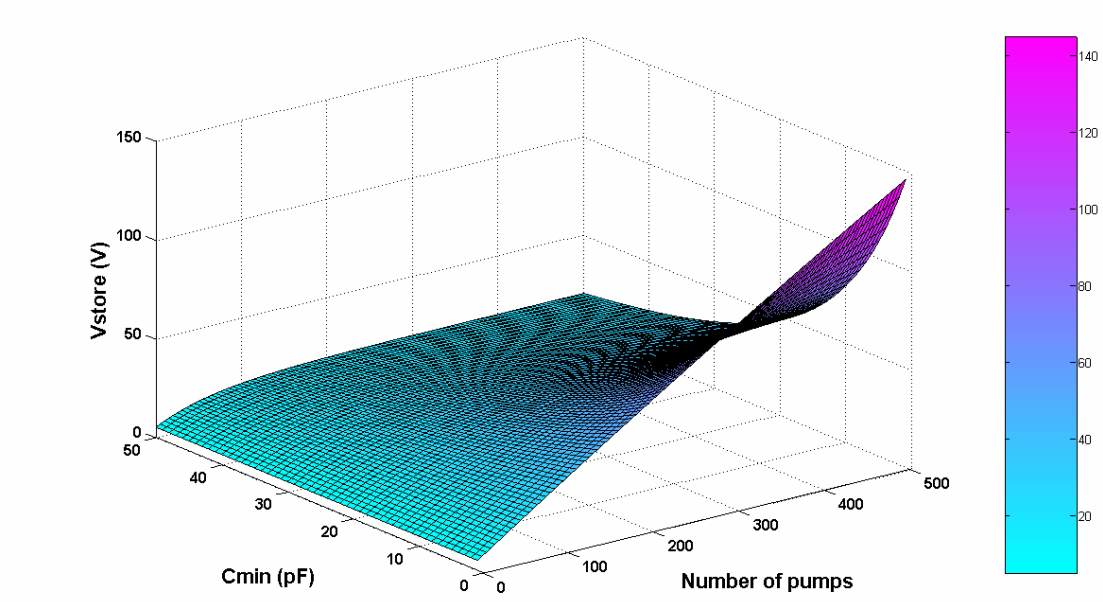

Fig. 2.7 V_{Store} as a function of C_{MIN} and number of pump cycles

2.1.1.2 Diodes selection

Until now in all the analysis, the diode losses and voltage drops are neglected. The diode selection criterion is the low reverse leakage current to avoid the discharge of the initial charge stored in the harvester. The initial charge storage, Q_O, can be given as:

$$Q_O = C_{\max} V_o$$

The reverse leakage current of the diode is given as:

$$I_{reverse} = \frac{Q_{leakage}}{T_{period}}$$

Where $Q_{leakage}$ is the charge loss due to reverse leakage current and T_{period} is the electrical time period of the capacitance variation (one pump cycle of the charge pump). So the diodes must satisfy the following condition:

$$C_{\max} V_o >> I_{reverse} T_{period}\,, \tag{2.11}$$

2.1.1.3 QV-diagram of charge pump operation

Observing the QV diagram of the charge pump operation (Fig. 2.8), one can see that the curve describing the cycle is changing at each cycle. Indeed, if at the beginning (point A) $V_{Res} = V_{store} = V_{var} = V_0$, and $C_{Var} = C_{MAX}$, the first cycle will be triangular (i.e. ΔABC). However, the second cycle will contain an additional point (Abis), and due to an increase in V_{store} the cycle will be a trapeze as it consisting of points A, Abis, Bbis and Cbis instead of a triangle. The next cycle is also trapeze and consists of points A, A'bis, B'bis and C'bis and the net surface area of the trapezoid, corresponding to each cycle, increases. It is known that the area of the clockwise QV cycle is numerically equal to the harvested energy [5]. The second cycle generates more energy than the first cycle as the surface area of the trapezoid is higher as compared to the triangle. The trapezoid corresponding to the third pump cycle has more surface area and thus able to generate more energy. From the left and from the right sides, the *QV* diagram is bounded by the lines corresponding to C_{MIN} and C_{MAX} values of the variable capacitance : $Q=C_{MIN}V$ and $Q= C_{MAX}$V. Hence the lines $Q=C_{MIN}V$ and $Q= C_{MAX}$V fix the maximal value of V_{store}, which is equal to $V_0\ C_{MAX}\ /\ C_{MIN}$ and called as "saturation voltage". When V_{store} is close to $V_{store,sat}$, the cycle is very thin, and at *n* reaching infinity, it

transforms itself from trapezoid to a line, thus we can say that there will be no more power generation. Hence, we conclude that there is an optimal cycle number at which the pump harvests the maximal amount of energy. The flyback should be active in this optimal zone for maximum power generation.

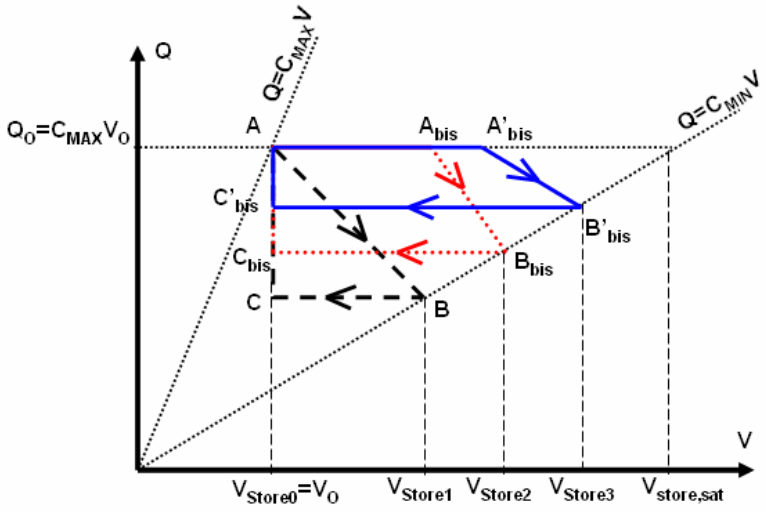

Fig. 2.8 QV diagram of the charge pump operation

2.1.2 Flyback operation

The charge pump operation is not symmetric in time, and only during some limited time interval the pump generates the maximal power. To guarantee a continuous power generation, a flyback circuit is needed. It has two roles: first, to return the charge pump to some earlier state in order to keep its operation in the optimal zone, second, to extract the harvested energy from the charge pump and deliver it to attached load resistance. This is achieved with the flyback circuit whose architecture has been inspired from the BUCK DC-DC converter architecture [1] (Fig. 2.3). It is composed of a diode D_{FLY} and an inductor L_{FLY}. The principle of operation is as follows. When the switch becomes ON, the LC circuit $C_{Res}C_{Store}L_{FLY}$ (in which two capacitors and an inductor are connected in series) starts to oscillate with the following initial condition: I_L=0, C_{Store} discharges, and the inductor accumulates the energy. When the difference between V_{Store} and V_{Res} decreases sufficiently to

return the charge pump at the beginning of the optimal operation zone (V1), the switch opens and the inductor discharges on C_{Res} capacitance providing electrical charges to it. Hence excessive energy generated by the vibrations is delivered to the load resistance.

In practice there are always power losses which are associated with the flyback operation (losses in inductor, switching power etc.). For this reason, the frequency of the flyback circuit activation should be as low as possible. On the other hand, enlarging the operating zone of the charge pump reduces the harvested power. These two opposite factors provide an optimal range of the operating zone of a charge pump: the start and the end of the C_{Res} voltage which we called V_1 and V_2 earlier (equation (2.6) and Fig. 2.4). The resulting system operation is being presented in Fig. 2.9.

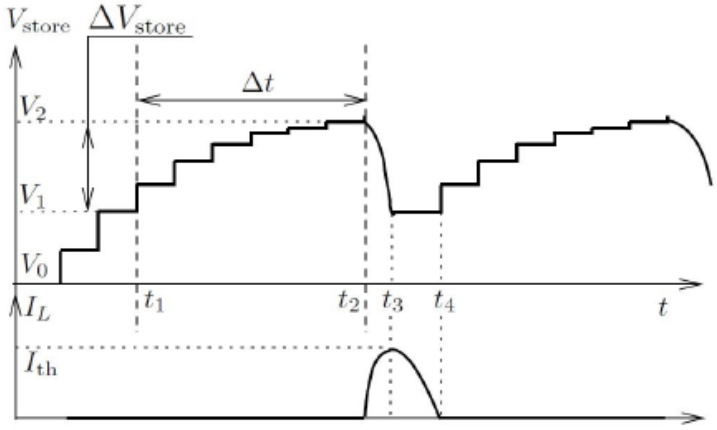

Fig. 2.9 Voltage build up and inductor current with optimal circuit operation

Note: In the context of this thesis, we established formulation of the energy generated by the electromechanical transduction using the charge pump. The flyback part has not been implemented in this work. But the work is underway to build up an intelligent switch for the flyback to have the complete system [6].

2.2 Choice of topology

We have already discussed in chapter 1, that there are four major configurations of variable capacitors, which are being employed in the energy harvesting applications based on electrostatic transduction. The choice among, In-Plane Overlap Comb (IPOC), In-Plane Gap-closing Comb (IPGC), Out-of-Plane Gap-closing Plate (OPGP) and In-Plane Overlap Plates (IPOP) topologies depends on the required application. But still in order to select the most appropriate topology, we need to establish some criteria, which can be given as:

1) Power generation
2) Stability against out-of-axis vibration
3) Ease of fabrication
4) Fluid damping

The most important criterion is the *highest power generation*. As discussed in 1.3.1, the highest attainable power density depends on three factors: 1) the initial voltage keeping in view the possibility of pull-in due to high voltage and eventual damage of device, 2) the capacitance variation and 3) the maximum capacitance. As most designs are unidirectional, *stability against out of axis vibration* is compulsory to avoid electrode stiction, which can cause a short circuit between two sets of electrodes. The device *fabrication process* should be simple. *Fluid damping* acts as a mechanical resistance, responsible for losses and should be minimized. It is in fact the result of two major components: Couette damping and squeeze film damping. Couette damping exists between two flat surfaces which are moving in parallel to each other. Squeeze film damping originates due to the compression of air between the moving object and the fixed object. Damping has a direct relationship with the bandwidth. If the intended application has a very specific resonance frequency with the high required value of a mechanical Q-factor, we would prefer low damping. On the other hand if the targeted application has comparatively large bandwidth then an optimal value can possibly be

determined between the Q-factor and the bandwidth. However we should keep it in our mind that reducing Q-factor is not a good idea as it can bring the generated power down with it [7].

2.2.1 Advantages & disadvantages of IPOP topology

Keeping in view all four types of electrostatic energy harvesters and the selection criteria described above, ***a resonant energy harvester based on an IPOP mechanism is being proposed***. The main *advantages* are:

1) In order to have high capacitance value, small gap between top and bottom electrodes can be attained.
2) Use of a thick silicon substrate can increase vertical stiffness, which can resist out-of-axis vibration. IPOC has the electrode stiction problem in case of rotational vibrations [5]. Even IPGC needs, most of the times, a mechanical stopper to avoid the stiction problem [5], but in case of IPOP this problem does not exist as there is no chance of electrode stiction in case of rotational vibrations.
3) IPOP and IPOC provide an additional advantage of reduced fluid damping as there is no compression of air between movable and fixed electrodes, thus squeeze film damping does not exist, which is maximum in case of OPGP. Hence, IPOP and IPOC are best compatible with narrow bandwidth, fixed mechanical resonance frequency applications.
4) Fabrication process for IPOP is easy as there are no closely spaced comb electrodes. Achieving higher capacitance in IPOC and IPGC is not as easy as it is in the case of IPOP and OPGP having the same surface area, because we need to increase the number of comb electrodes which in result makes the process of DRIE more complicated. This is primarily because it can make

through wafer etching very difficult, keeping high aspect ratio of mechanical spring, as well as avoiding critical losses and notching effects. SOI wafer is normally being used in the cases of IPOC and IPGC to avoid above mentioned problems but it makes the process bit expensive, whereas on the other hand IPOP can be fabricated using an ordinary silicon wafer.

The *disadvantage* with IPOP configuration is that it is more prone to pull-in problem at small voltages, as compared to IPOC and IPGC. This factor is even important for low frequency vibration sources as the designs for low frequency are less stiff, hence pull-in is hard to avoid at low voltages.

2.2.2 Capacitance model for IPOP configuration

In this sub section a capacitance model for the variable capacitor based on the IPOP configuration is developed. In order to model the IPOP based transducer, consider three electrodes system as shown in Fig. 2.10. The two bottom electrodes are stationary and are connected electrically. The top electrode moves laterally and the capacitance varies.

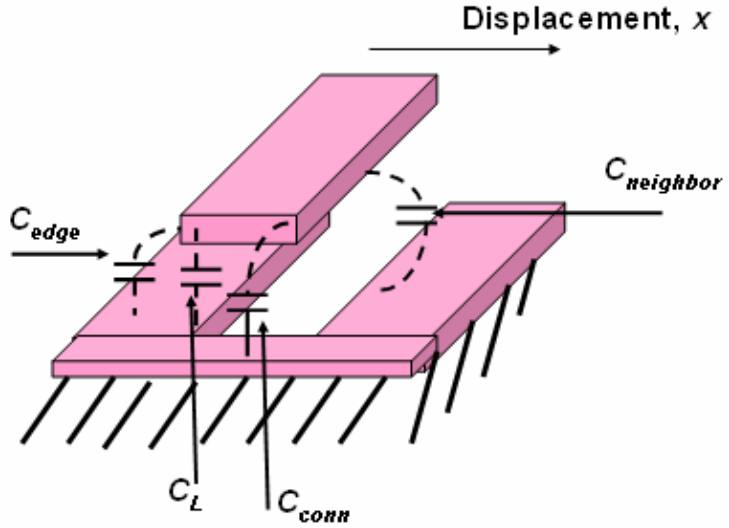

Fig. 2.10 Three electrode system with two fixed bottom electrodes electrically connected and one movable top electrode

There are four major types of capacitance contributing in the total capacitance which can be written mathematically as:

$$C_{TOT}(x) = C_L(x) + C_{neighbor}(x) + C_{edge}(x) + C_{conn}\,, \tag{2.12}$$

where $C_{neighbor}$ is the fringe capacitance due to the presence of neighboring electrode (front electrode), C_{edge} is the edge capacitance present between the top and bottom (back) electrodes, C_{conn} is the parasitic capacitance due to electrical connection, C_L is the linear capacitance due to overlapping of top and bottom electrodes, and can be written as:

$$C_L(x) = \frac{\varepsilon_O L(w - |x|)}{d}, \tag{2.13}$$

where ε_O, L, w, x and d are the permittivity of dielectric, length, width of an electrode, displacement of the top electrode and an air-gap between the top and bottom electrodes, respectively. In order to model the fringing capacitance because of neighboring electrodes and edge effects, the relation presented in [8] is being utilized i.e.:

$$C_{fringe} = \frac{2\pi\alpha\varepsilon_O L}{\ln\left(\dfrac{(l-r)(l-R)}{rR}\right)}, \tag{2.14}$$

Here R, l, α and r are given as in [8]:

$$\begin{aligned} r &= 0.5t \\ b &= w - x \\ l &= \frac{b + t + 0.5w}{b + t}\sqrt{(b+t)^2 + (d+t)^2} \\ R &= \frac{0.5w}{b+t}\sqrt{(b+t)^2 + (d+t)^2} - r \\ \alpha &= \frac{0.002826 + (t/w)^2}{0.001894 + (t/w)^2}\left[1.17059 - \left(\frac{1.29413}{b + 3.1937}\right)^2\right] \end{aligned}\,, \tag{2.15}$$

Here t represents the thickness of each electrode.

On the other hand, the three electrode system (cf. Fig. 2.11) was also simulated using Finite Element Modeling (FEM) in the *coventorware*^{tm} commercial software. The dimensions used for each electrode is *100 μm x 50 μm.* We used equations (2.13), (2.14) and (2.15) in

equation (2.12) to have analytical capacitance value. The value of C_{conn} is found to be 1 fF from the FEM simulations. Fig. 2.11 shows the comparison between simulated and calculated values using equation (12). The graph shows quite a good match. There exists a constant error of 0.5 fF which emerges as we have not modeled the edge effects along width of the electrodes. This capacitance model will be introduced later in a VHDL-AMS code to simulate and study the global system.

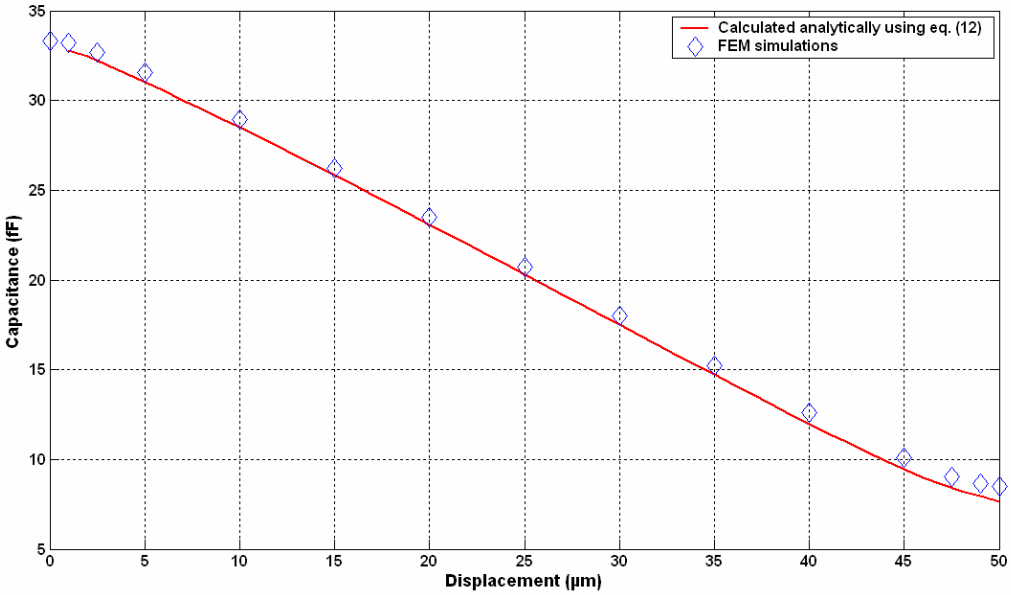

Fig. 2.11 Comparison of FEM simulations based calculated capacitance with analytically calculated capacitance

2.3 Design of silicon based electromechanical resonator: architecture & dimensioning

Based on the IPOP configuration we propose two designs of the mechanical resonator called as: 1) Proof mass Configuration (PC) and 2) Comb Configuration (CC). In this sub-section we will discuss the dimensioning of these proposed designs. The following constraints are fixed:

- Area of transducer (proof mass + spring) = 1.03125 x 0.64 cm²
- Area of contact pads 0.2 x 0.12 cm²
- Lateral resonance frequency, f_x = 250 Hz
- Ratio of lateral to vertical resonance frequency > 10
- Pull-in voltage > 10 V

The technological constraints are imposed by DRIE. As our structures have spacing of different sizes from 50 µm (gaps between springs and electrodes) to few millimeters (the contact pads to access electrodes), thus the aspect ratio is variable throughout the wafer due to the so-called *loading effect* during DRIE micromachining. With such non-uniform aspect ratio, the minimum achievable spring width is 30 µm which analytically gives f_x = 250 Hz with other constraints. Fig. 2.12 shows the top view of PC along with dimensions of the transducer and the contact pads.

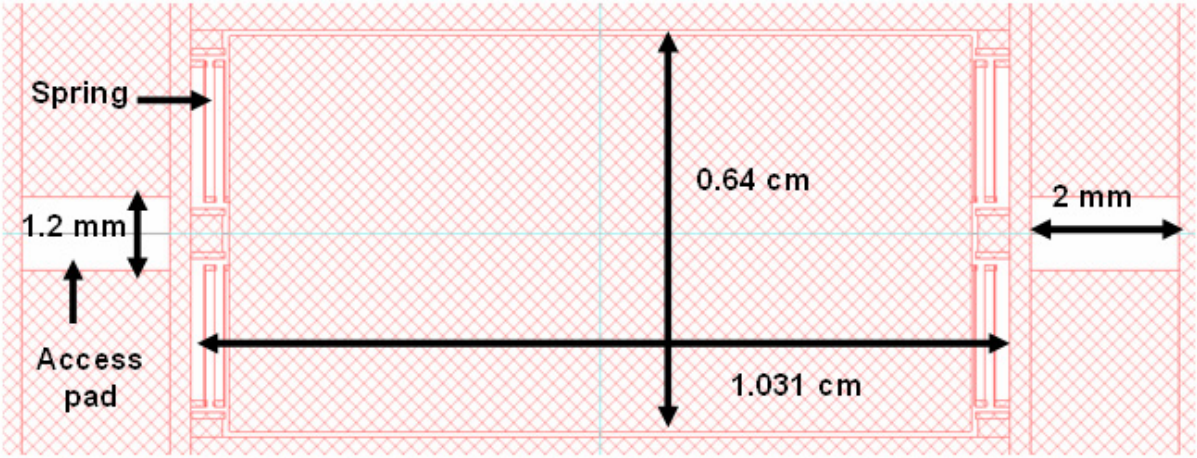

Fig. 2.12 Schematic top view of PC (with all dimensions)

Now the method used to determine the mechanical features of harvesters is discussed in the following.

The mass of the proof mass (m) is calculated by multiplying the proof mass volume by the bulk silicon density i.e. 2330 kg/m^3. For a single mass-spring system, the lateral resonance frequency of the system is given as:

$$f_x = \frac{1}{2\pi}\sqrt{\frac{k_x}{m}}\ , \tag{2.16}$$

where k_x is the lateral spring stiffness of the system. We can reasonably use this expression of f_x to calculate the overall value of k_x.

The total spring constant (k_x) should be divided by 4 to have each spring constant which is connected to the proof mass. Now we assume that each spring is the connection of various standard beams in series connected by the rigid links as shown in Fig. 2.13.

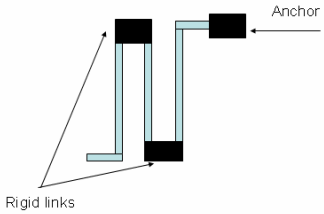

Fig. 2.13 Serpentine spring with rigid links

The stiffness of a single beam can be determined, using the boundary condition of a fixed-guided beam in the lateral direction, as follows.

$$k_{cantlever,x} = \frac{Etw^3}{l^3}, \tag{2.17}$$

Once the stiffness of a single beam is determined at each support point of the proof mass, the number of beams, which are to be connected in a series giving same net stiffness, can be calculated. So we will have the serpentine beam having previously mentioned beams in series (cf. Fig. 2.14). The stiffness in the vertical directions can also be determined using the boundary conditions of a fixed-guided beam for serpentine beam. In the IPOP configuration the major type of damping which is considered is the Couette damping. Mathematically it can be written as:

$$b_m = \frac{\mu S}{h}, \tag{2.18}$$

where μ, S and h are fluid viscosity having the value of 1.8e-5 Ns/m² (when the fluid is air), the surface area of the proof mass and the air gap present between movable and fixed part, respectively. Q factor of the resonator is then calculated by the expression:

$$Q = \frac{\sqrt{mk_x}}{b_m}, \tag{2.19}$$

The last parameter which is quite important in the design is the pull-in voltage of the harvester. The pull-in voltage is given as [9]:

$$V_{PULL-IN} = \sqrt{\frac{8k_z h^3}{27\varepsilon_O S}}, \tag{2.20}$$

Here k_z, *is* the vertical stiffness of the mechanical springs.

2.3.1 Dimensions of Proof mass Configuration (PC)

Fig. 2.14 shows 3D-view of the energy harvester based on the IPOP topology. Top electrodes are patterned on the underside of the silicon-based proof mass.

Fig. 2.15 shows the bottom view of the proof mass configuration with patterned electrodes.

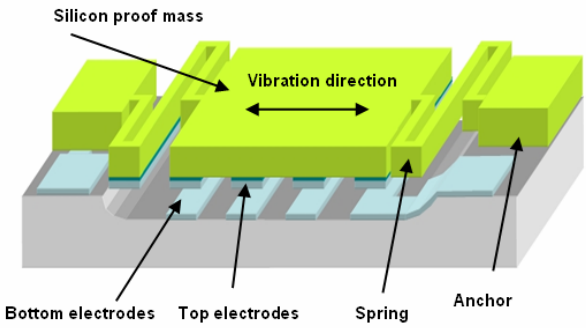

Fig. 2.14 Proposed energy harvester design: Proof mass Configuration (PC)

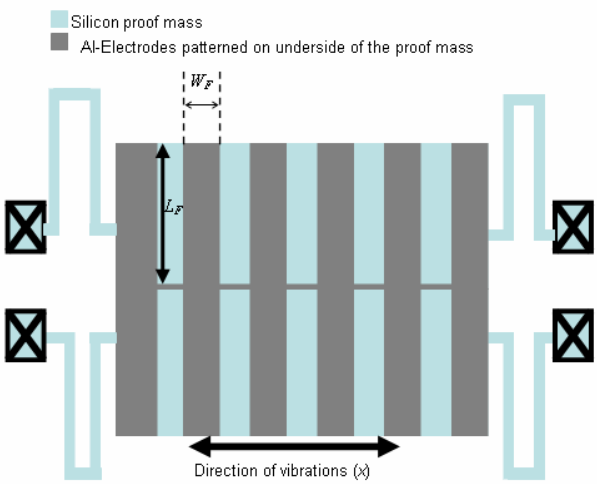

Fig. 2.15 Bottom view of the full proof mass configuration with the patterned electrodes

The theoretical ***mechanical features of the PC based energy harvester*** are summarized below:

Mass of the proof mass	59.684 mg
Lateral and vertical resonance frequencies	250 Hz and 3464 Hz
Fluid damping *b*	7.68e-4 Ns/m
Q-factor	146

Table 2.1 Mechanical features of PC

2.3.1.1 Electrodes design

Now the next part of the design is the electrical behavior of the energy harvester i.e. the capacitance variation of the design. The electrodes patterned underneath the proof mass have the length which is same as the width of the proof mass i.e. 6.4 mm, whereas the width of each electrode is 50 µm and total number of electrode pairs is 100. The width of the electrodes deposited on the glass is determined by FEM simulations, performed using *Coventorware*^{tm}. To make simulations faster, a three electrodes system as shown in Fig. 2.11 (one electrode at top and two at bottom) has been simulated, with each electrode having the length of 100 µm and thickness of 0.5 µm. The simulation was also performed for a lower

electrode width of 35, 40, 45 and 50 µm. As discussed in chapter 1, the theoretical maximum generated energy with lossless electronics is:

$$E = \frac{1}{2} V_o^2 C_{\max} \left(\frac{C_{\max}}{C_{\min}} - 1 \right), \tag{2.21}$$

From the aforementioned expression, it is evident that the energy generated is directly proportional to the factor $C_{\max}\left(\frac{C_{\max}}{C_{\min}}-1\right)$ (let it termed as *Energy Factor* EF). We have calculated EF for each case and Fig. 2.16 shows the plot of EF versus lower electrode width, pointing out that the 40 µm lower electrode width is an optimum value.

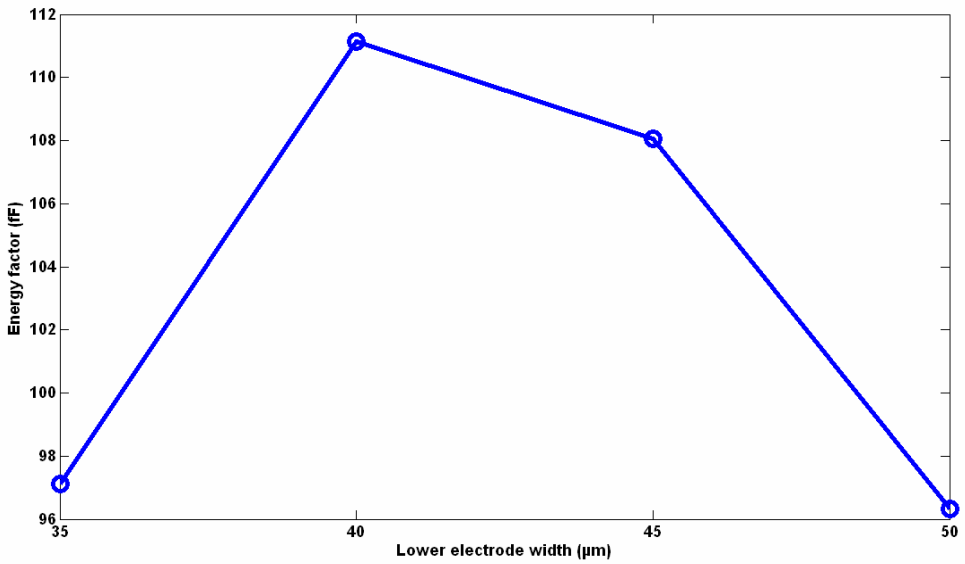

Fig. 2.16 Plot of Energy factor versus the lower electrode width

2.3.1.2 Capacitance variation

Now we will study the capacitance variation keeping in view the effect of the substrate capacitance, by simulating the two-pair electrode system with the silicon substrate and extrapolating the result for the 100 electrode pairs. Fig. 2.17 shows the cross section of the device being simulated. The net capacitance of the harvester is the sum of the linear overlap capacitance, the fringe capacitance (including the edge effects and the effect of the

neighboring electrodes) and the substrate capacitance. Fig. 2.17 shows all capacitances where C_L, C_S, C_{S2}, C_{F1} and C_{F2} represent the linear overlap capacitance, the substrate capacitance, the substrate capacitance with top electrodes, the fringe capacitance due to neighboring electrodes and the fringe capacitance due to edge effects, respectively. As the proof mass displaces towards the right as shown in Fig. 2.17 (b), C_L reduces to zero due to reduction in the overlap area of top and bottom electrodes, C_S increases due to increase in the substrate overlap with the bottom electrodes. Fig. 2.18 shows the FEM simulations based study of the substrate and the fringe capacitance. In the simulations the ground was applied to the substrate and top electrodes hence C_{S2} is zero. When the electrodes are not superposing each other at the minimum capacitance position, the net capacitance, in practice, is equal to the fringe capacitance and substrate capacitance. Mathematically net capacitance, C_{TOT} can be given as:

$$C_{TOT}(x) = C_L(x) + C_F(x) + C_S(x), \tag{2.22}$$

where C_L has been already mentioned in equation (2.13). The FEM simulations of the system shown in Fig. 2.17, give us C_{TOT}. The simulations of the aluminum electrodes (without taking in account the substrate), give us C_{LF}, the sum of the linear capacitance and the fringe capacitance. C_S is found from the equation (2.22):

$$C_s(x) = C_{TOT}(x) - C_{LF}(x), \tag{2.23}$$

Net fringe field can be determined by subtracting C_L from C_{LF}. Next step is to calculate the net power generated in an ideal case using equation (2.21). We can do so by multiplying the result of equation (2.21) with twice the resonance frequency (250 Hz), since in a single period the device capacitance reaches C_{min} two times. For V_{in} equals to 5V and 6 V, the harvested power (with C_{MAX} = 199 pF and C_{MIN}=135 pF) would be 0.5 µW and 0.85 µW respectively (using equation (2.21)). The value of pull in voltage calculated by equation (2.20) is around 10 V.

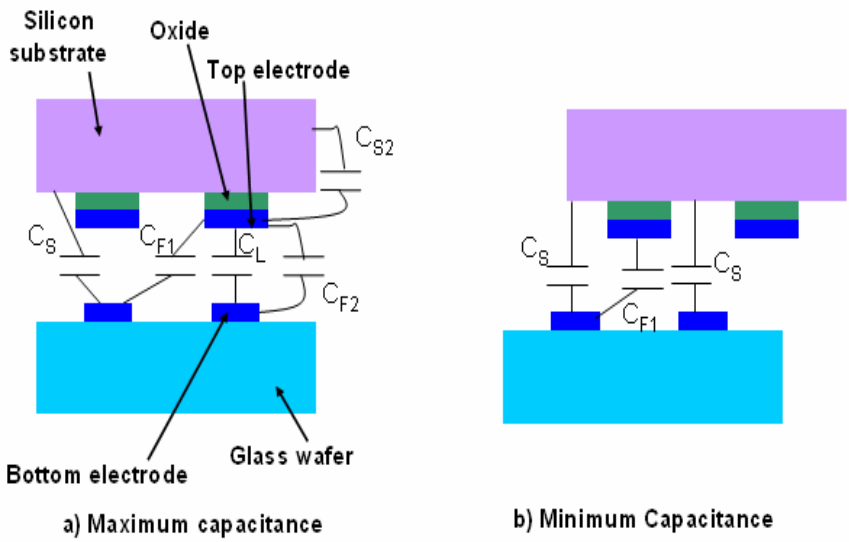

Fig. 2.17 Various phases of the capacitance variation and the corresponding parasitic capacitances

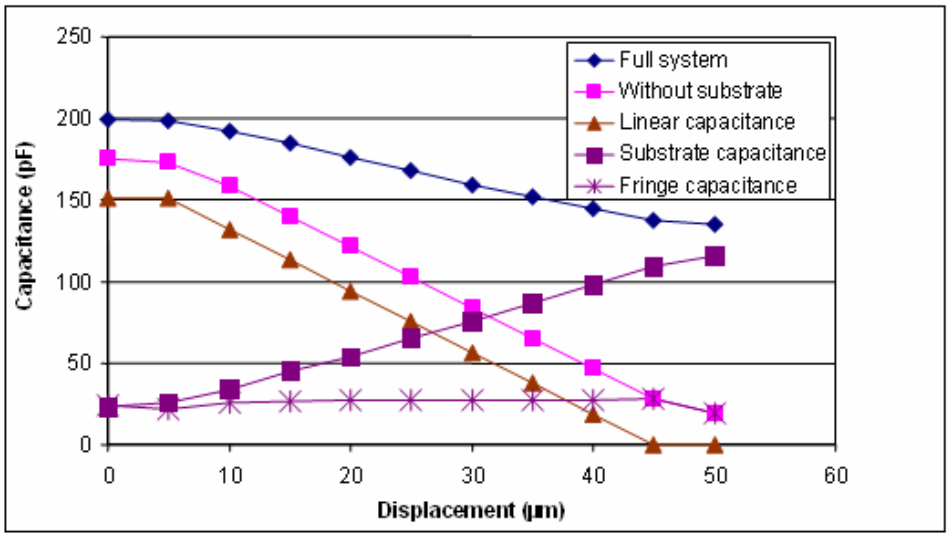

Fig. 2.18 Substrate capacitance, fringe capacitance and linear capacitance (eq. 13) for the PC with the lower electrode width 40 µm

2.3.2 Dimensions of Comb Configuration (CC)

The next architecture is the modification of a PC configuration. The major problem lies with the PC configuration is the high value of the parasitic capacitance (substrate capacitance). Now keeping the same surface area of the device, the ratio of maximum to minimum capacitance should be increased. So the proposed solution is the removal of silicon from the space present in between electrodes to reduce the parasitic capacitance. It also results

in the reduction of overall mass of the device, hence increasing its natural frequency as compared to the proof mass configuration (PC), having the same dimensions. So once the mass is reduced, the spring stiffness should be adjusted to make the harvester suitable for the low frequency vibration sources. Fig. 2.19 shows the 3D-view of device and Fig. 2.20 shows the backside of the proof mass.

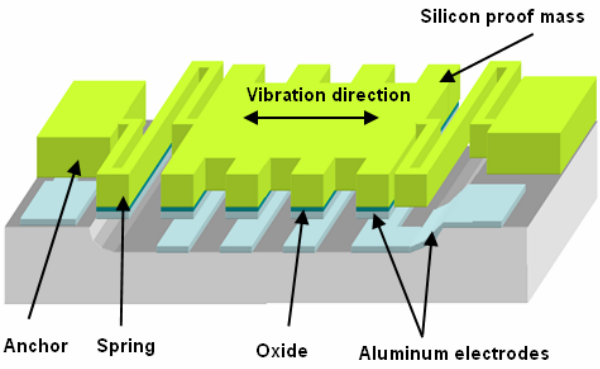

Fig. 2.19 Proposed energy harvester design: Comb Configuration (CC)

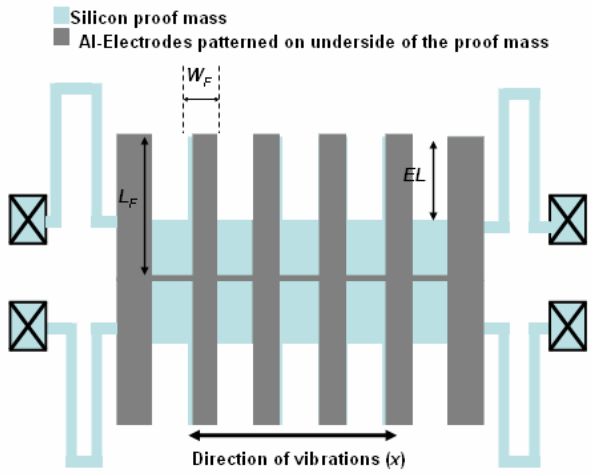

Fig. 2.20 Bottom view of the comb configuration with the patterned electrodes and the space etched between the electrodes

EL in Fig. 2.20 is the length of silicon to be etched completely from the space present between electrodes. FEM based simulations have been made to see the impact of etched length on the values of maximum and minimum capacitance. The simulation results are shown in Fig. 2.21. Increase in etched length does not affect the value of maximum

capacitance but the value of minimum capacitance reduces linearly. The chosen value for the length *EL* is 1.2 mm, as it gives the ratio of maximum to minimum capacitance around 2. The higher the value of *EL,* the larger the capacitance ratio but as we are targeting low frequency vibration sources we cannot afford to loose large mass.

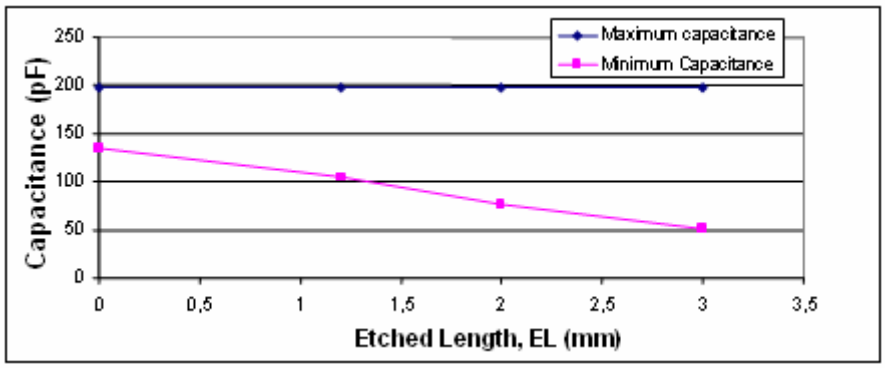

Fig. 2.21 Impact of EL over maximum and minimum capacitance

The theoretical ***mechanical features of CC based energy harvester*** are summarized below:

Mass of the proof mass	48.5 mg
Lateral and vertical resonance frequencies	250 Hz and 3998 Hz
Pull-in voltage	10 V

Table 2.2 Mechanical features of CC

The lower electrode width is chosen 40 µm which is the same as it was in case of PC configuration. Fig. 2.22 shows the plot of C_L, C_S, and C_F (defined in Fig. 2.18) based upon the FEM simulations and calculation mentioned in equations (2.22) and (2.23). Like PC, simulations are performed for two pairs of electrodes and extrapolated up to 100 pairs.

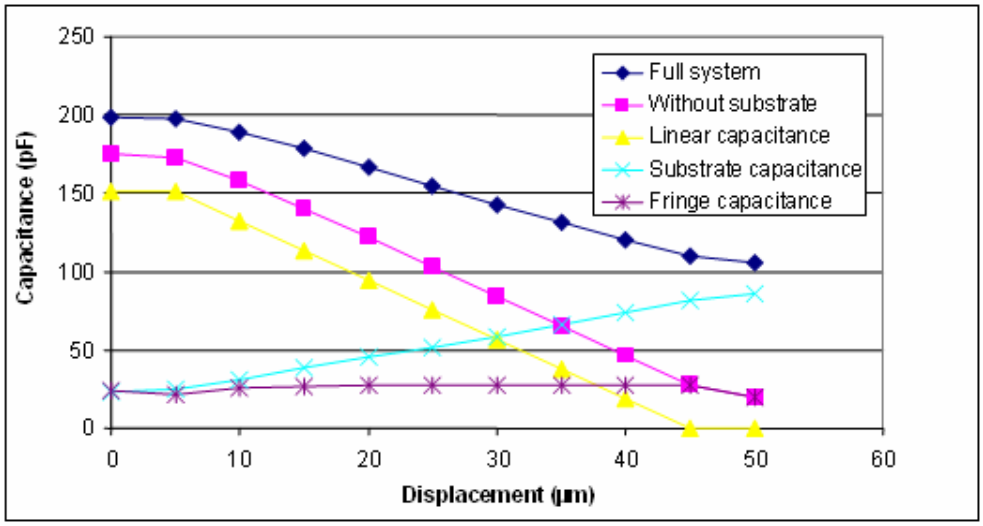

Fig. 2.22 Substrate capacitance, fringe capacitance and linear capacitance for the CC configuration with the lower electrode width equal to 40 µm

Using equation (2.21) for ideal case with lossless electronics and for V_{in} equal to 5V and 6 V, the maximum harvested power (with C_{MAX} = 198 pF and C_{MIN}=105 pF) for 250 Hz would be 1.1 µWand 1.58 µW respectively.

2.3.3 Modification of design with backside DRIE (BD)

In the CC configuration, 19% of the total mass of silicon is removed as compared to the PC configuration, resulting also in a decrease of the parasitic capacitance, hence giving a higher generated power density. But this mass reduction undesirably increases the resonance frequency of the device. So spring stiffness should be reduced to make system suitable for low frequency applications, as the resonance frequencies of most useful vibration sources lie below 250 Hz. In order to achieve a system which can work at such a low frequency, we cannot afford to loose a huge mass. Hence some improvements are required to reduce the parasitic capacitance but without sacrificing too much mass.

Electric field inside the silicon acts as a big parasitic capacitance. It is strong near the top electrodes when they are positioned at a minimum capacitance point because there is a direct overlap of the silicon substrate and aluminum electrodes on glass wafer. So in order to

reduce the parasitic capacitance, the silicon which is placed between the electrodes and are having a high permittivity and conductivity should be replaced by air. It can be done by through-wafer etching as we did in case of CC but it has an inbuilt problem of mass loss. To avoid this inconvenience, we propose to etch small depth of silicon present in between the top electrodes. This step is called as *Backside DRIE* (hence the name BD for this new configuration). Fig. 2.23 shows a side view of the modified design. Fig. 2.24 shows the variation in C_{max} and C_{min} as a function of backside DRIE depth, based on FEM simulations, using *Coventorware*^{tm}. So it can be concluded that through-wafer etching is not mandatory. The value of C_{min} decreases quite rapidly with an etched depth, and after 20 µm it almost becomes constant. At this point backside DRIE results in only 2.5% mass loss as compared to 19% in CC configuration. The backside DRIE has no notable effect on the value of C_{max}. This minor mass change improves our capacitance variation, from 64 pF (in case of PC) and 93 pF (for CC) to 141 pF for this last BD configuration. Based on these FEM simulation results, we can estimate an improvement in our power density. At a resonance frequency of 253 Hz (as the loss of mass increases the resonance frequency from 250 Hz) with the lossless ideal electronic circuit, and the starting voltage of 6 V, the generated power can be estimated using equation (2.21) i.e. 5.13 µW, corresponding to a 3X as compared to the CC configuration and to a 6X improvement as compared to the PC configuration.

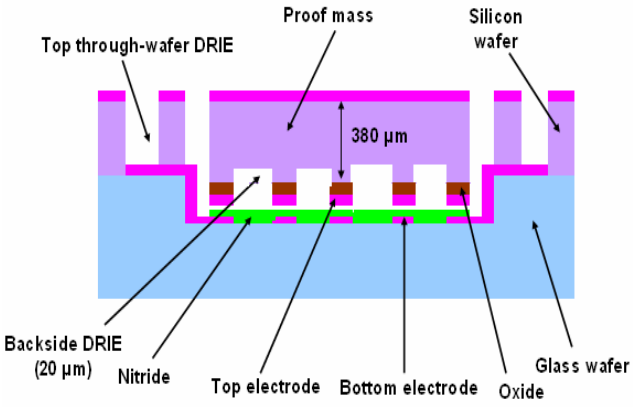

Fig. 2.23 Modified design with backside DRIE (BD configuration)

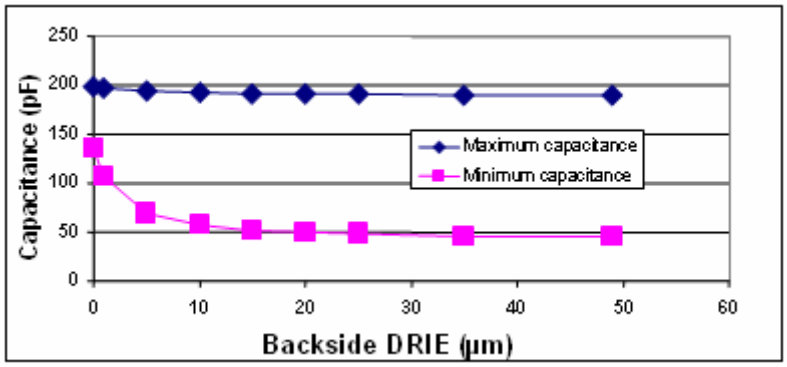

Fig. 2.24 Effect of backside DRIE depth on maximum and minimum capacitance C_{max} and C_{min} (FEM simulation based result)

2.4 Conclusions

This chapter is focused on the design of a silicon-based miniature harvester of mechanical vibration energy, utilizing electret-free electrostatic transducers.

First, we presented the analysis of global system based upon the charge pump and the flyback system. The effect of charge pump components upon the power generated by the transducer has been studied. About the charge pump, it can be concluded that:

1) The value of reservoir capacitance should be kept as high as possible.

2) There is an optimum range for the number of pump cycles, which is also related to an optimum range of operation voltages (V1 and V2), leading to maximum power.

3) The selection of storage capacitance depends upon the mechanical vibration frequency as this value defines the number of pump cycles to saturate the charge pump.

4) The minimum capacitance of transducer cannot be kept to (and even approaching) zero as it can result in device destruction by provoking pull-in.

Then, we have also discussed the criteria for the choice of topologies amongst electrostatic based energy harvesters and on the basis of that discussion; IPOP is selected because of power generation, stability against out-of-axis vibration and fabrication ease. Despite

of above advantages they also exhibit the problem of pull-in at low voltage. The importance of electrostatic fringe effect as well as other parasitic capacitance was highlighted through FEM simulations, which were also compared with a semi-empirical analytic model found in the literature.

Finally we discussed the architectures and dimensioning of IPOP based Proof mass Configuration (PC), Comb Configurations (CC) energy harvesters. The theoretical value of the power, generated with the lossless electronics, and 6 V start voltage with 250 Hz vibration frequency, for PC and CC is 0.85 μW and 1.58 μW, respectively. These values are calculated by equation (2.21). At the end it is proposed that power can be increased by reducing the substrate capacitance without sacrificing a huge mass as in case of CC configuration. For that purpose backside DRIE (BD) configuration has been proposed. The frequency is increased from 250 Hz to 253 Hz. The power generated using equation (2.21) becomes 5.17 μW with 6 V initial voltage, which corresponds to a 6X improvement as compared to the initial PC configuration design.

Reference:

[1] B. C. Yen, H. L. Jeffery, "A variable capacitance vibration-to-electric energy harvester", *IEEE trans. on circuits and systems*, vol. 53, no. 2, *pp. 288-295* Feb. 2006,.

[2] G. Despesse *et al.,* "Fabrication and Characterization of High Damping Electrostatic Micro Devices for Vibration Energy Scavenging", *Proc. of DTIP'05*, pp. 386-390, 2005.

[3] M. Miyazaki *et al.,* "Electric-energy generation using variable-capacitive resonator for power-free LSI: efficiency analysis and fundamental experiment" *ISLPED'03* pp 193–198, 2003.

[4] S. Roundy, P. K. Wright, K. S. J. Pister, "Micro-electrostatic vibration-to-electricity converters", *Proc. of IMECE'02*, pp. 1-9, 2002

[5] S. Meninger *et al.*, "Vibration-to-electric energy conversion", *IEEE Trans. on VLSI*, vol. 9, no. 1, pp. 64-76, 2001

[6] D. Galayko, *et al.*, "AMS modeling of controlled switch for design optimization of capacitive vibration energy harvester", *Proc. of IEEE Int. Behavioral Modeling and Simulation Conf. (BMAS'07),* pp. 115-120, 2007

[7] José Oscar Mur Miranda, "Electrostatic vibration to electric energy conversion", PhD thesis, Massachusetts Institute of Technology (MIT), February 2004.

[8] Magdy F. Iskander, "Electromagnetic Fields & Waves", Prentice-Hall, Inc., 1992

[9] S. Chowdhury *et al.,* "A Comparison of Pull-in Voltage Calculation Methods for MEMS-Based Electrostatic Actuator Design", *Proc. of 1st International Conference on Sensing Technology*, 2005

Chapter 3
Fabrication and Characterization of the energy harvester

This chapter focuses on micro-fabrication and testing of a vibration powered energy harvester which is based on a silicon and glass technology, and uses electrostatic mean of transduction. At first we will present the detailed explanation of manufacturing process of the micro-machined energy harvester and at second stage we will elaborate its characterization. It includes the following measurements:

1) The electrical characterization, in which we will obtain the dynamic variations of the transducer's capacitance.
2) The measurement of the mechanical Q-factor of the resonator.
3) The last step in characterization is to quantify the electrical power which is converted from the mechanical vibrations using the fabricated harvester implanted in a charge pump circuit. We have also compared these power measurements with the simulated results of a VHDL/ELDO based model, using *AdvanceMS* Environment[1].

3.1 Micro-fabrication process

We have fabricated an IPOP based electrostatic energy harvesters using a silicon glass technology [1]. The fabrication involves parallel processing of electrodes deposition on a silicon wafer and on a glass wafer, after which both of them are anodically bonded.

[1] This part of the work is being done in collaboration with Dr. D. Galayko from LIP-6 Paris.

Step number	Graphical description	Explanation
1		Glass wafer (500 µm), 1.7 µm depth is chemically etched by using HF (Mask 1)
2		Sputtering of aluminum (0.5 µm) as lower electrodes, photolithography and etching (Mask 2)
3		Nitride deposition by PECVD (0.2 µm), photolithography and dry etch (Mask 3)
4		Thermal oxidation (0.5 µm) + sputtering of aluminum electrodes (0.5 µm) on silicon back side, photolithography, RIE etching of oxide and aluminum (Mask 4)
5	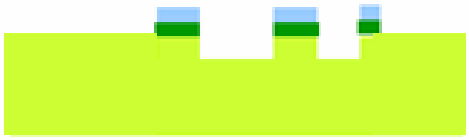	Back side DRIE (20 µm) (Mask 5)
6		Aluminum-sputtering (0.5 µm) as a hard mask for subsequent DRIE (Mask 6)
7	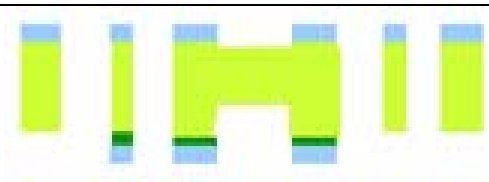	Through wafer DRIE (380 µm)
8		Anodic bonding of two substrates

Fig. 3.1 Micro-Fabrication process

In this process ordinary, cheap, 100-oriented, 380 μm-thick double-side polished, 4" silicon and 500 μm-thick glass wafers are used. There are six levels of masks required for the fabrication. The steps are shown in Fig. 3.1.

In order to avoid unwanted top and bottom electrodes stiction, 2000 Å thick nitride layer is deposited through PECVD as a passivation layer, on the lower electrodes, which are deposited on a glass wafer previously etched by HF. The deposition of a thermal oxide on the silicon wafer insulates this conductive substrate from the aluminum electrodes. A small quantity of silicon present between the electrodes is etched by 20 μm backside DRIE to reduce the parasitic capacitance. Now we will discuss in detail the issues involved during the DRIE and the anodic bonding.

3.1.1 Micromachining process by DRIE

The most important issue is the through-wafer DRIE of silicon in which aluminum serves as hard mask. DRIE is an anisotropic etch, which creates deep trenches in the substrate with high aspect ratios. At ESIEE, silicon etching is performed using Alcatel 601E plasma etcher [2]. This equipment is configured with a 2 KW ICP source and the RF or LF generator for wafer polarization. Wafer is clamped with a mechanical chuck and can be maintained at a temperature from – 150 °C to + 20 °C. Two ways can be used to achieve vertical anisotropic deep plasma etching of silicon with this equipment:

1) The cryogenic process [3]: During the DRIE process, a thin layer of silicon dioxide is used for side wall protection, to maintain anisotropy. The process is not used for deep depths etching.
2) The patented Bosch process [4]: The bosch process works in two steps, one is etching cycle and other is passivation cycle. The etching cycle is responsible to etch a small depth in the silicon substrate, whereas the passivation cycle deposits a protective layer on vertical and horizontals sides. This passivation

layer protects the sidewalls of the substrate, whereas due to the highly speedy ion bombardment, oriented in the vertical direction during the etching step, the passivation is removed from horizontal surfaces and small etching is performed again. For etching step we use SF_6 whereas for passivation we use C_4F_8.

For our device we need to etch openings of various dimensions (from 30 µm to few millimeters) trough the wafer (380 µm thick). This is particularly critical because of a common physical effect, observed in deep etching, called as ARDE effect (*Aspect Ratio Dependent Etching*). The ARDE effect is observed when we etch different etch widths at a given etching time. The mask is often modified to minimize this effect by drawing dummy structures thus allowing maintaining a constant opening area. Another way to obtain deep etching, on various pattern width, is to use an etch-stop layer like SiO_2 in the case of SOI wafers or using thick resist in the case of ordinary silicon wafer. The over-etching time is necessary to compensate the loss of etching rate for narrower structures. This over-etching time should be controlled perfectly to avoid Critical Dimension (CD) loss on the narrowest structures. Indeed, charging occurs at the dielectric bottom (etch stop layer) in high aspect ratio patterns, which causes sidewall attacks by re-directed ions (*Notching* phenomenon).

The recipe of DRIE of 400 µm thick substrate consists of three consecutive steps which are:

1) RF biased etching step 1:

- Flow-rate : 300 cc of SF_6 for 5sec
- Flow-rate : 150 cc of C_4F_8 for 2 sec
- Pressure = 4 Pa
- Power of ICP source = 1800 W
- Power of substrate source = 100 W

2) RF biased etching step 2:

- Only SF_6 timing is increased up to 6 sec.

3) LF biased etching step 3:

- Now RF biasing is turned into LF pulsed biasing.

In the first step of RF biased etching, the etching step (by SF_6) and passivation steps (by C_4F_8) continue until the etched thickness is around 200- 250 µm. For larger depths, the polymer deposition (during passivation) can cause problems, as there could be lot of polymer deposition until the point comes when it becomes impossible to remove the polymer. Hence in order to avoid such sort of problem, the etching rate is increased by prolonging the timing of SF_6 with the same concentration. This can help to remove the polymer deposited horizontally on the silicon substrate. In the last step RF is changed to 400 kHz LF biased source, which helps to discharge the etch stop layer [5] and thus avoid notching. 10 µm thick resist is used as an etch stop layer.

Hence the structures were obtained using a mixed RF/ LF pulsed process allowing smooth sidewall, almost perfect anisotropy and no negative effect of the over-etching time. Total etching time is around 1h and 30 min. Fig. 3.2 shows the backside microscopic view of the proof mass after the through-wafer DRIE (oxide is used as the etch stop in this case). Fig. 3.3 shows the 3D view of the combs of Comb Configuration (CC) after DRIE.

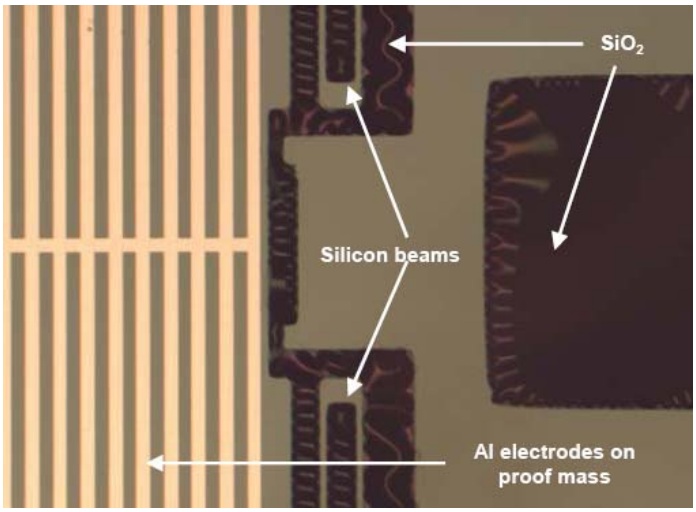

Fig. 3.2 Microscopic backside view of silicon substrate just after DRIE. SiO_2 is used as an etch stop layer

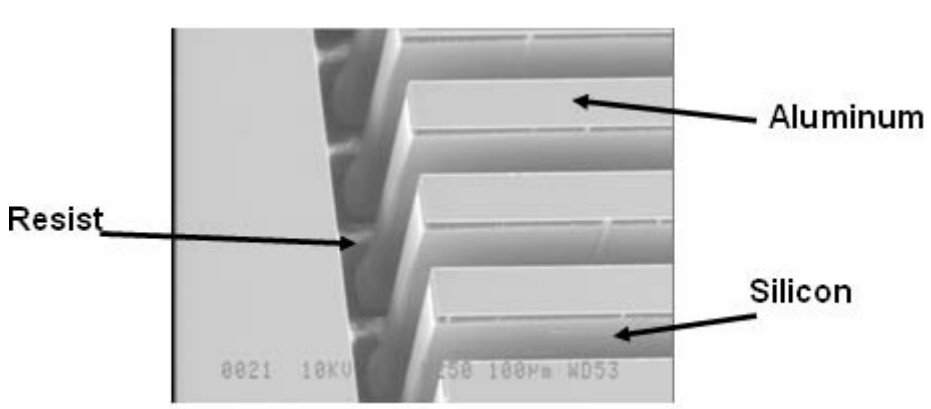

Fig. 3.3 Microscopic topside view of CC just after DRIE. Resist is used as an etch stop layer

3.1.2 Substrate assembling by anodic bonding

The anodic bonding of the silicon and the glass wafer is performed using *Electronic Vision* [tm] 501S. The anodic or electrostatic bonding is defined as the process in which the silicon substrate is adhered to the glass substrate. Two substrates are put into direct contact and heated at around 400-500 °C. The heat mobilizes the sodium ions present in the glass. Then a high voltage ranging between 300 to 500 V is applied. As a result of which, the sodium ion movement is created under the effect of the applied electric field at the interface and hence, an ion-depletion region is being created. This pulls the two wafers together and an anodic bond is created [6]. For our device the applied voltage is equal to 300 V at 420°C.

The main problem in the case of IPOP configuration is that there exists a pair of parallel plate electrodes and with the application of the voltage an electric field is created between these electrodes. The pull-in voltage is around 10 V. In order to avoid pull-in between top and bottom electrodes, an additional care has been taken in the mask design. All the aluminum electrodes and connections present on the glass wafer are filled in a glass cavity which is etched by HF. Some part of the aluminum is kept outside the cavity. The overlap of this metal is made with the top electrodes, which creates a short circuit between top and bottom electrodes, hence making the electric field between them equals to zero. After the

anodic bonding this connection can be rubbed off using micro-manipulators. The mask snapshot and 3D view of this short circuit is shown in Fig. 3.4.

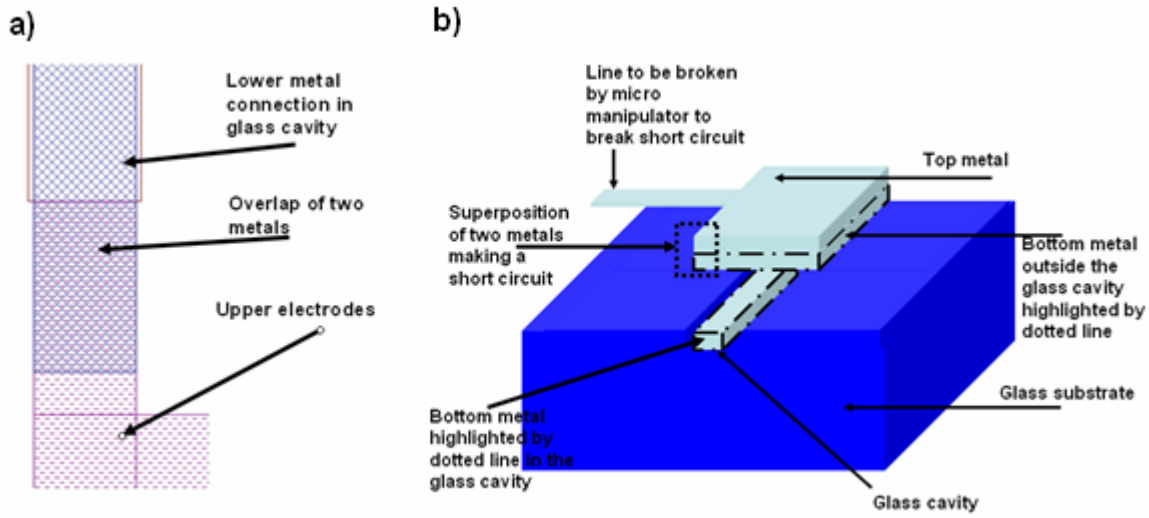

Fig. 3.4 a) Snapshot of mask shows the overlap of top and bottom metals to avoid stiction during bonding, b) 3D view of the overlap of top and bottom metals to avoid stiction during bonding

3.1.3 Fabrication results

Fig. 3.5 shows the overall status of the devices after the processed silicon and glass wafers are processed and bonded. At the end of the whole process, 18 structures out of 26 are released after DRIE. The structures which were not liberated lie at the wafer edge. As the DRIE plasma etches faster at the center than on the edges, thus the process has to be stopped, to avoid the crack in the etch stop layer. If it happens, the plasma can easily pass through the crack and starts baking the resist present at other sides of the wafer. Fig. 3.6 shows the SEM pictures of the CC based vibration-to-electricity converter, with two close-up views.

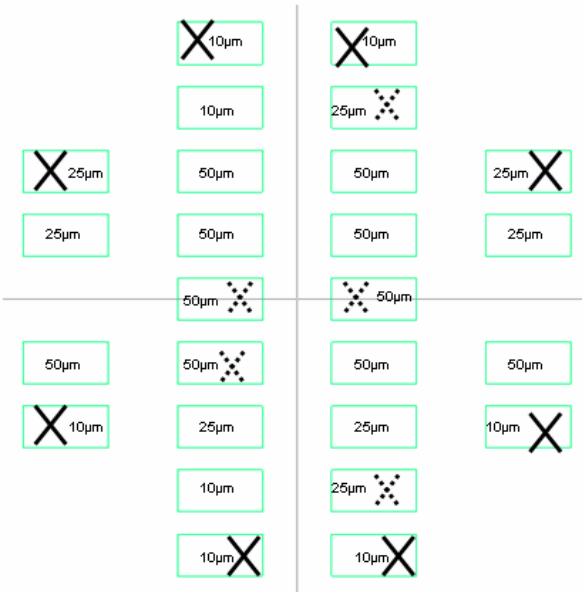

Fig. 3.5 Overall status of the wafer, 18 out of 26 dies are successfully released after DRIE. The structures crossed with dotted crosses are broken during the dicing of the wafer. (10 µm, 25 µm and 50 µm shows the electrodes size)

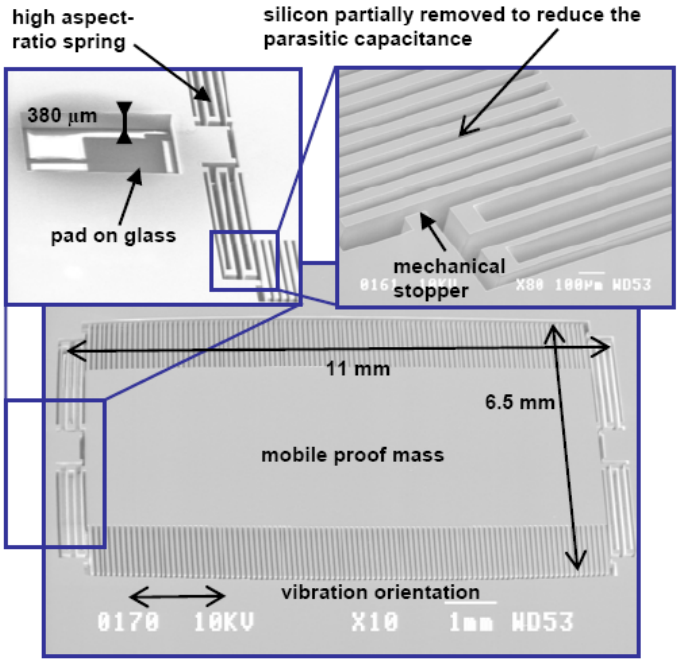

Fig. 3.6 SEM pictures of the CC based vibration-to-electricity converter with two close-up views

3.2 Dynamic characterization of the capacitance variation

In order to perform the measurements, the resonators were mounted on a PCB and wire-bonded to the conditioning electronic circuit (cf. Fig. 3.7). The PCB is fixed on a vibration table, type *P-6201.1* from *Physik Instrumente*[tm]. We applied in-plane mechanical vibrations. A dynamic measurement of C_{var} is achieved by measuring the phase shift in an RC_{var} circuit powered with an AC voltage at a frequency much higher than the frequency of the mechanical vibrations (cf. Fig. 3.8).

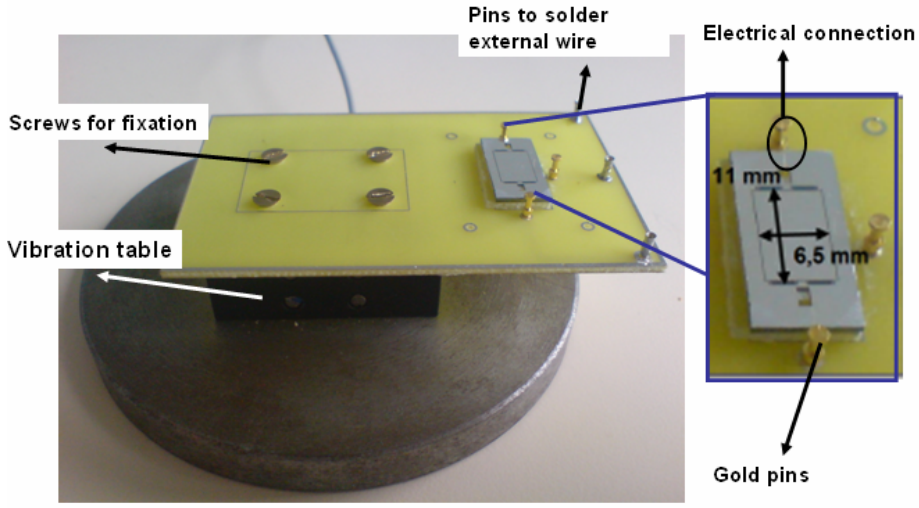

Fig. 3.7 Test bench used in measurements with the zoomed view of energy harvester

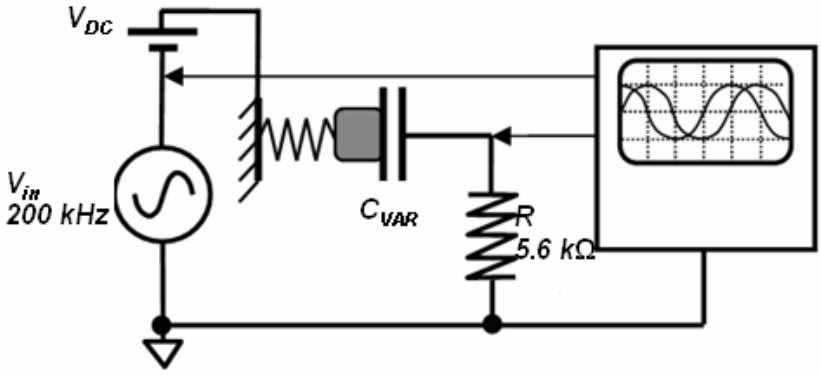

Fig. 3.8 Setup for dynamic measurement of the transducer's capacitance variation

The capacitance is calculated as:

$$C_{\text{var}} = \frac{1}{\tan(\theta) R\omega}, \tag{3.1}$$

where ω is the angular frequency of source signal V_{in}, θ is the phase-shift between the voltage across the capacitor and the voltage generated by the source. The precision of θ measurement is defined by the resolution of the oscilloscope, *i.e.* by the sampling period T_s. As the time error being T_s, the error on θ would be $T_s\,\omega$. Considering that R is known with a negligible error (1% error for regular resistors), we have the following error on C_{var}:

$$\begin{aligned}\Delta C_{\text{var}} = d\left(\frac{1}{\tan(\theta) R\omega}\right) &= -\frac{1}{R\omega}\frac{1}{\sin^2(\theta)} d\theta \\ &= -C_{\text{var}}\frac{1}{\cos(\theta)\sin(\theta)}\frac{d\theta}{dt} dt\end{aligned}, \tag{3.2}$$

where dt is the time error measurement. For finite error, if d$t = T_s$, it gives:

$$\frac{\Delta C_{\text{var}}}{C_{\text{var}}} = -2\frac{T_s\omega}{\sin(2\theta)}, \tag{3.3}$$

To minimize the error, an initial phase shift of $\theta=\pi/4$ should be chosen. This is only possible if the exact value of C_{var} is known *a priori*. Since we know the range of expected values from design, we adjust ω and R in order to maximize the measurement accuracy at the mean value of C_{var} i.e. C_{var_m}. From equation (3.1) the governing ratio is therefore:

$$C_{\text{var}\_m} R\omega = 1, \tag{3.4}$$

which leaves one free parameter among ω and R. But the choice of the frequency is constrained by two factors. First, the frequency ω should be much higher than the frequency of the capacitance variation. This is necessary for the circuit to operate in a quasi-stationary sinusoidal mode only in which the above analysis is valid. In addition, equation (3.3) states that the measurement error on C_{var} is proportional to the frequency ω. On the other hand, the available oscilloscope memory is finite, which limits the maximal acquisition time: a high frequency prohibits long data acquisition time, and thus makes difficult to take observation of

a long-term capacity evolution, due to which compromise is necessary. From equations (3.1) and (3.3), the relative error can be calculated as:

$$\frac{\Delta C_{\text{var}}}{C_{\text{var}}} = -2\frac{T_S\omega}{\sin\left[2\tan^{-1}\left(\frac{1}{\omega R C_{\text{var}}}\right)\right]} \quad , \tag{3.5}$$

Thus, for each measurement, the above formula must be applied *a posteriori* on the maximal and minimal measured values of C_{var} to estimate the worst-case error.

3.2.1 Verification of test bench

In order to verify the test bench, we tested a commercial capacitor of 68 pF, which is given with an error of 1%. At first, its capacitance is measured by means of LCR meter *Agilent^{tm} 4275A*. The value is found to be 69 pF. Then it was measured using the test bench. The oscilloscope used to acquire the two signals is *Le Croy^{tm} 9354AL*. The acquired signals have non negligible (quantization) noise which is generated as we used the digital function generator (*AFG 3102*) to generate V_{in}. During digital to analog conversion, undesired frequency components are generated in addition to the desired signal frequency. These generated harmonics are eliminated by taking the FFT of the acquired signals and fixing the amplitudes of the undesired harmonics zero using *MATLAB^{tm}*. Figs. 3.9 shows the signal V_{in} before and after the *MATLAB^{tm}* treatment.

We also used *MATLAB^{tm}* to calculate the capacitance value at each time instant. Fig. 3.10 shows the capacitance measurement of the used commercial capacitor over 2 msec which is equal to 69.8 pF. The MATLAB-based program which is used to filter-out the noise and measure the capacitance is given in appendix 1. The relative error measured from the equation (3.5) is 0.85%. Here *Ts* is 5 nsec, *R* is 10 kΩ and applied AC frequency is 100 kHz.

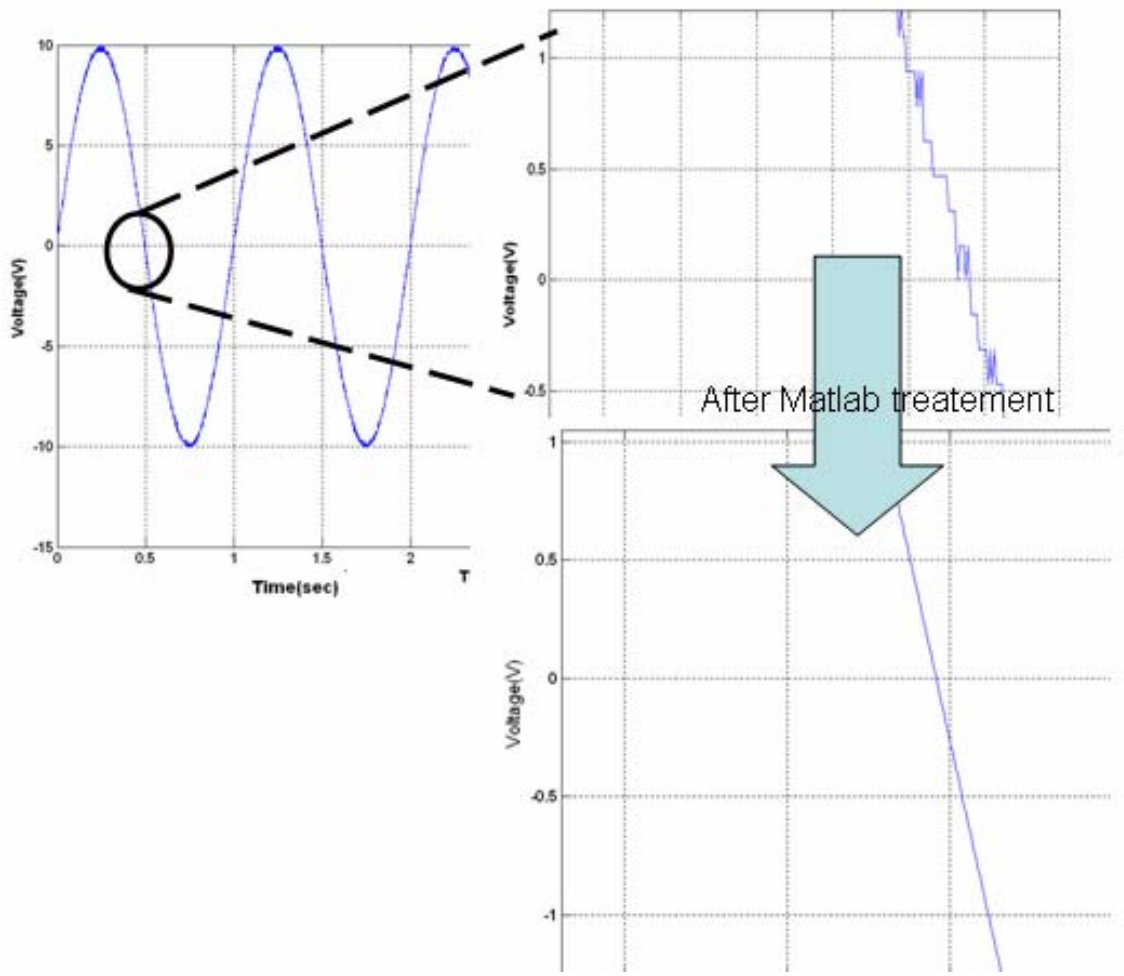

Fig. 3.9 a) Voltage generated by the signal generator before Matlab[tm] treatmen, and after Matlab[tm] treatment.

Along x-axis there is time in seconds whereas along y-axis there is an amplitude of the voltage applied

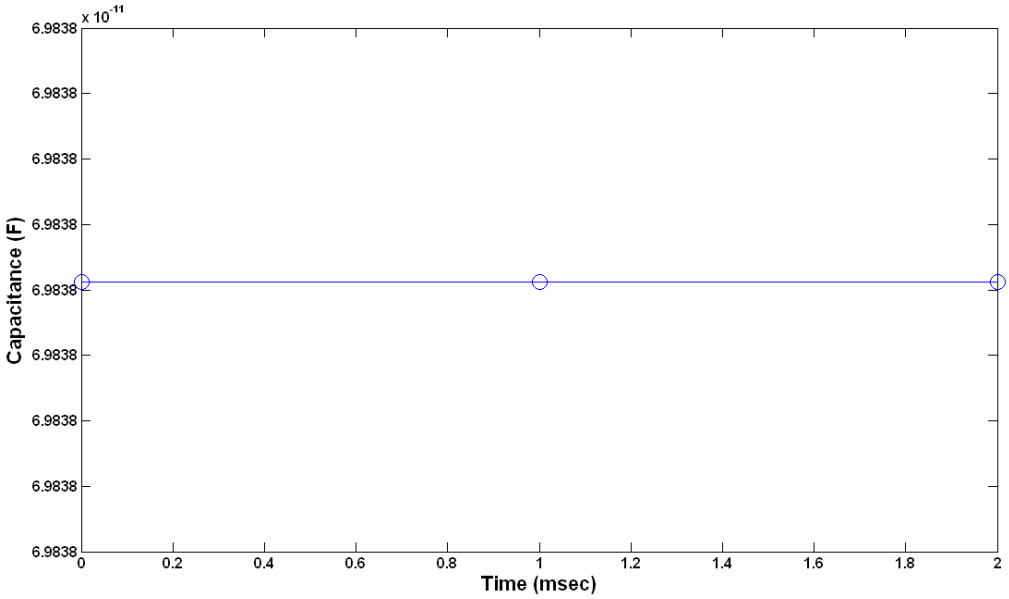

Fig. 3.10 Measurement of the commercial capacitance of value 68 pF using the test bench shown in Fig. 3.8

3.2.2 Dynamic measurement of the transducer's capacitance

The in-plane vibrations are applied at the mechanical resonance of device which is observed optically at 250 Hz, with a minimum acceleration of 0.1 *g* to obtain a proof mass displacement of 50 μm. The frequency of AC voltage is set to 200 kHz. The measurements have been performed with an oscilloscope, *Le Croy*^{tm} *9354AL*, having a sampling time T_s equal to 10 nsec and with a resistance R of 5.6 kΩ. By applying an AC voltage of magnitude 500 mV on C_{var}, it exhibits a maximum variation from 73 to 144 pF as shown in Fig. 3.11. During one mechanical cycle, the proof mass passes twice through the mean position, so the frequency of C_{var} variation is consequently twice the mechanical vibration frequency. Equation (3.5) gives a maximum relative error around 3.1%. The variation of the relative error with the capacitance variation is shown in Fig. 3.12. *Ts* is 1 nsec, R is 5.6 kΩ and applied AC frequency is 200 kHz. The maximum error exists when the capacitance approaches its minimum value as the value of capacitance deviates from the optimum capacitance value as mentioned in equation (3.4).

When a DC voltage V_{dc} is superpimposed on the sinusoidal voltage V_{in} (Fig. 3.8), the vertical electrostatic force between top and bottom electrodes pulls the proof mass down to the substrate and thus reduces the ratio C_{max}/C_{min}, mainly because of an increase in the fringe field which is responsible for C_{min} value. In this scenario the acceleration required to attain the resonance also increases. Thus, at V_{dc} equal to 8 V, the measured ratio C_{max}/C_{min} is 1.3 (cf. Fig. 3.13) and the acceleration required to achieve resonance is 0.25 *g*. This corresponds to a gap reduction of almost 40%, which is much bigger than the theoretical maximum gap reduction threshold of 33% for pull-in instability in the case of an ideal electrostatic actuator. This behaviour is ascribed to a nonlinear spring stiffness, which increases at large displacement of the attached proof-mass [7].

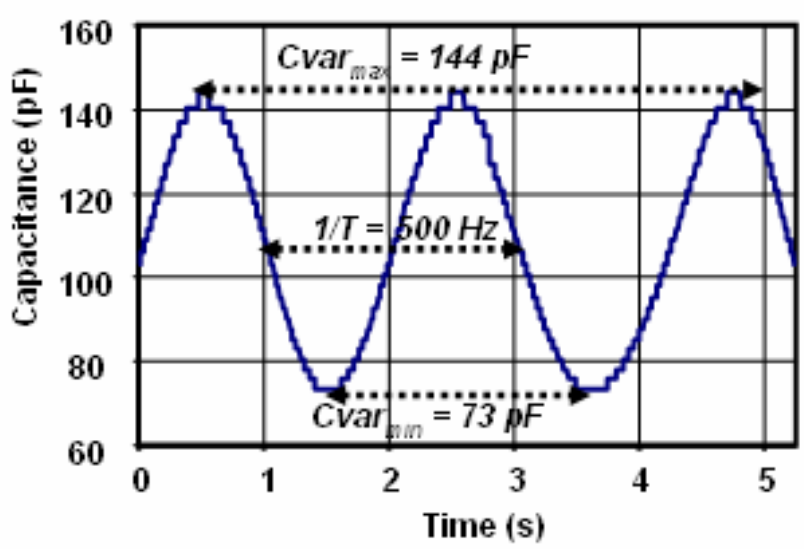

Fig. 3.11 Dynamic measurement of the transducer's capacitance: capacitance variation C_{var} with time with no DC voltage applied

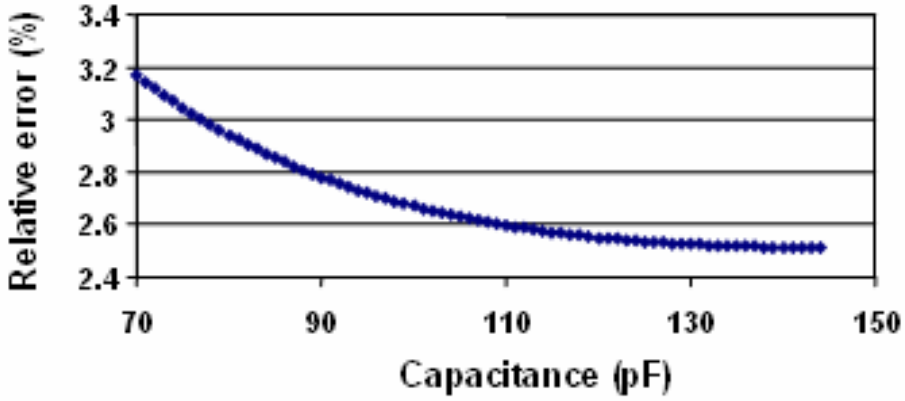

Fig. 3.12 Variation of the relative error with respect to the capacitance

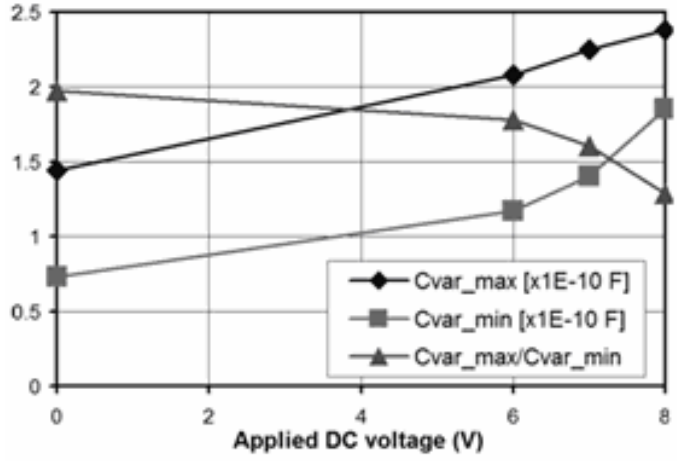

Fig. 3.13 Measurement of $Cvar_{max}$, $Cvar_{min}$ and $Cvar_{max}/Cvar_{min}$ ratio with increasing applied DC voltage

The comparison of measured and simulated values, from chapter 2, shows a large deviation. The expected value of the maximum capacitance is 200 pF and the minimum capacitance is 50 pF, but instead of these values we observed the variation of the capacitance between 144 pF and 73 pF. This is due to the following reasons:

1) As glass wafer is chemically etched with some uncertainty, hence the resulting air gap between the top and the bottom electrodes is 1.69 µm instead of 1.5 µm.
2) In the simulations, the capacitance between the silicon substrate and the electrodes deposited on the silicon were short-circuited as both layers were connected to the ground terminal. But in real measurements the substrate was kept in the floating state. The silicon substrate and top aluminium electrodes have a silicon dioxide dielectric in between them. The capacitance exists between them is estimated to nearly 2 nF (cf. C_{s2} in Fig. 2.17(a)). The incorporation of this value in the net capacitance model decreases the net capacitance value.
3) Due to the backside DRIE, the substrate capacitance is reduced but on the other hand the net value of the fringe capacitance (capacitance between the electrodes deposited on the glass wafer and the edges of top electrodes, shown by C_F in Fig. 2.17(a)) is also modified. The edge thickness of top electrodes is 20 µm (thickness of aluminium and backside DRIE depth) instead of 0.5 µm.

The incorporation of the first two modified parameters (i.e. air gap, and C_{S2}) in the capacitance model explained in section 2.2.2 gives us the capacitance variation between 145 pF and 63 pF. As this is already explained that backside DRIE disturbs the electrode thickness which alters the fringe capacitance. The incorporation of 6 µm electrode thickness (analytically) gives us the capacitance variation between 144 and 73 pF, respectively. This thickness represents the net electrode thickness which affects the fringe capacitance C_F.

3.3 Q - Factor measurement

The next task in the characterization is to measure the mechanical quality factor (Q-factor) of the transducer. This characterization can help us to estimate the mechanical damping and the bandwidth of the resonator. In the case of an electrostatic resonator, when the voltage is applied across the movable and the fixed electrode, an electrostatic force is generated between the two electrodes. The applied voltage is composed of a DC and an AC components, the electrostatic force is given as:

$$F_e = \frac{1}{2}\frac{\partial C}{\partial z}\left(V_{DC} + V_{AC}\sin(\omega t)\right)^2, \tag{3.6}$$

where V_{DC}, V_{AC}, C, z and ω are DC voltage component, AC voltage component, capacitance of the resonator, displacement of the proof mass and the angular frequency of AC signal. For $V_{DC} >> V_{AC}$, one can rewrite equation (3.6) as follows,

$$F_e \cong \frac{1}{2}\frac{\partial C}{\partial z}{V_{DC}}^2 + \frac{\partial C}{\partial z}V_{DC}V_{AC}\sin(\omega t), \tag{3.7}$$

Hence under the condition equation (3.7), the electrostatic force depends on two components, one is constant and the second is harmonic which will induce vibrations on the resonator. Higher harmonics can be neglected, so the electrostatic force has a linear response with applied AC voltage. The output current of the transducer is given as:

$$I_{out} = \frac{dC}{dz}\frac{dz}{dt}V_{DC}, \tag{3.8}$$

The higher the rate of change in displacement of a movable electrode (speed) , the higher will be the output current of the transducer.

The electrical representation of the resonator is given in Fig. 3.14. Hence the resonator is composed of mass, spring, damper, represented by RLC series circuit, and a parasitic capacitance in parallel which is responsible for the electrical coupling of input and output ports.

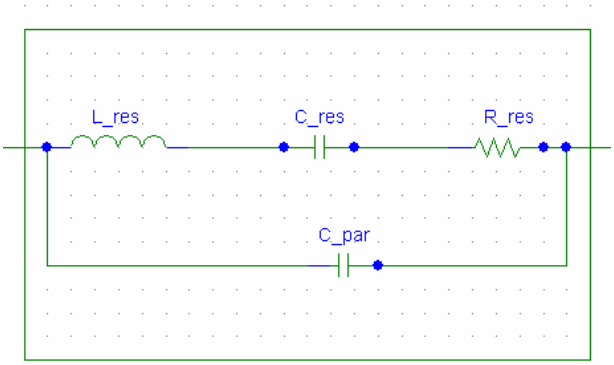

Fig. 3.14 Electrical representation of the resonator

This equivalence can be represented mathematically [8]:

$$R\_res = \frac{\sqrt{km}}{Q\sigma^2}, \tag{3.9}$$

$$C\_res = \frac{\sigma^2}{k}, \tag{3.10}$$

$$L\_res = \frac{m}{\sigma^2}, \tag{3.11}$$

$$\sigma = V_{DC}\frac{dC}{dz}, \tag{3.12}$$

where k, m, Q, and σ are spring constant, mass, Q-factor and electromechanical transduction factor of the resonator, respectively. In order to characterize the resonator, the effect of parasitic capacitance must be eliminated. The method we followed consists of three steps [9]:

1) Characterize the overall response (resonator + parasitic capacitance) by applying the DC + AC voltage. Applied DC voltage must be higher than the AC voltage to have a linear response of the resonator.
2) As it is shown in equation (3.12) that the transduction factor is proportional to the DC voltage so we should switch off the DC voltage and once this factor is zero, the net response obtained is the response of the parasitic capacitance.
3) Subtract second response from the first to have the response of pure electro-mechanical resonator without the parasitic capacitance. From that response the

resonance frequency and bandwidth can be measured by which we will be able to calculate the Q-factor.

The schematic of the setup used to measure the Q-factor is shown in the Fig. 3.15. AC signal is applied and the response is seen by using the network analyzer *89410A* from *Agilent*^{tm}. The frequency is swept around the expected value of the resonance frequency. Fig. 3.16 shows the response of the resonator and the parasitic capacitance at V_{AC} = 800 mV and V_{DC} = 2.5 V, along with the response of the parasitic capacitance with no DC polarization. Fig. 3.17 shows the results after the subtraction. The bandwidth at -3 dB is 1.7 Hz and the resonance frequency is 250.5 Hz. From these values, the Q-factor of 147 is estimated. By the measurement of resonance frequency, Q-factor and mass of the resonator, the calculated fluid damping is 5.02 10^{-4} Ns/m (using eq. 2.18 of chapter 2).

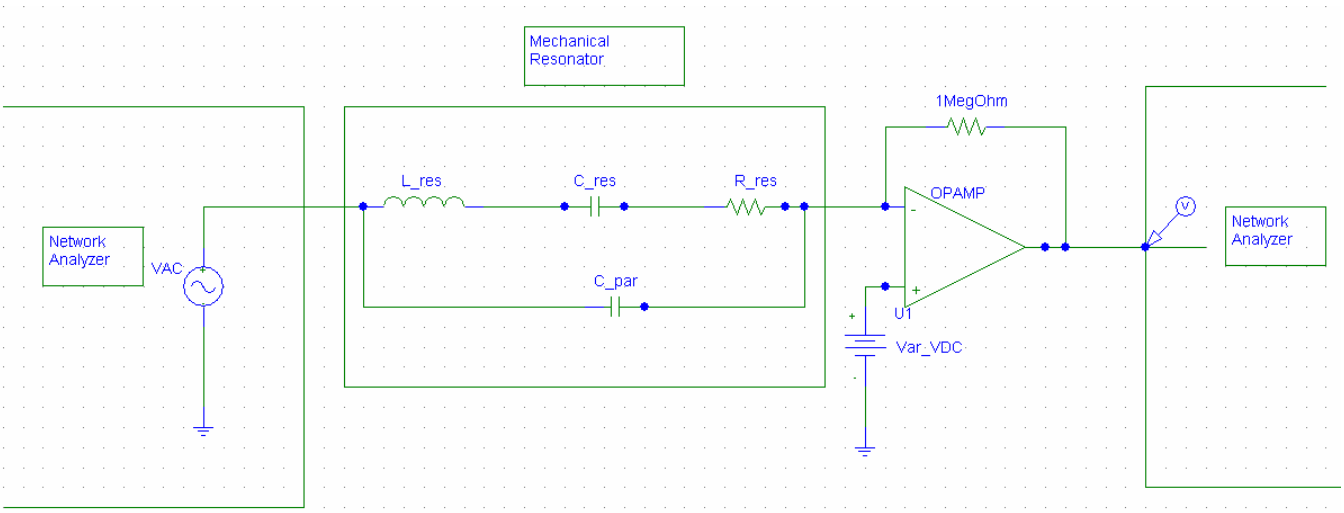

Fig. 3.15 The setup to measure the Q-factor

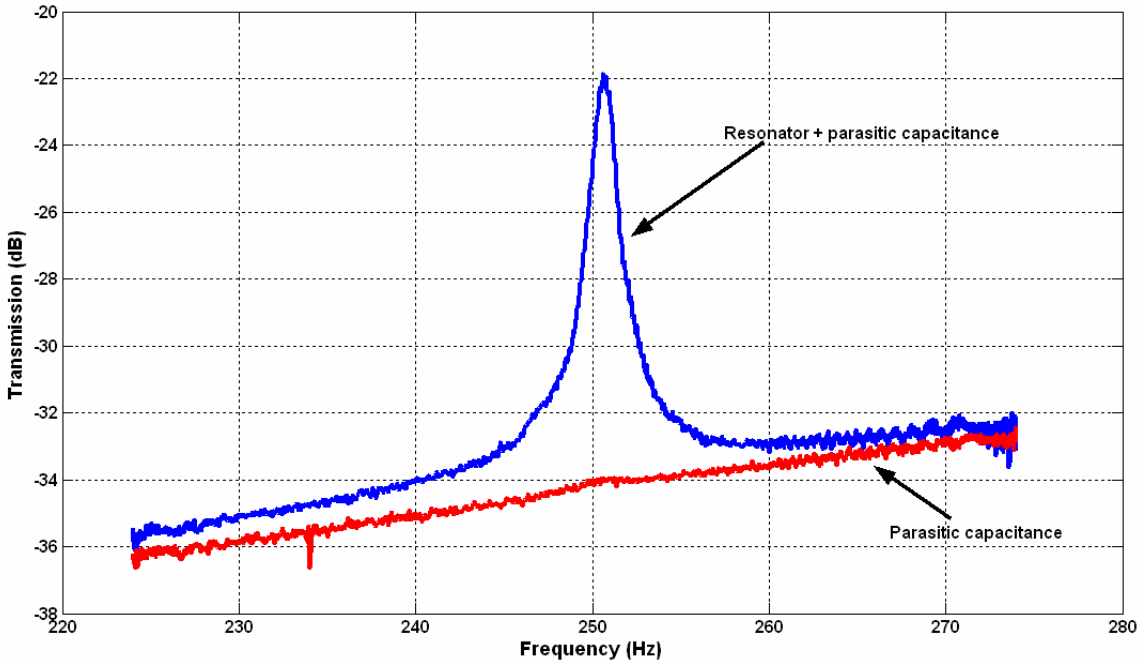

Fig. 3.16 Response of the resonator + parasitic capacitance and

Response of the parasitic capacitance only(with no DC polarization)

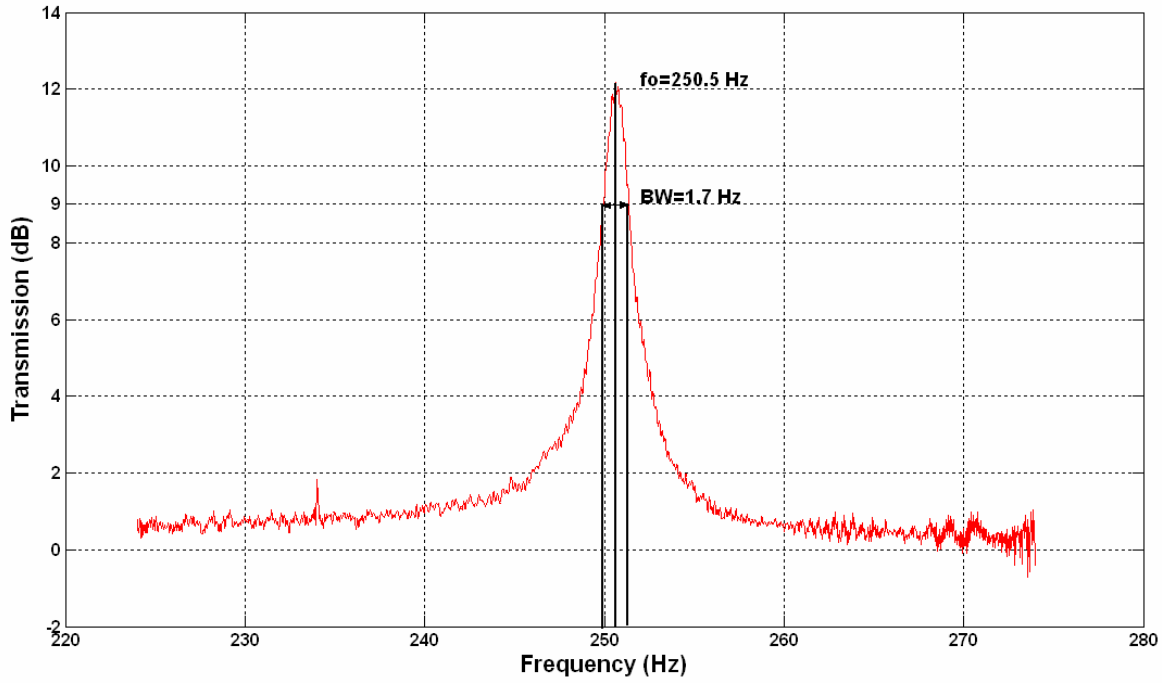

Fig. 3.17 Response of the resonator

3.4 Measurement of converted power using a charge pump circuit

The mechanism of the conditioning electronics described in [10] consists of two phases: energy accumulation (charge pump) and recharge of a reservoir capacitor C_{Res} through an inductive flyback. In this research, the energy harvester is only implemented in a charge pump to study the continuous power conversion from the mechanical to the electrical domain.

3.4.1 Description of the method

The measurement setup scheme is shown in Fig. 3.18. The charge pump is composed of three capacitors: a large capacitance C_{res} = 1.3 µF, a smaller C_{store} = 3.3 nF and C_{var} which is the variable transducer capacitance and varies typically in a range of hundreds of pico-farads. The role of the charge pump is to transfer the charges from C_{res} toward C_{store}. Since $C_{store} << C_{res}$, this transfer requires an external energy which is provided by the mechanical vibrations through the variations of the capacitance C_{var}. Without the load resistor, C_{store} voltage increases and C_{res} voltage decreases gradually until the charge pump reaches a saturation regime at which no power is generated (as there is constant energy with time). To observe a continuous energy conversion, a load resistor is connected to C_{store}, hence the charge pump is kept away from the saturation.

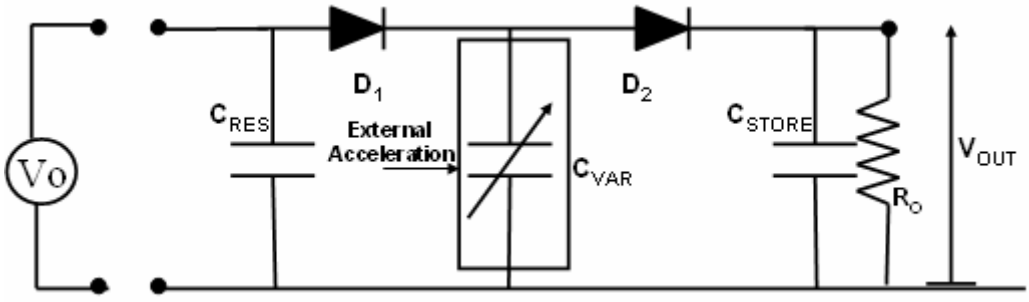

Fig. 3.18 The charge pump circuit

The measurements are achieved in the following way. First, C_{res} is pre-charged with a DC voltage at V_o. Then the voltage source is disconnected from the system which makes the

charge pump electrically autonomous. C_{res} and C_{store} discharge and inject energy into the circuit, conversely diodes and R_{load} dissipate the energy. In a purely electrical circuit we have:

$$E_{R_{load}} + E_{diodes} = E_{C_{res}} + E_{C_{store}} \,, \tag{3.13}$$

However, since the transducer converts mechanical energy into electrical energy, the measured dissipated energy is expected to be higher than the energy provided by the capacitors. Thus, the energy balancing equation for the given system is:

$$E_{mec} = E_{Rload} + E_{diodes} - E_{Cres} - E_{Cstore} \,, \tag{3.14}$$

where E_{mec}, E_{Rload}, E_{diodes}, E_{Cres} and E_{Cstore} are the energy harvested by the mechanical vibrations, energy dissipated by the load resistance, energy dissipated in the diodes, energy stored in C_{res} and C_{store}, respectively. Between time instants t_1 and t_2, these energies can be defined as:

$$E_{R_{load}} = \frac{1}{R_{load}} \int_{t_1}^{t_2} \frac{(V_{store}(t))^2}{2} dt \,, \tag{3.15}$$

$$E_{diodes} = \Delta Q_{res} V_d + \Delta Q_{store} V_d \,, \tag{3.16}$$

$$E_{C_{res}} = \frac{C_{res}}{2} \left({V_{res\_0}}^2 - {V_{res-n}}^2 \right), \tag{3.17}$$

$$E_{C_{store}} = \frac{C_{store}}{2} \left({V_{store-0}}^2 - {V_{store-n}}^2 \right) \tag{3.18}$$

where

$$\Delta Q_{res} = C_{res} \Delta V_{res} \text{ and } \Delta Q_{store} = C_{res} \Delta V_{store}$$

V_d, ΔV_{res}, ΔV_{store}, $V_{res\text{-}o}$, $V_{res\text{-}n}$, $V_{store\text{-}o}$ and $V_{store\text{-}n}$ are the threshold voltage of the diode, change in the voltage across C_{res} and C_{store}, the voltages across C_{res} and C_{store} at the initial and final time, respectively. We assumed above that V_d is constant, which is not exactly the case. For our calculations we take V_d = 0.4 V and 0.6 V. The first value is consistent with the indirect measurement and confirmed by the simulation. It corresponds to the typical average current circulating in our system, which transfer the essential amount of charges. The value of 0.6 V

gives an upper limit of the harvested power. The power generated by the mechanical vibrations in certain time frame Δt is then given as:

$$P_{mec} = \frac{E_{mec}}{\Delta t}, \tag{3.19}$$

Δt can be any time interval taken to see the evolution of the energy. Greater the value of Δt, lower would be the energy generation we are going to measure because of the discharge of C_{res}.

The diodes should have low reverse leakage current to minimize the discharge of the initial charge stored in the harvester. The condition for the diodes is already mentioned in chapter 2 i.e.:

$$Q_{initial} = C_{\max} V_0 >> Q_{leakage} = I_{reverse} T_{period},$$

where $Q_{initial}$, C_{max}, V_0, $I_{reverse}$, $Q_{leakage}$ and T_{period} are the initial charge stored in the transducer, the maximum capacitance of the transducer, the initial applied voltage, the reverse leakage current, the charge loss due to it , and the electrical time period of the cycle respectively. In our case the system can be pre-charged with a maximum of 6 V (as we are limited by the pull-in voltage), hence $Q_{initial} = C_{max} V_o$ = 858 pC (as calculated with C_{max} of the used transducer i.e. 143 pF). The selected diode is a JPAD5 from *Calogic corporation*^{tm} with the leakage current of 5 pA. Hence with the electrical frequency at 500 Hz, $Q_{leakage}$ is 10 fC, so the charge lost due to the leakage current is negligible. Attention should be paid towards the voltage measurement as well. The available voltage probes, *TEK*^{TM} *6139A,* having 10 MΩ resistance, could not be directly used for the voltage measurement, since the electrical charge stored in the capacitors would leak through this resistance. To avoid this, an Op-Amp based voltage follower configuration is used. The operational amplifier selected for this purpose is AD549J from *Analog Devices*^{tm}, having high input impedance and low input bias current 250 fA.

3.4.2 Measurement

The charge pump is tested with and without the load resistance.

3.4.2.1 Without the load resistance

Initially the charge pump is tested without the load resistance. C_{res} is charged with a DC voltage of 6 V. Due to the vibrations, the voltage across C_{store} increases and gets saturated after some time as shown in Fig. 3.20. From theory, the saturation voltage is given as [8]:

$$V_{store\_sat} = \frac{C_{\max}}{C_{\min}}(V_o - V_d) - V_d , \tag{3.20}$$

With the ratio C_{max}/C_{min} for the tested transducer being equal to 1.9, the above equation yields the theoretical value of V_{store} at saturation around 11 V with V_d = 0.1 V. But as we have seen that with the application of DC voltage C_{max}/C_{min} reduces (cf. Fig. 3.13). Hence the measurement without the load identifies the saturation voltage V_{store_sat} of the charge pump to be 8.45 V for C_{max}/C_{min} =1.45 and V_d= 0.1 V (cf. Fig. 3.19). Such a low diode voltage is explained by the fact that there is nearly no charge transfer when the charge pump is saturated.

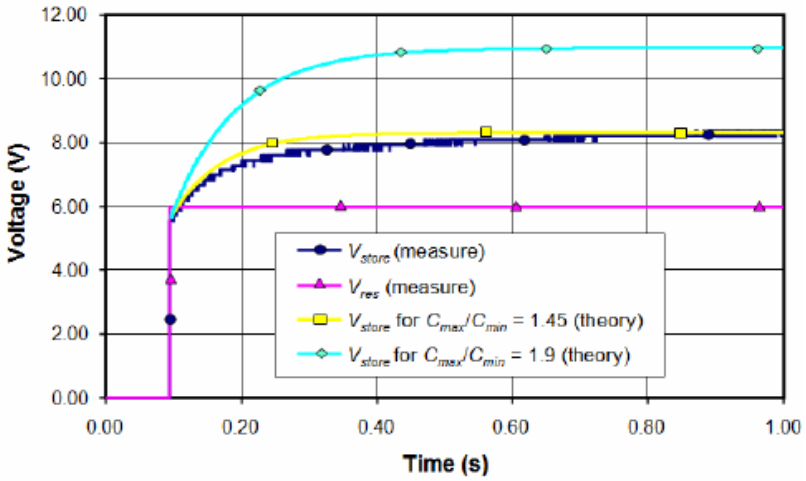

Fig. 3.19 Measurement and theoretical evolution with time of V_{res} and V_{store} with an infinite load after an initial pre-charge of V_0 = 6 V on V_{res}

3.4.2.2 With the load resistance

To evaluate the part of the power which is harvested from the mechanical domain, we performed experiments with various non-zero loads from 30 to 150 MΩ. A typical example of the obtained curves is given in Fig. 3.20 for R_{load}=50 MΩ. As expected, the voltages evolve exponentially while discharging on R_{load}. Using these curves and energy balancing equation defined from equations 3.13 to 3.19, the net power generated by the mechanical domain is calculated keeping Δt = 20 sec. $V_{res} - V_{store}$ being lower than 2 diodes threshold voltages, there is a positive electrical energy generation coming necessarily from the mechanical domain. This experiment was modelled using a mixed VHDL-AMS model presented in [11], implemented with the same C_{max}/C_{min} ratio of 1.45 and with a realistic exponential diode model. This model is simulated in *AdvanceMS* environment with the help of Dr. D. Galayko of LIP-6 Paris. For the capacitor voltage evolution, the modelling and the experiment agreed better than 3%.

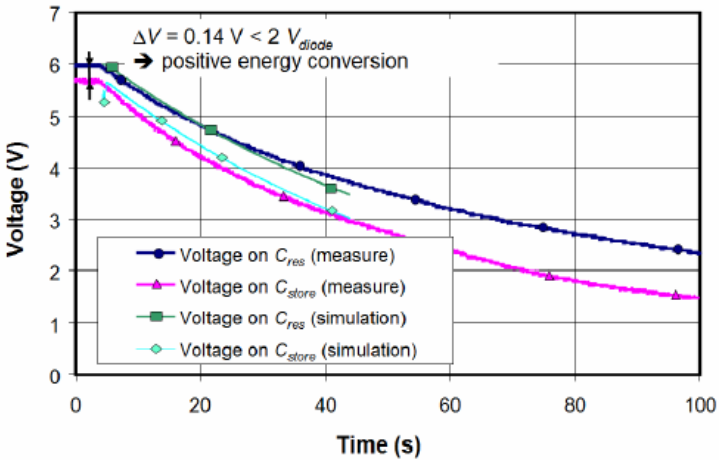

Fig. 3.20 Measurements and simulations of the charge-pump operation in autonomous mode on a 50 MΩ load resistance for a pre-charge of 6 V

The plot in Fig. 3.21 shows the value of P_{mec} calculated from the measured and from the simulated voltage evolutions. When the power dissipated in the diodes is assumed constant, we obtain a maximal electrical power generation of 61 (103) nW on a 60 (50) MΩ load

resistor for V_d 0.4 (0.6) V, respectively. The power extracted from the modeling highlights a maximal power of 79 nW for an optimal load of 90 MΩ. Though very acceptable, this discrepancy in the results is due to the difficulty to account correctly for the diode losses in the calculation of the experimental power. For the simulations, ELDO model used a more realistic exponential diode representation. However, it is very difficult to determine the exact value of V_d as it is problematic to measure the transducer voltage because of its low capacitance.

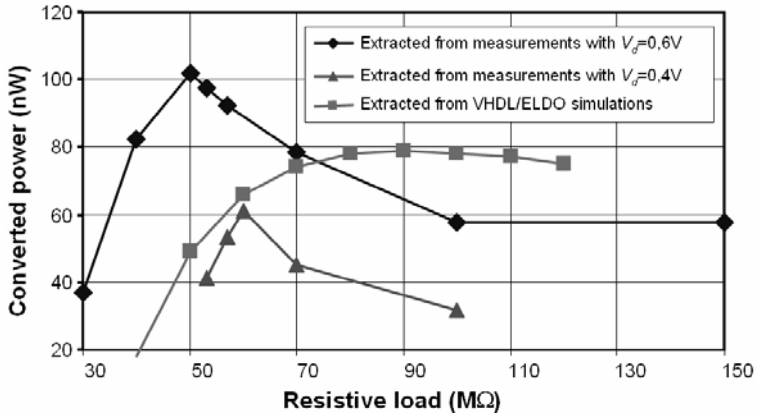

Fig. 3.21 Harvested power converted from the mechanical to the electrical domain in the charge-pump

The power balance is shown in Fig. 3.22. It shows the power calculation for V_d = 0.4 (0.6) V on a 60 (50) MΩ load resistances, respectively.

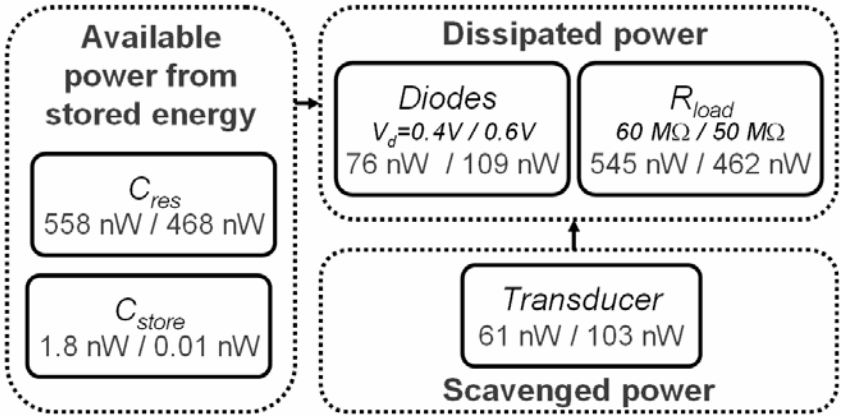

Fig. 3.22 Power balance diagram

3.5 Conclusions

In this chapter, the fabrication process of a micro-machined CMOS-compatible energy harvester is discussed. The fabrication challenges encountered during DRIE process and anodic bonding have been discussed together with proposed solutions. The fabricated, electrostatic-based energy harvester has been characterized. The measurements include the mechanical resonance frequency, acceleration to achieve the resonance, dynamic measurement of the capacitance variation, Q-factor estimation and the energy generation by implementing the transducer in the charge pump circuit. After a pre-charge of the transducer at 6 V, the measurements have been performed in an autonomous mode (no voltage source was connected to the system). We achieved a power conversion in between 61 nW (pessimistic estimation) and 100 nW from the mechanical to the electrical domains with external vibrations at 250 Hz and an amplitude of 0.25 *g*. The results of the charge pump are also compared with the VHDL-AMS / ELDO model simulated in *AdvanceMS* environment with the help of Dr. D. Galayko of LIP-6 Paris. For the capacitor voltage evolution, the modelling and the experiment agreed better than 3%. However, the functioning of energy harvester is limited due to the Pull-in voltage which is 10 V in our case. Thus by increasing the pre-charge voltage from 6 V to 7 V, stiction between the top and the bottom electrodes occurs.

Reference:

[1] C. M. Tassetti *et al.*, "New tunable RF MEMS Microinductor design", *Journal of Micromechanics and Microengineering*, vol. 14, no. 9, pp. 17-22, 2004.

[2] F. Marty, *et al.*, "Advanced etching based on deep reactive ion etching for silicon high aspect ratio microstructures and three dimensional micro and nano structures", *Microelectronics journal*, vol. 36, 2005, *pp. 673-677*

[3] M. J. de Boer, *et al.*, "Guidelines for etching silicon MEMS structures using fluorine high density plasmas at cryogenic temperatures", *Journal of microelectro mechanical systems,* vol. 11, no. 4, August 2002, *pp. 385-401*

[4] Franz Lärmer and Andrea Schilp, Patents DE4241045, US 5501893 and EP 625285

[5] Hopkins, *et al.*, "Method and apparatus for etching a substrate", *US Patent 6187685, (2001)*.

[6] B. Stark, *et al.,* "Chapter 5: MEMS Device Processing", downloadable from site: http://parts.jpl.nasa.gov/docs/JPL%20PUB%2099-1E.pdf, site visited 24th August 2009

[7] C. Cortopassi et al, "Nonlinear Springs for Increasing the Maximum Stable Deflection of MEMS Electrostatic Gap Closing Actuators," downloaded Jul. 10, 2006 from robotics.eece.berkeley.edu/˜pister/245/project/CortopassiEnglander.pdf.

[8] Ville Kaajakari, *et al.*, "Square-extensional mode single crystal silicon micromechanical resonator for low phase noise oscillator applications", IEEE electron device letters, Vol.25, No. 4, pp. 173-175, April-2004

[9] D. Galayko, "Filtres micro électromécaniques micro usinés en poly silicium couche épaisse et leur application au filtrage en fréquence intermédiaire" thèse soutenue à l'université de Lille 1, le 6 Décembre 2002

[10] B. C. Yen, H. L. Jeffery, "A variable capacitance vibration-to-electric energy harvester", *IEEE transactions on circuits and systems*, vol. 53, no. 2, Feb. 2006, *pp. 288-295*

[11] D. Galayko, *et al.*, "AMS modeling of controlled switch for design optimization of capacitive vibration energy harvester", *Proc. of IEEE Int. Behavioral Modeling and Simulation Conf. (BMAS'07),* pp. 115-120, 2007

Chapter 4
Conclusions and Perspectives

This chapter gives an overall conclusion of the conducted research work along with the suggested improvements. The chapter is distributed in three main sections. The first section compares the fabricated energy harvester with other existing electrostatic-based energy harvesters on the basis of figure of merits, which exists in the literature. In order to compare the performance of electrostatic-based vibration-powered energy harvesters, we have also proposed a new figure of merit. It takes into account all the parameters related specifically to the electrostatic transduction. The second section is the summary of the conducted research work along with the achieved successes. The comparison of the measured power has also been made with the theoretical power in the ideal case. In order to improve the power generated by the energy harvester and to implement an autonomous global system, some suggestions have been presented in the third section. These perspectives are classified in two parts. In the first part, the improvement in the design of the transducer has been discussed. The second part addresses the issues related to the global system (transducer with the associated electronics).

4.1 Comparison with existing harvesters

The comparison among different energy harvesters is not so easy. This is because:

1) Each transducer is designed to vibrate at some particular frequency, which depends on the targeted application.
2) They can have different surface areas or volumes.

3) The external acceleration used to vibrate the proof mass can be different,
4) The initial voltage (in case of electrostatic based energy harvester) can be different. As it depends on the design of the energy harvester and the operation of the energy harvester i.e. either the used method is the charge constant or the voltage constant.
5) The materials used to fabricate the transducer can also be different. Heavier material can make harvester vibrates at low frequency but they can be non compatible with the CMOS process.

In our case we report the converted power of 61 nW for 66 mm² surface area. The converted power of our device is lower than the figures which can be found in the literature. However, an adequate comparison with the existing works implies at least all the considerations explained above. For example, the power of 1.8 μW delivered to load reported by Yen [1] was obtained with a transducer capacitor built with large square aluminum and steel sheets of 6.6 cm side and at the rather high frequency of 1.5 kHz, which do not fit with most vibrational environments. Our structure is 30 times smaller in area, and operates at frequency 7 times lower (which is more realistic for the practical applications). So, to make an adequate comparison of different works, some figures of merits (FOMs) were proposed. Those are discussed here below:

4.1.1 Harvester effectiveness

The harvester effectiveness (E_H) has been defined as [2, 3]:

$$E_H = \frac{P_{conv}}{\frac{1}{2} x_l y_{ext} \omega^3 m}, \tag{4.1}$$

The term in the denominator is the maximal power generation with no mechanical damping, as derived in section 1.2.3 (equation. (1.11)). Theoretically the maximum value of E_H is 100%. It is a measure of how closely a specific design approaches its ideal performance.

4.1.2 Volume figure of merit

The harvester effectiveness does not distinguish between the designs of different proof mass density or geometry, as one geometry can be more effective than others. So another figure of merit called as volume figure of merit FoM_v was defined by the same team [3]. It compares the overall performance of a device as a function of its overall size. This is done by replacing mass of the device (m) and distance traveled by the proof mass (x_l) of the devices with equivalent values for an equivalent device of cubic geometry. Hence the replacement has same total package volume, with a proof mass (with the density of gold (ρ_{Au})) occupying half of this volume and other half is the space for displacement. We have:

$$FoM_V = \frac{P_{conv}}{\frac{1}{16} y_{ext} \rho_{Au} Vol^{\frac{4}{3}} \omega^3}, \tag{4.2}$$

4.1.3 Normalized power density

In ref. [4], another figure of merit termed as Normalized Power Density (NPD) is defined. It is given as the stated power output of the device normalized to square of the acceleration level (as the output power varies with the square of acceleration) and divided by total volume of the device. Hence the NPD is given as:

$$NPD = \frac{P_{conv}}{{a_{ext}}^2 Vol}, \tag{4.3}$$

The authors have neglected the frequency factor, according to them the frequency of the resonant generator is fixed whereas the acceleration level is different.

4.1.4 Figure of merit for electrostatic harvesters

The above defined figure of merits are generalized for all vibration-powered micro generators i.e. independent of transduction type. But the problem lies that there are some factors which are significant for each type of transduction. For electrostatic generator we need the initial voltage for harvesting the electrical energy. The energy depends on square of the voltage applied. So in the specific case of electrostatic based energy harvester, the converted power must be normalized with this factor. The secondly important parameter is the targeted vibration frequency which affects the surface area or volume of the device. The resonant generators normally have high Q-factor, hence even small excitation acceleration can make them in resonance, so frequency is more significant than acceleration. Hence the converted power should be normalized with the frequency rather than acceleration. The surface area is also an important parameter to normalize the converted power, which depends on the targeted resonance frequency. The electrodes of the variable capacitor should be optimized in small surface area to generate high power. Hence new figure of merit is given as:

$$FOM = \frac{P_{conv}}{V^2 fA}, \tag{4.4}$$

The following table 4.1 represents the dimensions and parameters of a few electrostatic based energy harvesters and all the above defined figure of merits are calculated for each harvester. In some cases, calculations are not applicable due to incomplete information. From table 4.1, it can be seen that our work has among the best values of the figure of merit.

Table. 4.1 Comparison of electrostatic energy harvesters

Author [ref]	*f (Hz)*	*A (mm^2)*	*Vol (mm^3)*	*y_{ext} (μm)*	*x_l (μm)*	*V (V)*	*P_{conv} (μW)*	*E_H (%)*	*FoM_v (%)*	*NPD ($kgsm^{-3}$)*	*FOM ($10^8 \mu W/(mm^2 Hz V^2)$)*
Miyazaki [5]	45	m*=5gm	-	1	30	5	0.21	12.4	-	-	-
Despesse [6]	50	1800	18000	116	90	120	1050	7.66	0.06	7.55	81
B. Yen [1]	1560	4356	-	-	-	6	9.47[1]	-	-	-	3.87
Tsutsumino [7]	20	200	-	600	-	950 E*	37.7	-	-	-	1.04
Ma [8]	4100	25.9	-	2.2	-	15 E*	0.065	-	-	-	0.27
Suzuki [9]	37	900	990	1000	-	450 E*	0.28	-	1.2×10^{-4}	5.23×10^{-3}	0.0034
This work	250	66	59.4	1	50	8	0.061	1.34	3.2×10^{-3}	0.41	5.68

m = the mass of the system*

E = Electret*

4.2 Overall conclusion

A vibration-powered electrostatic-based energy harvester has been proposed in this research. Issues related to the design, fabrication and characterization of the micro generator have been highligted in the previous chapters. In this subsection, we summarize the criteria of selection of chosen technologies and topologies. The notable choices are given as follows:

1) Vibration is preferred over solar energy due to its high availability in different applications like automotives, aeronautical, domestic utility machines etc… as well as dark environments, and most importantly its around the clock availability unlike solar energy which is available only in day time.

2) Because of the CMOS compatibility feature, electrostatic-based transduction is selected over piezoelectric and electromagnetic.
3) Amongst different topologies, IPOP topology is selected due to the possibility of higher power generation, stability against out-of-axis vibration, fabrication ease and low fluid damping features. Apart from these advantages, the major drawback with IPOP topology is the low pull-in voltage, which limits the output power.
4) The fabrication process is based on silicon-glass technology. The fabrication involves parallel processing of electrodes deposition on a silicon wafer and on a glass wafer, after which both of them are anodically bonded. In this process ordinary, cheap, (100)-oriented, 380 μm-thick, 4" silicon together with 500 μm-thick glass wafers are used. The fabrication process is totally compatible with CMOS process.
5) After all this we tested our CMOS-compatible, IPOP based vibration-powered energy harvester. We have shown experimentally the ability to scavenge mechanical vibrations energy in order to provide electrical power to a resistive load with the use of an electrostatic silicon-based MEMS transducer fabricated in a CMOS-compatible technology. *The result of this work is the first fully working electrostatic energy harvester fabricated in a silicon batch process without using an electret.* After a pre-charge of the transducer at 6 V, the measurements have been performed in autonomous mode (no voltage source was connected to the system). The converted power is 61 nW with external vibrations at 250 Hz and an acceleration amplitude of 0.25 *g*.

The maximal available mechanical power calculated with equation (1.11) is 4.5 µW. This difference of magnitude lies, as this relation takes into account only the spring-mass system, and considers an "ideal" transducer without accounting for the transduction mechanism while neglecting the power losses in mechanical damper and associated electronics. The maximum available power for the electrostatic-based power generators is given in equation (1.13). Using the measured values of the maximum and the minimum capacitance, the resonance frequency and 6 V initial voltage in eq. (1.13) gives us 1.26 µW. This difference arises as the used equation is only valid for a specific case where the associated electronics has no losses and secondly the transducer fully charge and discharge during one cycle unlikely the charge pump case (cf. section 2.1.1.3 *QV-diagram of charge pump operation*).

As compared to other harvesters, our harvester highlights a good FOM after reference [6], but still 61 nW of power is not enough to supply a real microsystem. In order to have a useful generator, a minimum of several µW are mandatory with current technology used in abandoned sensors.

4.3 Future work

The future work can be classified in two main sections. The first section is about the implementation of the global autonomous system. The second section is to improve the design of the harvester to improve the generated power.

4.3.1 To implement the global system

In the contest of this thesis we have implemented our mechanical transducer and verified the power converted from the mechanical to electrical domain using the charge pump

circuit. But in order to implement the real energy harvester for some application, we need to have complete system as shown in Fig. 4.1

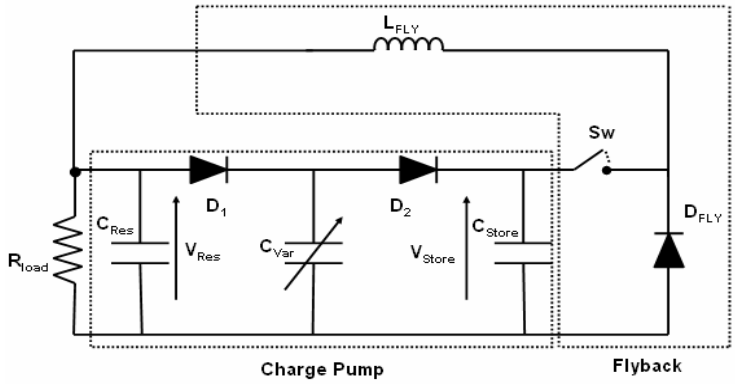

Fig. 4.1 Energy harvesting system [1]

The bottleneck in implementing the global system is the switch. There are two requirements about the switch, i.e. 1) the switch should be "smart' and 2) it should have low consumption losses. If the switch is controlled externally, the system cannot be autonomous. Hence the switch should be smart enough to observe the voltage across C_{Store} and get 'ON' and 'OFF' at the optimal voltage levels. These voltage levels correspond to the operating zone of charge pump where the maximum power is generated (cf. section 2.1.1.3). The switch should not have more consumption losses. In [1] the switch is implemented using MOSFET but it is controlled externally. The power lost in driving the MOSFET is estimated to 50 nW and power losses during the conduction is calculated as 0.36 nW. But the generated power is 1.8 µW. Hence the switch losses are negligible. With an objective to implement the smart switch for the system, a research work is now ongoing [10].

4.3.2 Improvements in the design of the transducer

Here we will discuss the improvements in the mechanical design of the energy harvester in order to improve the generated power and efficiency of the transducer.

4.3.2.1 Improvement of pull-in voltage and capacitance variation

For our device, the output power is mainly limited by its ability to support a high operation voltage, since in electrostatic transducers, the harvested power is proportional to the square of the voltage across the variable capacitance. With the presented technology, much more electrical power is available when the device is designed for higher vibration frequencies *i.e.* with stiffer spring's beams width W. This is due not only to the increased number of capacitance variation cycles, but also because of the increase of the in-plane resonance frequency which leads to a higher out-of-plane instability (pull-in) voltage, and consequently to a higher operation voltage. For instance, the harvested power in such electrostatic transducers scales with $W^{2.5}$. Then doubling W leads to a potential 6-time increase of the harvested power. For our device, P_{mec} would be above 2 μW at 1 kHz. But, as it is already discussed in chapter 1, that majority of vibration sources don't have such high vibration frequencies. Hence important thing is to further increase the capacitance variation and the maximum capacitance of the transducer, while keeping the same surface area therefore still targeting low frequency vibration sources. This can be done by incorporating two topologies together. We are already using two electrodes which are present out-of-plane but having in-plane capacitance variation. So we can put comb electrodes as well, like in IPOC and IPGC so that we can have hybrid topologies like IPOP + IPOC or IPOP + IPGC. This can improve the capacitance variation. In order to increase the pull-in voltage, the design can be made where electrostatic force in one direction can be balanced by the other side.

4.3.2.2 Improvement of resonator bandwidth

The bandwidth of the resonator needs to be improved as well. Either this can be done by making the system more damped. But increase in damping reduces the power generation. As shown in Fig. 8 of chapter 1, reduction in the Q-factor by a ratio of 3 reduces normalized

power from 1 to 0.3. Hence the net efficiency of generator can be reduced. But we can adopt another approach by cascading more than one transducer which resonates at different frequencies. This idea already exists in the literature for micro-mechanical band pass filter [11]. This can help us to have high power generation as each transducer will have high value of Q-factor and at the same time net frequency response of the cascaded system will have relatively broadband frequency spectrum. This solution is not ideal since we need to increase the device area. A completely different approach for increasing the resonator bandwidth is to design the resonator springs so that they exhibit observable non-linear spring constant, leading to inharmonic behavior (Duffin effect) [12, 13]. Indeed such behavior leads to the deformation of the resonance curve in the frequency domain, which enlarges the frequency bandwidth. However, there is also a hysteretic behavior which requires special attention in the implementation of such a resonator for the application of harvesting energy from vibrations.

4.3.2.3 Improvement of the transducer electrical frequency

In order to improve the generated power, the electrical frequency of the transducer can be increased. The electrical frequency means number of times, the capacitance is varied from the maximum to the minimum value, during one mechanical cycle. It means that if in one mechanical cycle the number of electrical cycles can be increased, the net generated energy will be constant, but when this energy is multiplied by electrical frequency the generated power will be increased accordingly.

4.3.2.4 Bidirectional energy harvester

Most of energy harvesters presented until now based upon any of the geometries i.e. IPOC, IPGC, OPGP and IPOP (discussed in the chapter 1 and 2) have one degree of freedom (DOF) i.e. they can vibrate in only one direction (uni-directional). In many of real systems,

the axis of the external vibrations is not known *a priori* and if we assume that the available energy is equally distributed over the three degrees of freedom, the translational "2D"-transducer is potentially twice more efficient than its one-degree of freedom counterparts [14, 15]. We presented the design of an energy harvester which is sensitive to the vibrations in the 2 in-plane dimensions i.e. the design is bi-directional in appendix 2. The design, fabrication, initial characterization results along with the improvements in the design have been addressed as well.

Reference:

[1] B. C. Yen, H. L. Jeffery, "A variable capacitance vibration-to-electric energy harvester", *IEEE trans. on circuits and systems*, vol. 53, no. 2, *pp. 288-295*, Feb. 2006.

[2] P. D. Mitcheson *et al.,* "Architectures for Vibration-Driven Micropower Generators", IEEE/ASME *Journal of Microelectromechanical Systems,* vol. 13, no. 3, pp. 429-440 June 2004,

[3] P. D. Mitcheson, *et al.*, "Energy harvesting from human and machine motion for wireless electronic devices", *Proc. of IEEE*, vol. 96, no. 9, pp. 1457-1486, 2008

[4] S. P. Beeby, *et al.*, "A micro electromagnetic generator for vibration energy harvesting", *J. of Micromech. Microeng*., vol. 17, pp. 1257-1265, 2007

[5] M. Miyazaki *et al.,* "Electric-energy generation using variable-capacitive resonator for power-free LSI: efficiency analysis and fundamental experiment" *ISLPED'03* pp 193–198

[6] G. Despesse *et al.,* "Fabrication and Characterization of High Damping Electrostatic Micro Devices for Vibration Energy Scavenging", *Proc. of DTIP'05*, pp. 386-390, 2005

[7] T. Tsutsumino, *et al.*, "Seismic Power Generator Using High-Performance Polymer Electret", *Proc. of MEMS '06*, pp. 98-101, 2006

[8] W. Ma, *et al.*, "An Integrated Floating-Electrode Electric Microgenerator", *IEEE/ASME Journal of Microelectromechanical Systems*, vol. 16 no. 1, 2007

[9] Y. Suzuki, *et al.*, "Micro Electrets Energy Harvesting Device with Analogue Impedance Conversion Circuit", *Proc. of PowerMEMS'08*, pp. 7-10, 2008

[10] D. Galayko, *et al.*, "AMS modeling of controlled switch for design optimization of capacitive vibration energy harvester", *Proc. of IEEE Int. Behavioral Modeling and Simulation Conf. (BMAS'07),* pp. 115-120, 2007

[11] K. Wang and C. Nguyen, "High-Order Micromechanical Electronic Filters", *Proc. of IEEE International Micro Electro Mechanical Systems Workshop*, pp. 25 -30, 1997

[12] F. Cottone, *et al.,* "Nonlinear Energy Harvesting", *Proc. of Physical review letter*, pp. 080601-1 - 080601-4, 2009

[13] L. Gammaitoni, *et al.,* "Nonlinear oscillators for vibration energy harvesting", *Proc. of Applied Physics letters*, pp. 164102-1 - 164102-3, 2009

[14] A. Mahmood Paracha *et al.,* "MEMS DC/DC converter for 1D and 2D vibration-to-electricity power conversion", *Proc of Transducers 2009*, pp. 2098-2101, 2009

[15] U. Bartsch *et al.,* "A 2D Electret-based Resonant Micro Energy Harvester", *Proc. of MEMS'09*, pp. 1043-1046, 2009

Appendix 1
Matlab code to measure capacitance

In this appendix the code used to measure the capacitance in *Matlab*^{tm} is presented. The procedure of measurement is already explained in section 3.2. Here we will only give a code which will illustrate the matlab operations performed on the saved curves to measure the capacitance.

```
% To read the stored files
load c1.txt;
load c2.txt;

temps= c1(:,1);        %Time vector
vs=c1(:,2);            %Source voltage
v1=c2(:,2);            %Voltage value at the capacitance

offset_temps = temps(1,1);

temps = temps - offset_temps;        %To make the start of the readings from zero time

offset_dc=0;

N=1000002;   %Number of measured points
dT=10e-3;
fs=N/dT;   Sampled frequency
fsource=200e3;        % Frequency of the sinousoidal source
periode_sugg=1/fsource;
freq_res=1/dT;
et=length(temps);
Harmonics_corr=1000;   %The factor which corresponds to the harmonic noise

R1=5.6e3;  %Series resistance

dt=temps(3,1)-temps(2,1);

eY = fft(vs);              % Fourier transform of noisy signal
freq=0:freq_res:(fs-freq_res);

n = size(vs,2)/2; % use size for scaling
```

```
amp_spec = abs(eY)/n; % compute amplitude spectrum
fY = fix(eY/Harmonics_corr)*Harmonics_corr; % set numbers < 1000 to zero

ifY = ifft(fY); % inverse Fourier transform of fixed data
cy = real(ifY); % remove imaginary parts

eY1 = fft(v1); % Fourier transform of noisy signal

fY1 = fix(eY1/Harmonics_corr)*Harmonics_corr; % set numbers < 1000 to zero
ifY1 = ifft(fY1); % inverse Fourier transform of fixed data
cy1 = real(ifY1); % remove imaginary parts


% Zero crossing of the signal
fc_1 = 0.005; % Error factor of 0.5%

t_crois_vs = [];
j = 1;
act_crois=0;
for i = 1:( length(cy) - 1 )
   a = cy(i + 1);
   b = cy(i);
 if (a >= offset_dc & b < offset_dc) | (a <= offset_dc & b > offset_dc)
    prec_crois=act_crois;
    act_crois=temps (i);
 end
 if (((a <= offset_dc) & (b > offset_dc)) & (act_crois-prec_crois>fc_1*periode_sugg))
      t_crois_vs(j) = temps (i);
      j = j + 1;
  end
end

t_crois_vs_fin =[]; %Vs final vector

t_crois_vs_fin(1) = t_crois_vs(1);
k = 2;

for i=2:(length(t_crois_vs) - 1)
      if ( (t_crois_vs(i) - t_crois_vs(i-1)) > fc_1*periode_sugg )
         t_crois_vs_fin(k) = t_crois_vs(i);
         k=k+1;
      end


end

%Same algorithm for V1
t_crois_v1 = [];
j = 1;
act_crois=0;
```

```
for i = 1:( length(v1) - 1 )
   a = cy1(i + 1);
   b = cy1(i);

   if (a >= 0 & b < 0) | (a <= 0 & b > 0)
     prec_crois=act_crois;
     act_crois=temps (i);
  end
  if (((a <= 0) & (b > 0)) & (act_crois-prec_crois>fc_1*periode_sugg))
       t_crois_v1(j) = temps (i);
       j = j + 1;
    end

end
fc_2 = 0.005;
t_crois_v1_fin =[]; %Final vector of V1
t_crois_v1_fin(1) = t_crois_v1(1);
k = 2;
for i=2:(length(t_crois_v1) - 1)
       if ( (t_crois_v1(i) - t_crois_v1(i-1)) > fc_1*periode_sugg )
          t_crois_v1_fin(k) = t_crois_v1(i);
          k=k+1;
       end
end
for i=1:1:length(t_crois_vs_fin)
   m(i)=t_crois_vs_fin(i)-t_crois_v1_fin(i); %Difference of time in two signals VS and V1
end

index = 1;
item=1;

p_vs = t_crois_vs_fin(index + 1) - t_crois_vs_fin(index);
p_v1 = t_crois_v1_fin(index + 1) - t_crois_v1_fin(index);
freq_s = p_vs ^ -1;  %Applied AC frequency
w = 2*pi*freq_s;

while(item<=length(m))
   %t_diff = m;
   P_vs_new(item)=p_vs*item/2;
   t_diff(item)=m(item);
   angle_deph = 2*pi*t_diff(item)/p_vs; % To calculate phase difference from time
difference
   Cvar = 1/(w*R1*tan(angle_deph)); % To calculate capacitance
   Cv(item)=Cvar*1e12;
   item=item+1;
end
```

Appendix 2
Bidirectional energy harvester

This appendix presents the concept, design, fabrication, early characterization and design modifications of the bidirectional energy harvester. All the energy harvesters presented until now based upon any of the geometries i.e. IPOC, IPGC, OPGP and IPOP (discussed in the chapter 1 and 2) have one degree of liberty i.e. they can vibrate in only one direction (uni-directional). Here we present the novel design of the energy harvester which is sensible to the vibrations in the 2 dimensions in the plane i.e. the design is bi-directional. The 3D view of the proposed device is given in Fig. 1. The mechanical design is inspired from 2D gyroscope [1] and based on IPOP configuration. As in most of real systems, the axis of the external vibrations is not known and if we assume that the available energy is equally distributed over the three degrees of freedom, the "2D"-transducer is potentially twice more efficient than its one-degree of freedom counterparts. Recently few works have been presented regarding 2D-energy harvesters [2, 3].

Fig. 1 3D view of the bidirectional energy harvester

App.2.1 Design features

The net surface area of the device is 1 cm² (without taking into account the holes to access the metal contacts on a glass wafer). The targeted resonance frequency is 285 Hz. The mechanical spring constants have been calculated using the model of clamped-clamped beam and clamped-guided beam. The ratio between the vertical resonance frequency and the in-plane resonance frequency is calculated around 12. Since there are little vibrations at high frequency, the out of plane vibrations are minimized. The modeled value of pull-in voltage is 10 V. The patterned electrodes are of the spiral rectangular shape. This is being done to achieve the same capacitance variation in either direction in the plane.

Fig. 2 shows the FEM simulations based study of the substrate and the fringe capacitance. In the simulations the ground was applied to the substrate and top electrodes. When the electrodes are not superposing each other at the minimum capacitance position, the net capacitance, in practice, is equal to the fringe capacitance and substrate capacitance.

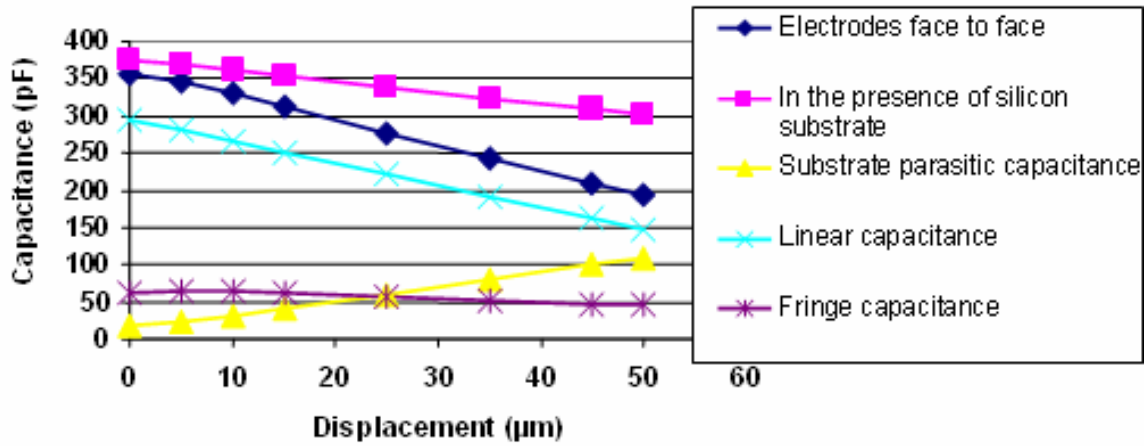

Fig. 2 FEM simulation based capacitance variation, with and without taking in account substrate, linear capacitance, substrate capacitance and the fringe capacitance

To maximize the max-to-min ratio of net capacitance, we have tried to reduce the substrate capacitance. It exists due to an electric field inside the silicon substrate. It is strong near to the top electrodes when they are positioned at a minimum capacitance point, as there is a direct

overlap of the silicon substrate and aluminum electrodes on glass wafer. In order to reduce the substrate capacitance, the silicon between the electrodes having a high permittivity and being not highly resistive should be replaced by air. It can be done by fabricating holes by through-wafer etching but this would reduce the mass of the resonator. We determined the optimal (minimal) depth of the silicon trenches in the substrate on the basis of FEM based simulations as shown in the Fig. 3, using *Coventor*^{tm}. It is shown that the minimum capacitance value decreases rapidly with an etched depth and after 20 µm it becomes constant around 205 pF instead of 302 pF (as in case without silicon etching). The value of the maximum capacitance remains constant with the back side DRIE around 370 pF. The fringe capacitance is also reduced by making the top electrode width 48 µm with respect to the bottom electrode width 50 µm. Table 1 illustrates the dimensions and design features of the presented transducer.

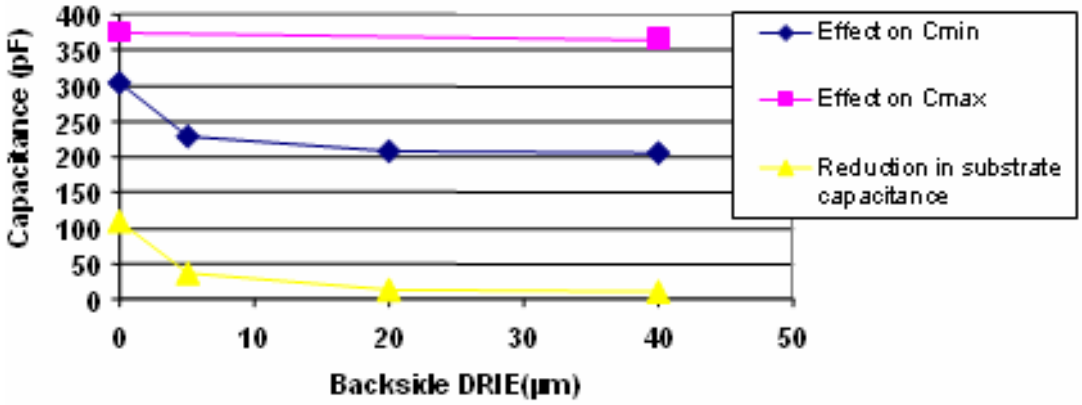

Fig. 3 Effect of backside DRIE on maximum and minimum capacitance (FEM simulation based result)

Table. 1 Main characteristics of the bidirectional energy harvester

Dimensions (mm^3)	10x10x0.9
Mass of mobile part (mg)	87
Horizontal resonance frequencies (fx,fy)	285 Hz (theory) 246 Hz (measured)
Vertical resonance frequency	3603 Hz
Pull in voltage	10 V
C_{min} / C_{max} (pF)	205/370
Couette damping	1.8e-3 Ns/m

App.2.2 Fabrication and characterization

The fabrication process is based on a silicon-glass technology. The details are exactly the same as explained in section 3.1 for uni-directional transducer. Fig. 4 shows a SEM picture of the back side of the proof mass with the zoomed view of the mechanical springs and the electrodes. During experiments, only the mechanical characterization has been performed until now. The devices have been excited with a vibration table from *Physik Instrumente*[tm]. The mechanical resonance frequency has been observed optically around 246 Hz. The observed value is less than the calculated value. It can be due to the defects during DRIE process which makes it impossible to predict a precise resonance frequency at the design level. Secondly the influence of the strong fluid damping present between the movable and fixed part can also be responsible for this resonance frequency reduction.

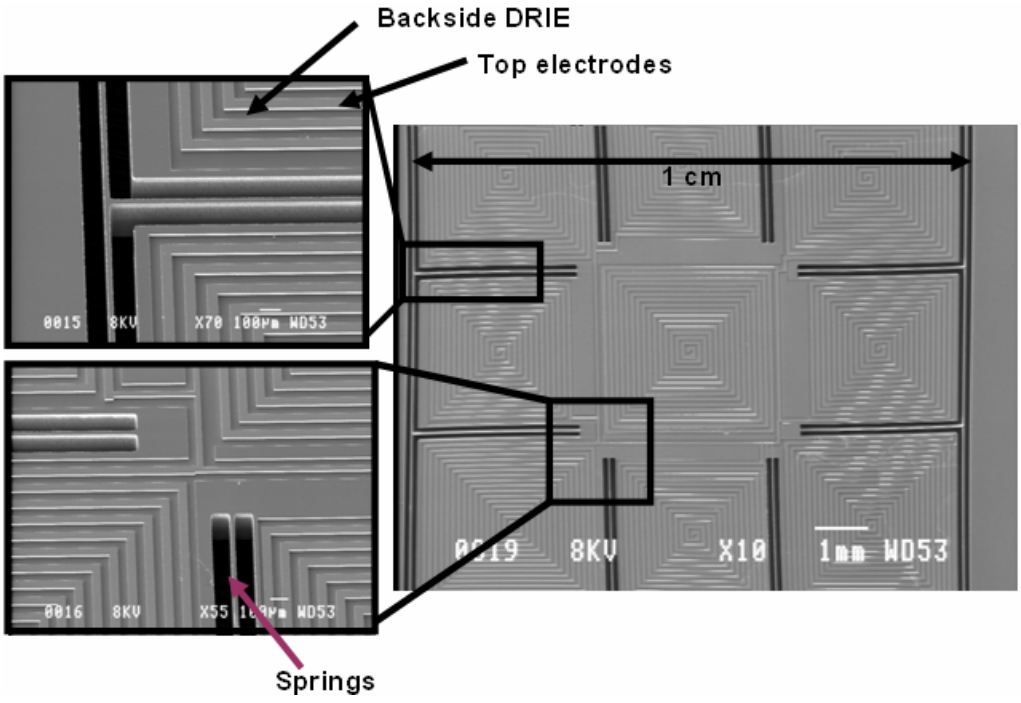

Fig. 4 SEM picture of the Silicon-wafer backside just before glass bonding

App2.3 Problem encountered and proposed modification in design

During the characterization it is being observed that proof mass does not exhibit the required displacement even when subject to the high acceleration in the range of 1*g* to 2g (we are limited to apply high accelerations than this value by vibration table). This fable displacement is due to the use of clamped-clamped beam to support the proof mass. The maximum distance which this beam can travel under the uniform load is given as [4]:

$$x = \frac{FL^3}{384EI}, \tag{1}$$

here *F, L, E* and *I* are force applied on the beam, length of beam, young's modulus of silicon and moment of inertia of beam. The volume dimension of one beam is 1 cm x 30 μm x 400 μm. The maximum displacement which corresponds to the acceleration of 1*g* and 2 *g* is 54 nm and 108 nm respectively. Hence as a solution the clamped-clamped beams should be replaced by clamped-guided beam to have large displacement and to have the useful power generation.

Reference:

[1] D. Piyabongkarn *et al.*, "Development of a MEMS gyroscope for absolute angle measurement", *IEEE transactions on control systems technology*, vol. 13, no. 2, March 2005

[2] A. Mahmood Paracha *et al.,* "MEMS DC/DC converter for 1D and 2D vibration-to-electricity power conversion", *Proc. of IEEE Transducers*, 2009

[3] U. Bartsch *et al.,* "Low-Frequency 2D-Resonators for Vibrational Micro Energy Harvesting Applications", *Proc. of PowerMEMS*, pp. 57-60, 2008

[4]http://www.codecogs.com/reference/engineering/materials/beams/beam_deflection_formulae_3.php, site visited 31/03/2009

Résumé en français

Résumé en français

1.0 Introduction

La technologie MEMS « Micro-Electro-Mechanical Systems» est une étape avancée de la technologie des circuits intégrés. C'est l'intégration de structures micro- mécaniques sur un substrat de silicium par fabrication collective base coût.. Les composants MEMS qui dominent le marché sont les suivants : têtes d'imprimantes à jet d'encre, capteurs de précision et micro-optiques pour vidéo projecteur [1]. Les autres domaines d'applications sont les MEMS inertielles (gyroscopes et accéléromètres), les MEMS-RF, la µ Fluidique et les microphones. Avec l'évolution des micros et nano technologies, le volume d'un capteur se réduit rapidement. Cette réduction est aussi accompagnée par une baisse de la puissance consommée par capteurs [2]. Avec cette réduction de puissance, le nouveau concept de capteurs autonomes émerge, c'est-à-dire des capteurs ne dépendant pas d'une source externe pour son alimentation, mais qui sont capables de générer de l'énergie électrique à partir de l'environnement ambiant.. Dans notre environnement, il y a beaucoup de réservoirs d'énergie qui peuvent être utilisés pour la génération d'énergie dont les ondes électromagnétiques ambiantes, la lumière, les variations de la température, l'écoulement d'air, les vibrations, etc. [3]. Les avantages de ce concept sont :

1) Suppression des fils utilisés pour les connections électriques entre la source d'énergie et les capteurs.

2) Augmentation de la durée de vie des capteurs et réduction des coûts de maintenance (pas de piles externes à remplacer).
3) Réduction ou voire même élimination des matières chimiques polluantes.

Ce concept permet de fournir des nœuds autonomes dans les réseaux des capteurs distribués (cf. Fig. 1). Chaque nœud est composé d'un capteur, d'une micro antenne [4], d'un CI et une source d'alimentation. Le capteur fait une mesure et envoie les données vers le serveur via une antenne.

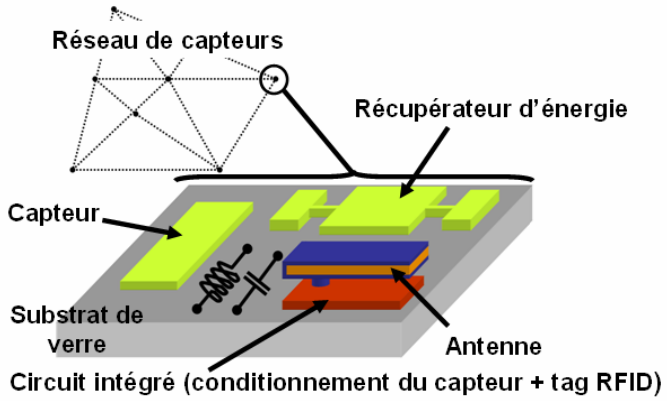

Fig. 1 Exemple d'un nœud dans un réseau de capteur sans fil

Les densités de puissance électrique générée par l'énergie solaire et les vibrations mécaniques sont parmi les plus intéressantes [5]. Dans une journée ensoleillée, la densité de la puissance générée par l'énergie solaire est autour de *15,000 µW/cm*^{3}, laquelle est réduite à 150 µW/cm^3 lorsque la journée ennuagée. À l'intérieur des bâtiments cette densité est réduite jusqu'au 6 µW/cm^3. Pour les applications qui sont installées en permanence dans les zones sombres sans accès direct à une source de lumière, l'énergie solaire n'est pas une solution réalisable. Pour alimenter des nœuds autonomes dans un réseau de capteurs et de « poussières intelligentes » [6], les vibrations ambiantes peuvent être dans des domaines comme l'aéronautique [8], l'automobile [7], le bâtiment [9], etc. Les vibrations mécaniques sont choisies comme source d'énergie renouvelable dans ce travail de recherche.

2.0 Etat de l'art de la récupération de l'énergie vibratoire

La conversion de l'énergie électrique à partir des vibrations mécaniques est réalisée en deux étapes. Dans un premier temps, une masse mobile est couplée avec les vibrations de l'environnement à l'aide à une liaison élastique (ressort) : la masse et le ressort constituent un résonateur mécanique. Grâce à ce couplage, la masse oscille dans le système de référence et accumule une énergie mécanique. La deuxième étape est la conversion de cette énergie en énergie électrique. Pour cela, un transducteur électromécanique doit appliquer à la masse mobile une force d'amortissement, c'est à dire doit effectuer un travail négatif sur le système mécanique. Dans le cas des transducteurs électromagnétiques, électrostatiques et piézoélectriques, la force d'amortissement électromécanique est créée par le champ magnétique, le champ électrique et la déformation de matériau piézo-électrique, respectivement [10, 11]. Un circuit électronique est nécessaire pour gérer le flux d'énergie électrique vers la charge électrique. L'architecture d'un convertisseur d'énergie mécanique en énergie électrique est illustrée Fig. 2.

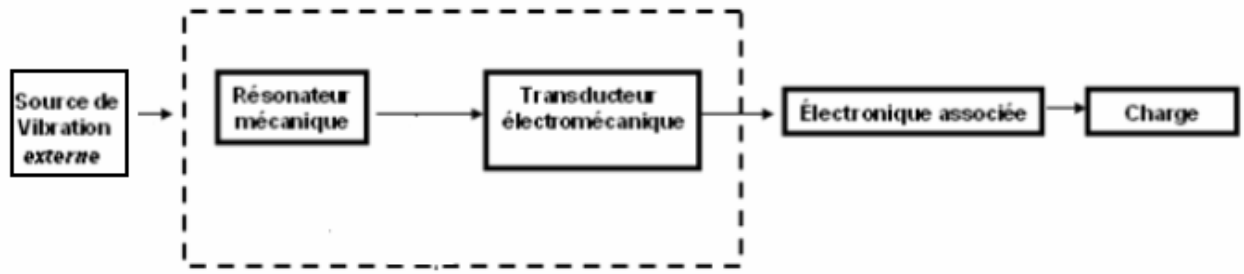

Fig. 2 Architecture générale d'un convertisseur d'énergie mécanique en énergie électrique

2.0.1 Générateurs résonnants et non résonnants

Les générateurs résonants sont destinés à des applications où l'amplitude de la source de vibration est faible par rapport au déplacement possible de la masse mobile et ne fonctionne que pour une bande étroite de fréquences spécifiques. Les générateurs non

résonnants sont utilisés dans des applications où les vibrations extérieures sont réparties dans une large bande spectrale (à basse fréquence) et où l'amplitude des vibrations est grande par rapport au déplacement possible de la masse mobile du résonateur [11].

2.0.2 Puissance maximum pour un transducteur résonnant

Un générateur résonant idéal est modélisé par un ressort, une masse et un amortisseur (cf. Fig. 3). Quand on écrit idéal, on signifie que l'amortisseur électrique est strictement proportionnel à la vitesse de la masse mobile, ce qui n'est vrai que pour des cas spécifiques. Parallèlement, l'équivalent électrique du système mécanique est également représenté. La puissance disponible peut être estimée selon l'équation dynamique du système, c'est-à-dire :

$$m\frac{d^2x}{dt^2}+(b_m+b_e)\frac{dx}{dt}+k_m x=-m\frac{d^2y}{dt^2}, \qquad (1)$$

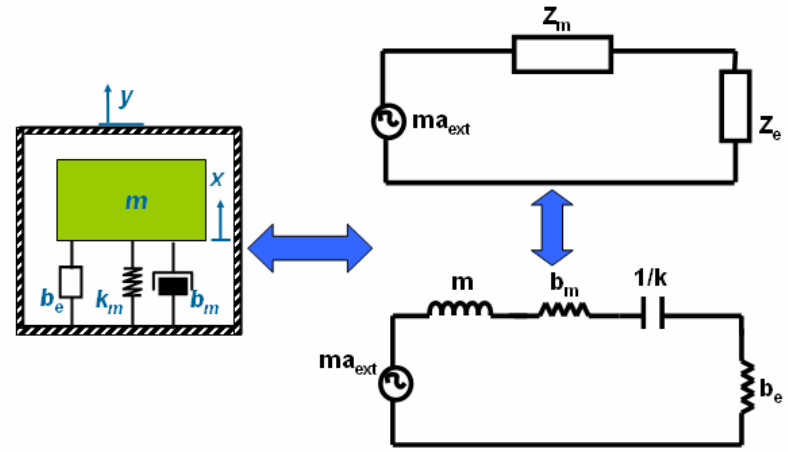

Fig. 3 Equivalent électrique d'un convertisseur d'énergie vibratoire résonant et idéal

où m est la masse de la partie mobile, b_m est l'amortissement mécanique et représente des pertes mécaniques, b_e est l'amortissement électrique qui est responsable de la conversion de l'énergie cinétique en énergie électrique, k_m est la raideur du ressort, x est le déplacement de la masse mobile par rapport au cadre , y est le déplacement du cadre et a_{ext} est l'accélération

externe. En supposant une excitation extérieure sinusoïdale ($y = Y \sin(\omega t)$), l'équation (1.1) peut se résoudre, pour obtenir la solution pour le déplacement de la masse, selon x [12] :

$$x = \frac{m\omega^2 Y}{\sqrt{\left(k_m - m\omega^2\right)^2 + \left((b_m + b_e)\omega\right)^2}}, \tag{2}$$

La puissance générée est la puissance moyenne convertie par l'amortisseur b_e :

$$P_e = \frac{b_e m^2 \omega^6 y^2}{2\left(\left(k_m - m\omega^2\right)^2 + \left((b_m + b_e)\omega\right)^2\right)}, \tag{3}$$

Le système génère une puissance maximale lorsque :

1) La fréquence de la source de vibration correspond à la fréquence de résonance mécanique du transducteur.
2) L'amortissement mécanique du système est égal à l'amortissement électrique.

En utilisant une analogie électrique, on peut dériver une expression pour la génération de la puissance maximale, incluant la contrainte du déplacement limité. Dans la Fig. 1.3. Z_m représente l'impédance mécanique du résonateur c'est-à-dire b_m. Z_e représente l'impédance mécanique du transducteur c'est-à-dire b_e qui est responsable de la conversion de l'énergie cinétique en énergie électrique. ma_{ext} est la force extérieure qui est appliqué par les vibrations mécaniques. Nous pouvons la représenter comme une source de la tension dans le réseau d'impédance. Dans le domaine mécanique, un courant électrique est représenté par une vitesse et nous pouvons trouver le courant en divisant la source de tension (force externe) par l'impédance totale du réseau. La puissance absorbée par Z_e est :

$$P = \frac{1}{2}\left|\frac{ma_{ext}}{Z_m + Z_e}\right|^2 \mathrm{Re}\left(Z_e\right), \tag{4}$$

Dans le domaine électrique un déplacement est représenté par une charge électrique :

$$x = \left| \frac{ma_{ext}}{Z_m + Z_e} \right| \frac{1}{\omega} \leq x_l , \tag{5}$$

ω est la fréquence de vibration et x_l est le déplacement autorisé. Selon les conditions décrites ci-dessous :

$$Z_m + Z_e = \frac{ma_{ext}}{\omega x_l}$$

$$\mathrm{Im}(Z_m) = -\mathrm{Im}(Z_e)$$

$$\mathrm{Re}(Z_m) = b_m = 0$$

Nous pouvons exprimer la puissance maximale avec la contrainte de déplacement :.

$$P_{\max} = \frac{1}{2} x_l y_{ext} \omega^3 m = \frac{1}{2} x_l a_{ext} \omega m , \tag{6}$$

On peut trouver l'équation (6) dans des références [14, 16], mais dérivée en se basant sur une méthodologie différente.

3.0 Méthodes de la conversion de l'énergie mécanique en électrique

Les techniques principales de transduction pour la récupération de l'énergie des vibrations de l'environnement ambiant sont électrostatiques [7], piézo-électriques [14], électromagnétiques [2] et magnétostrictifs [15] (cf. Fig. 4). Nous avons choisi la transduction électrostatique car elle a l'avantage de la compatibilité avec les procédés CMOS et elle est considérée comme la plus adaptée à la miniaturisation. Mais elle a aussi deux inconvénients : 1) d'avoir un faible rendement par rapports aux autres techniques et 2) la nécessité d'une énergie initiale). Mais ce transducteur est à considérer comme un des candidats les plus prometteurs dans la réalisation de systèmes intégrés pour les jours à venir.

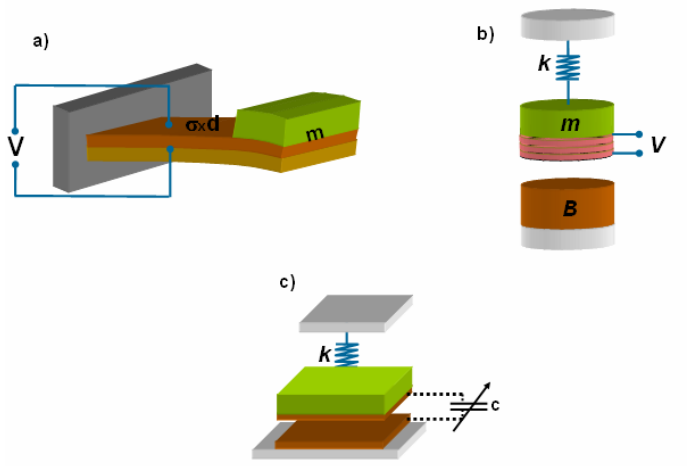

Fig. 4 Méthodes principales de transduction de l'énergie mécanique en énergie électrique : a) piézo-électrique, b) électromagnétique et c) électrostatique

3.1 Etat de l'art de la récupération d'énergie par transduction électrostatique

Le convertisseur résonnant électrostatique est un résonateur mécanique avec une capacité variable. Une des électrodes est attachée à la masse mobile qui bouge avec les vibrations et la seconde électrode est fixe. Le processus de récupération de l'énergie qu'on utilise garde la charge électrique du système constante. Il y a trois étapes :

1) charger le transducteur lorsque la capacité variable est maximale, soit par une source de tension externe ou par un condensateur réservoir déjà chargé,
2) en raison des vibrations, il y a en mouvement de la masse mobile et de l'électrode correspondante, pour permettre à la capacité d'atteindre sa valeur minimale, tout en maintenant une charge constante qui augmente l'énergie nette stockée,
3) décharger la capacité lorsqu'elle a atteint sa valeur minimale. L'expression mathématique de l'énergie électrique qui est générée est [16] :

$$\Delta E = E_O\left(\frac{C_{\max}}{C_{\min}} - 1\right), \tag{7}$$

où *Eo* est l'énergie électrique initiale du système, C_{max} et C_{min} sont les valeurs maximum et minimum des transducteur. Mais cette équation n'est valable que quand il y a deux conditions:

1) l'électronique associée avec le transducteur est sans perte
2) toute la charge électrique retourne vers le réservoir en état minimale de la capacité

Généralement, il existe quatre géométries de transducteurs qu'on utilise pour le récupération de l'énergie par transduction électrostatique, ce sont : « In-Plane Overlap Comb (IPOC) », « In-Plane Gap-closing Comb (IPGC) », « Out-of-Plane Gap-closing Plates (OPGP) [17] » et In-Plane Overlap Plates (IPOP) [13] (cf. Fig. 5). IPOC et IPGC ont l'architecture de peignes inter-digités. En IPOC la variation de capacité existe en raison du chevauchement variable et en IPGC il y a changement de l'entrefer, mais dans les deux cas la masse mobile bouge dans le plan. L'architecture de OPGP et IPOP est des plaques parallèles. En OPGC la capacité change parce qu'il y a un mouvement de la masse mobile hors plan et donc variation de l'entrefer. En IPOP la variation de la capacité est liée au changement du chevauchement des électrodes en raison d'un mouvement de la masse mobile dans le plan. Nous avons choisi la structure IPOP car elle permet d'obtenir une très grande capacité variable.

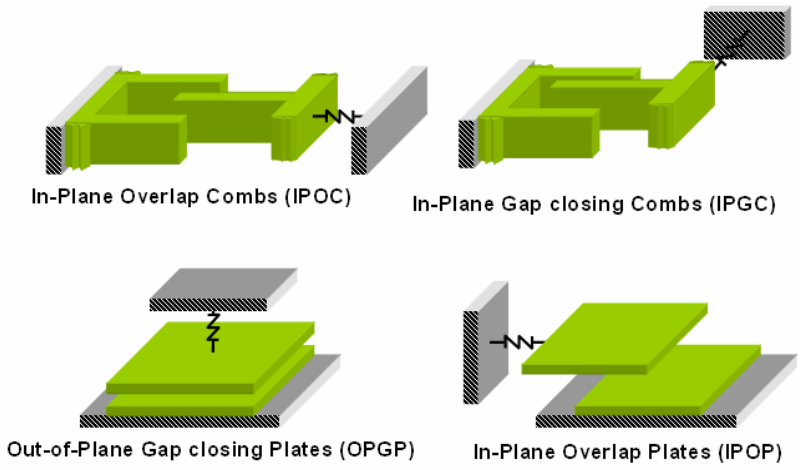

Fig. 5 Les topologies utilisant pour récupération de l'énergie avec le transduction électrostatique

4.0 Le système global

Le circuit de conditionnement choisi, pour notre transducteur a été présentée dans [18]. Le schéma est montré Fig. 6. Son fonctionnement se décompose en deux phases : 1) l'accumulation d'énergie par une pompe de charge et 2) la recharge d'une capacité réservoir C_{Res} par un retour inductive (Flyback). La commutation entre les deux phases est réalisée par le commutateur *Sw*, qui doit être à l'état ouvert (OFF) pendant que la pompe de charge est en fonctionnement. La résistance de charge R_{load} est mise en parallèle à C_{Res}. C_{Res} récupère la charge électrique en sortie de la pompe de charge quand *Sw* est en état (fermer) ON.

Dans le cadre de cette thèse, nous avons établi la formulation de l'énergie générée par la transduction électromécanique à l'aide de la pompe de charge. La partie flyback n'a pas été traitée, cependant des travaux sont en cours pour construire un commutateur intelligent afin de réaliser un flyback et obtenir un système complet [19].

.

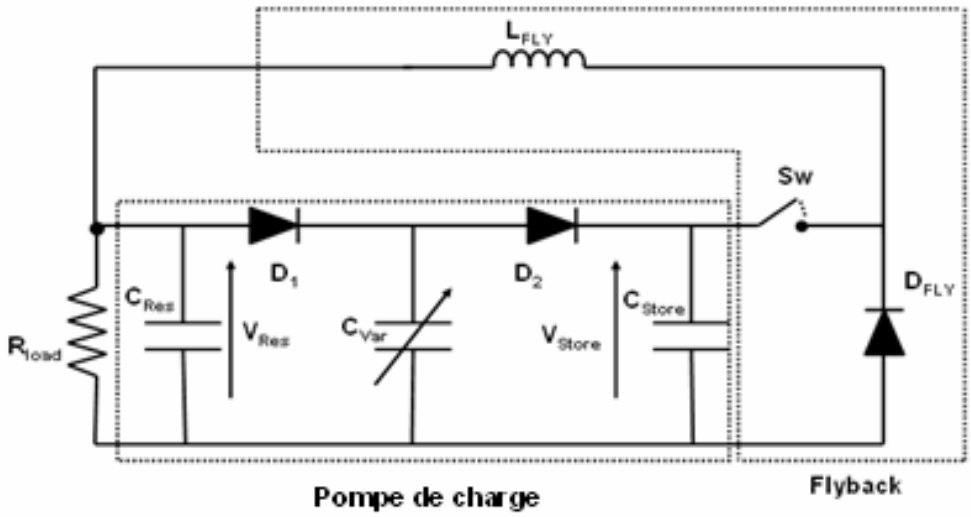

Fig. 6 Système global [18]

4.1 Fonctionnement de la pompe de charge

La pompe de charge convertit l'énergie mécanique en énergie électrique. Ainsi elle permet de définir la puissance récupérée. Elle comprend trois capacités et deux diodes. Les

capacités sont les suivantes : la capacité réservoir (C_{Res}) qui donne l'énergie initiale au système, la capacité variable C_{Var} (ayant un maximum C_{MAX} et un minimum C_{MIN}) qui varie sous l'effet des vibrations externes, et la capacité de stockage C_{Store}, elle est utilisée pour stocker la charge électrique pendant le processus de conversion électromécanique. Les diodes D_1 et D_2 sont des interrupteurs passifs.

Supposons les conditions initiales sur la pompe de charge décrites ci-dessous :

$$V_{Res} = V_{store} = V_{var} = V_0 > 0,$$

$$C_{Var} = C_{MAX}$$

D_1 et D_2 sont en état OFF

On suppose que la chute de tension à travers les diodes est nulle en état ON. Quand le résonateur commence à vibrer, C_{Var} diminue et la tension du transducteur V_{var} augmentes, ce qui va changer l'état de la diode D_2 en *ON*. Donc il y aura un flux de la charge électrique de C_{Var} vers C_{store}. Une fois que la capacité est devenue minimum, C_{Var} commence à augmenter et V_{var} à baisser, donc D_2 passe à l'état OFF. Quand V_{var} arrive jusqu'au niveau de V_{Res}, D_1 entre à l'état ON. Puis il y aura le flux de la charge électrique de C_{Res} vers C_{Var}. V_{Store} augmente et V_{Res} baisse avec les vibrations, mais la charge électrique est toujours constante. Pour garder V_{Res} constant, durant le fonctionnement de le pompe de charge, il faut avoir C_{Res} >> C_{Store} et C_{Var} . L'expression de V_{Store} est [18] :

$$\left(V_{store}\right)_n = V_O\left[\left(1-\frac{C_{\max}}{C_{\min}}\right)\left(\frac{C_{Store}}{C_{Store}+C_{\min}}\right)^n + \frac{C_{\max}}{C_{\min}}\right], \tag{8}$$

où n est nombre des cycles de la pompe. Quand n tend vers l'infini, V_{Store} a une valeur constante. Cet état est la saturation de la pompe de charge, la tension de saturation est :

$$V_{sat} \approx \frac{C_{\max}}{C_{\min}} V_O, \tag{9}$$

L'augmentation de l'énergie stockée par C_{Store} est :

$$\Delta E_{1\to n} = \frac{C_{Res} C_{Store}}{2(C_{Res} + C_{Store})}\left((V_{store})_n - (V_{Res})_n\right)^2, \quad (10)$$

Comme C_{Res} >> C_{Store}, l'équation (10) devient :

$$\Delta E_{1\to n} = \frac{C_{Store}}{2}\left((V_{store})_n - V_{Res}\right)^2, \quad (11)$$

Fig. 7 représente l'évolution de la tension et l'énergie de C_{Store} en fonction du nombre de cycles de la pompe en utilisant les équations (8) et (11). La valeur des composants utilisés pour faire ces courbes sont : C_{Res} =1 µF, C_{store} = 3,3 nF, C_{MAX} = 200 pF, C_{MIN} = 100 pF et V_O = 5 V.

V_1 et V_2 (cf. Fig. 7) sont les niveaux de tension entre V_O et V_{sat}, qui correspondent aux cycles n_1 et n_2 respectivement. Si l'opération de flyback est initiée de V_2 à V_1 (*Sw* est ON), l'énergie stockée par C_{Store} baisse de E_2 à E_1. Cette diminution de l'énergie est utilisée pour charger C_{Res} et alimenter la charge résistive. Ces niveaux de tension doivent être optimisés pour maximiser la puissance récupérée. Si on néglige le temps de flyback, la puissance moyenne récupérée est :

$$P = \frac{E_2 - E_1 - E_{Flyback,loss}}{(n_2 - n_1)T}, \quad (12)$$

$E_{Flyback,loss}$ est l'énergie dissipée par l'interrupteur pendent « flyback » et T est le durée d'une cycle de la pompe.

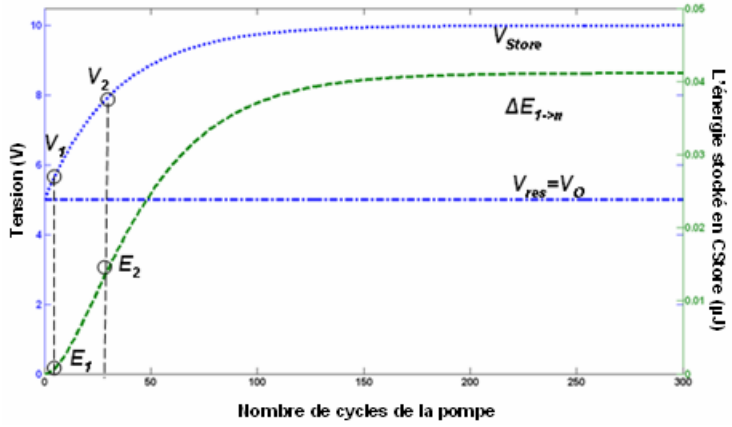

Fig. 7 Energie de C_{store} et tensions de C_{store} et C_{Res} en fonction du nombre de cycles de pompes

5.0 Conception d'un résonateur : architecture et dimensionnement

A la base de la configuration IPOP, nous proposons deux structures du résonateur mécanique appelé: 1) Proof mass Configuration (PC) et 2) Comb Configuration (CC). Dans la sous-section, nous discuterons le dimensionnement de ces structures. Les contraintes suivantes sont fixées :

- L'area de la surface du transducteur (Masse mobile + ressort) + plots de contact < 1 cm²
- Fréquence de résonance latérale, f_x = 250 Hz
- Ratio entre la fréquence de résonance latérale et verticale > 10
- La tension de Pull-in > 10 V

Les contraintes technologiques sont imposées par la gravure DRIE. Comme il y a des surfaces de silicium à graver de dimensions différentes, la largeur minimale de ressort est 30 µm.

5.1 « Proof mass Configuration » (PC)

La Fig. 8 montre l'image 3D du convertisseur d'énergie basé sur la topologie IPOP.

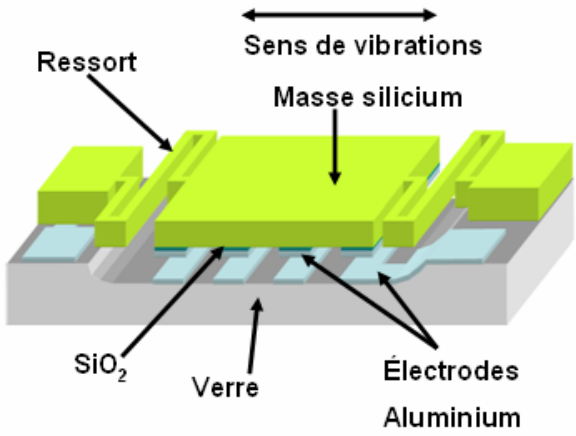

Fig. 8 Proof mass Configuration (PC)

Les caractéristiques mécaniques basées du convertisseur PC sont résumées ci-dessous :

Masse de la partie mobile	59,684 mg
les fréquences de résonance latérale et verticale	250 Hz and 3464 Hz
L'amortissement fluidique *b*	7,68e-4 Ns/m
Facteur de qualité	146

La Fig. 9 montre les simulations FEM de la variation de la capacité totale. Elle se compose d'une capacité linéaire, d'une capacité due aux effets des bords, de la capacité qui existe à cause du substrat et à cause des connections. Pour V_{in} égal à 5V et 6 V, la puissance récupère maximale (avec C_{MAX} = 199 pF et C_{MIN}=135 pF), obtenue à l'aide de l'équation (7), est de 0,5 µW et 0,85 µW respectivement. Pour obtenir la puissance, l'énergie est multipliée par 2 fois la fréquence de résonance, car dans un cycle mécanique, il y a deux cycles de variation de la capacité. La tension de pull-in théorique est de 10 V.

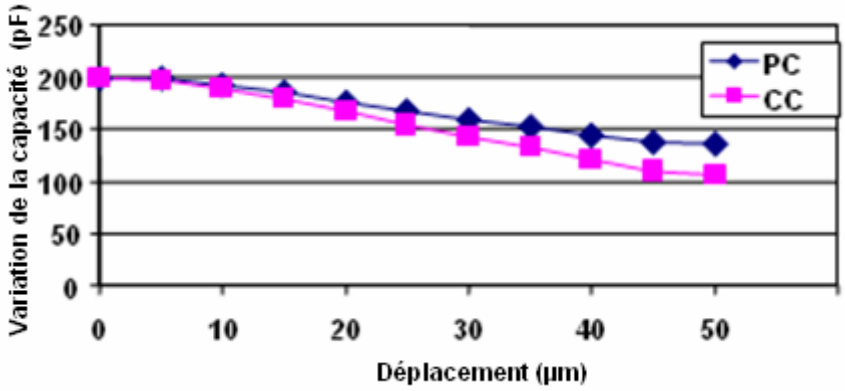

Fig. 9 Capacité totale pour les structures PC et CC obtenue par simulations FEM

5.2 « Comb Configuration » (CC)

L'architecture CC est la modification de la configuration PC. Le problème avec PC est la grande valeur de la capacité avec le substrat lorsque $C_{var} = C_{min}$. La solution proposée est de graver le silicium partiellement au niveau de l'espace présent entre les électrodes afin de réduire la capacité parasite. Cela induit une baisse de la masse totale de la partie mobile, par conséquent il y aura une augmentation de la fréquence de résonance par rapport à la structure PC. La Fig. 10 montre la vue 3D du dispositif.

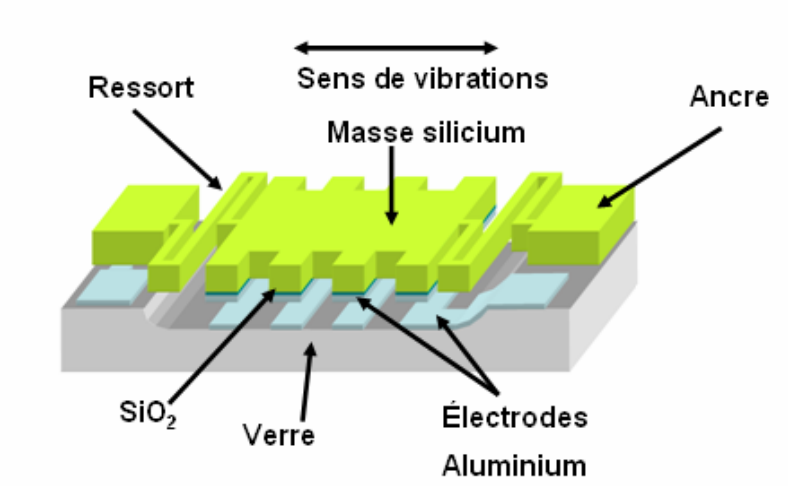

Fig. 10 Comb Configuration (CC)

Avec l'équation (7), pour V_{in} égale à 5V et 6 V, la puissance maximale récupérée (avec C_{MAX} = 198 pF et C_{MIN}=105 pF, cf. Fig. 9) pour 250 Hz est 1,1 µW et 1,58 µW respectivement (les valeurs de la capacité sont obtenues par des simulations FEM). Toutes les autres spécifications (la fréquence de résonance, le ratio de la fréquence de résonance verticale à fréquences de résonance horizontale et la tension de pull-in) sont les mêmes que pour la configuration PC. Seulement, un ajustement est fait entre la masse et le ressort pour baisser la fréquence de la masse mobile.

5.3 Modification du dessin avec « Backside DRIE » (BD)

Dans la configuration CC, 19% de la masse totale de silicium est enlevée par rapport à la configuration PC, ce qui va diminue la capacité parasite et donne une densité d'énergie supérieure. Mais cette réduction de la masse augmente la fréquence de résonance, ce qui n'est pas désiré, puisque les fréquences de résonance de la plupart des sources de vibrations utiles se trouvent en dessous de 250 Hz.

Afin de réduire la capacité parasite, le silicium qui est placé entre les électrodes et qui a une haute permittivité et conductivité doit être remplacé par de l'air. Nous pouvons l'atteindre en gravant sur toute la largeur de plaque du silicium, comme nous l'avons fait dans le cas de CC. Pour limiter la perte de masse, nous proposons de graver la petite profondeur de silicium. Cette étape est appelée « Backside DRIE » (BD). La Fig. 11 montre une vue de côté du design modifié. La Fig. 12 montre la variation de C_{max} et C_{min} en fonction de la profondeur de gravure, basée sur des simulations FEM, à l'aide de *Coventorware*^{tm}. On peut en conclure qu'il n'est pas nécessaire de graver toute l'épaisseur de la plaque de silicium. La valeur de C_{min} diminue très rapidement avec la profondeur de gravure, mais après 20 µm elle devient presque constante. Avec une gravure de 20 µm, la perte de la masse est 2,5% au lieu de 19% en configuration CC. Cela ne change pas la valeur de C_{max}. Avec l'équation (7), pour V_{in} égal à 6 V, la puissance maximale récupérée (avec C_{var} = 141 pF) pour 253 Hz est de 5.13 µW.

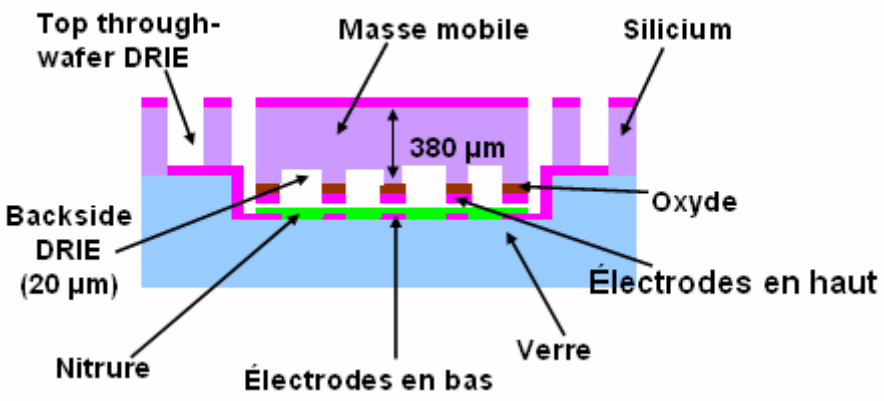

Fig. 11 Structure modifiée

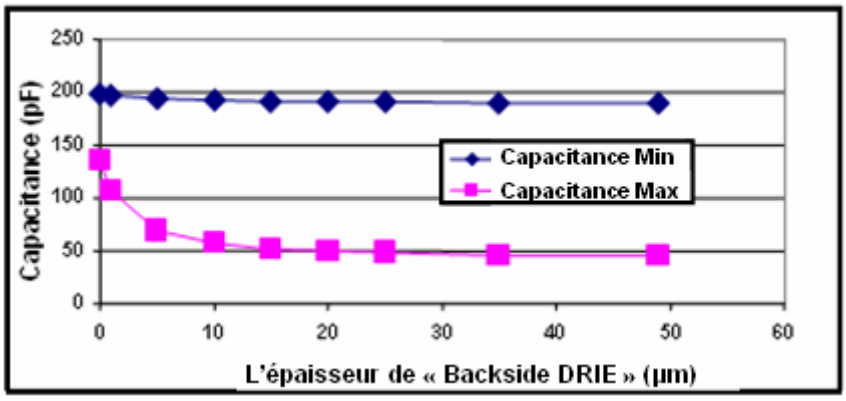

Fig. 12 La capacité maximum et minimum avec l'épaisseur de gravure

6.0 Procédé de fabrication

On a utilisé une technologie silicium-verre pour fabriquer le convertisseur de l'énergie mécanique en énergie électrique. On dépose des électrodes en aluminium sur une plaque de silicium et sur une plaque de verre, après les deux sont soudées en utilisant la soudure anodique. Il y a six niveaux de masques nécessaires à la fabrication. Les étapes sont représentées Fig. 13. Afin d'éviter un collage entre les électrodes, 2000 Å de nitrure sont déposés par PECVD sur l'électrode inférieure, qui est déposée sur verre préalablement gravé par HF. Un dépôt d'oxyde thermique sur le silicium isole ce substrat par de l'électrode d'aluminium. Une épaisseur de 20 µm de silicium est gravée par DRIE entre les motifs de l'électrode supérieure afin de réduire la capacité parasite.

La plus importante étape dans la fabrication est la gravure profondeur (DRIE) sur toute l'épaisseur du silicium pour la réalisation des ressorts. On utilise l'équipement « *Alcatel*^{TM} 601E plasma etcher ». Pour atteindre un profile de gravure verticale et anisotrope, le procédé Bosch est utilisé. La Fig. 14 montre une vue microscopique de la face arrière du subtrat de silicium après DRIE. La vue de dessus du dispositif final est montrée dans la Fig. 15.

Etap	schéma	Explications
1		Verre (500 µm) graver chimiquement (1,7 µm) par HF (Masque 1)
2		Pulvérisation d'Al (0,5 µm) électrodes en bas, photolithographie et gravure (Masque 2)
3		Le dépôt de nitrure par PECVD (0,2 µm), photolithographie et gravure (Masque 3)
4		Oxydation thermique (0,5 µm) + Pulvérisation d'Al électrodes en haut (0,5 µm), photolithographie et gravure de l'oxyde et al (Masque 4)
5	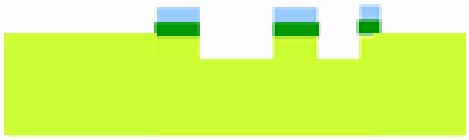	Back side DRIE (20 µm) (Masque 5)
6		Pulvérisation d'Al pour utiliser comme masque pendent DRIE (0,5 µm) (Masque 6)
7	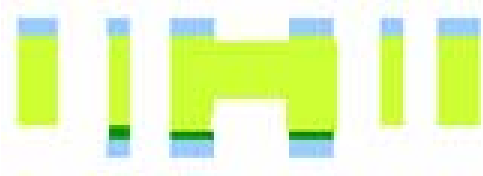	Garvure à toute l'épaisseur du silicium (Through wafer DRIE) (380 µm)
8		Soudure anodique

Fig. 13 Processus de fabrication

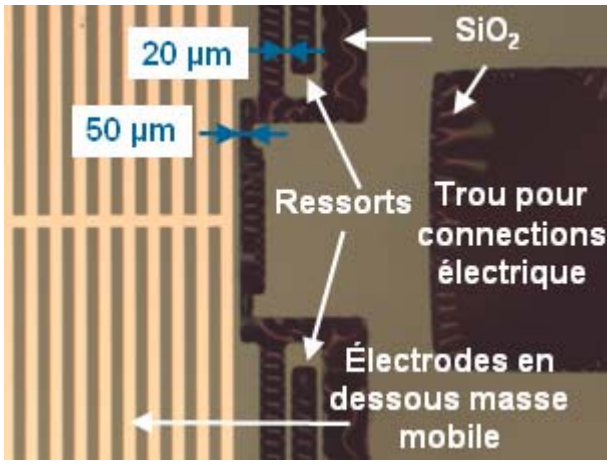

Fig. 14 Vue de la face arrière du substrat de silicium après DRIE

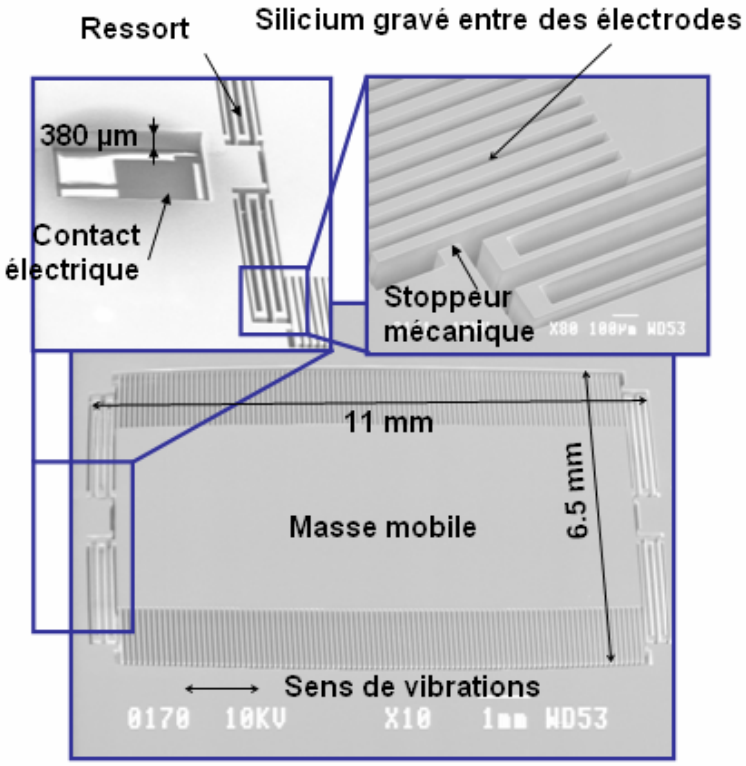

Fig. 15 Vue de dessus du dispositif final

7.0 Caractérisation dynamique du transducteur

Afin de caractériser le dispositif, les résonateurs ont été montés sur un circuit imprimé (PCB). La connexion avec le circuit électronique de conditionnement a été fait par « Wire Bonding » (cf. Fig. 16). Le PCB est fixé sur une table vibrante, de type *P-6201.1* de *Physik*

Instrumente^{tm}. Nous avons appliqué des vibrations mécaniques dans le plan du substrat. Une mesure dynamique de C_{var} est obtenue en mesurant le décalage de phase dans un circuit RC_{var} alimenté avec une tension alternative à une fréquence beaucoup plus élevée que la fréquence des vibrations mécaniques s (cf. Fig. 17).

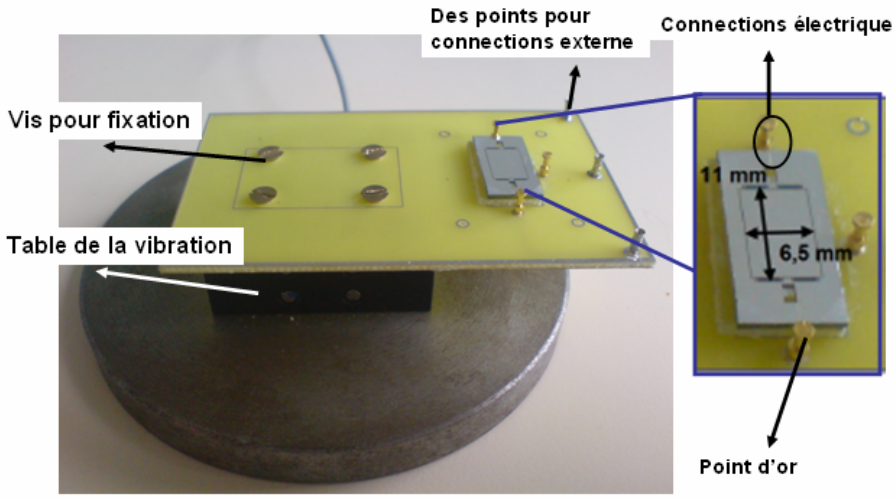

Fig. 16 Banc de mesure avec le dispositif

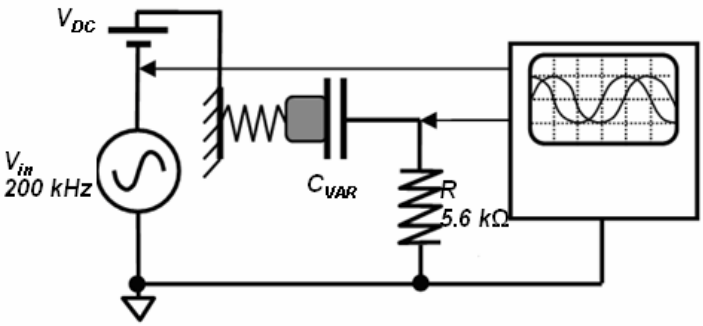

Fig. 17 Schéma du banc la mesure pour la caractérisation dynamique de la capacité du transducteur

La capacité est calculée par l'expression :

$$C_{\text{var}} = \frac{1}{\tan(\theta) R\omega}, \tag{13}$$

où ω est la pulsation de la source V_{in}, θ est le déphasage entre la tension aux bornes de la capacité et la tension générée par la source AC. Nous pouvons calculer l'erreur relative par la formule:

$$\frac{\Delta C_{\text{var}}}{C_{\text{var}}} = -2\frac{Ts\omega}{\sin\left[2\tan^{-1}\left(\frac{1}{\omega R C_{\text{var}}}\right)\right]} \quad , \tag{14}$$

où *Ts* est la période d'échantillonnage de l'oscilloscope.

7.1 Mesure de la variation de la capacité du transducteur

Des vibrations dans le plan sont appliquées au dispositif, la résonance mécanique du dispositif est observée optiquement à 250 Hz, avec une accélération minimale de 0,1 g. Avec ces paramètres le déplacement de la masse mobile est de 50 μm, la distance maximale autorisée. La fréquence de la tension AC est fixée à 200 kHz. Les mesures ont été effectuées avec un oscilloscope, le *Croy*^{tm} *9354AL*, ayant un temps d'échantillonnage T_s égal à 10 nsec et avec une résistance R de 5,6 kΩ. En appliquant une tension alternative de 500 mV sur C_{var}, on mesure une variation de la capacité de 73 à 144 pF comme montré dans la Fig. 18. Dans un cycle mécanique, la masse mobile passe deux fois par la position de la capacité maximum, donc la fréquence de variation de C_{var} est deux fois la fréquence des vibrations mécaniques. L'équation (14) donne une erreur relative maximale autour de 3,1%.

Lorsqu'une tension continue V_{dc} est aussi appliqué en plus de la tension sinusoïdale V_{in} (Fig. 17), la force électrostatique entre les électrodes verticales en haut et en bas tire la masse mobile vers le substrat et réduit ainsi le rapport C_{max}/C_{min}, car cela augmente plus la capacité parasite que C_{max}. L'accélération nécessaire pour atteindre un déplacement augmente également. A V_{dc} égale à 8 V, le rapport mesuré C_{max}/C_{min} est 1,3 (cf. Fig. 19) et l'accélération nécessaire est de 0,25 g. Cela correspond à une réduction d'entrefer de près de 40%.

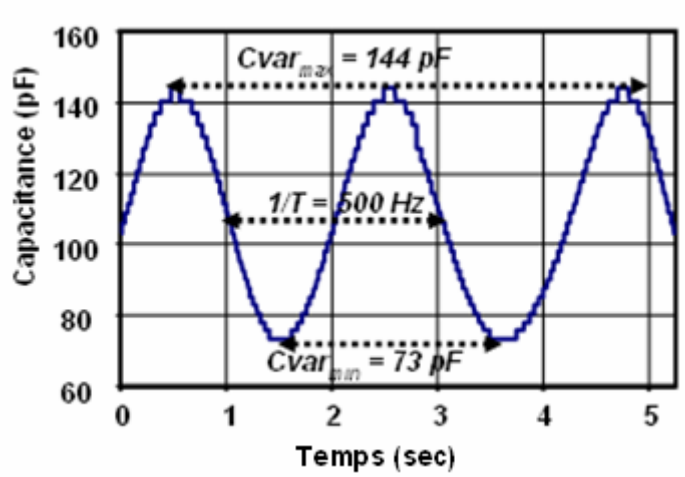

Fig. 18 Variation de la capacité sans tension DC

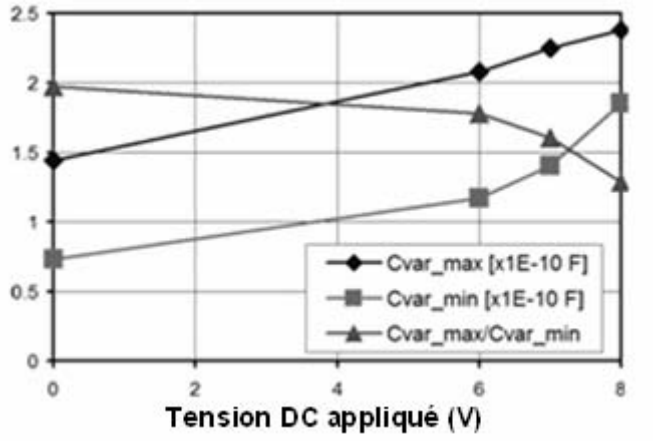

Fig. 19 Mesure de $Cvar_{max}$, $Cvar_{min}$ et $Cvar_{max}/Cvar_{min}$ en fonction de la tension DC

La valeur mesurée est de 144 pF et 73 pF au lieu de 200 pF et 50 pF obtenue par simulations. Ceci est du à :

1) L'épaisseur de gravure de verre qui est de 1,69 µm au lieu de 1,5 µm.
2) Le substrat n'était pas polarisé durant la mesure.

8.0 Le facteur de la qualité (Q-factor)

La caractérisation du facteur de qualité mécanique du transducteur nous permet de calculer l'amortissement mécanique du résonateur.

La Fig. 20 montre la réponse en fréquence du résonateur. La bande passante à -3 dB est de 1,7 Hz et la fréquence de résonance est 250,5 hertz. Le facteur de qualité est donc de 147. L'amortissement fluidique est calculé à 5,02 10-4 Ns / m.

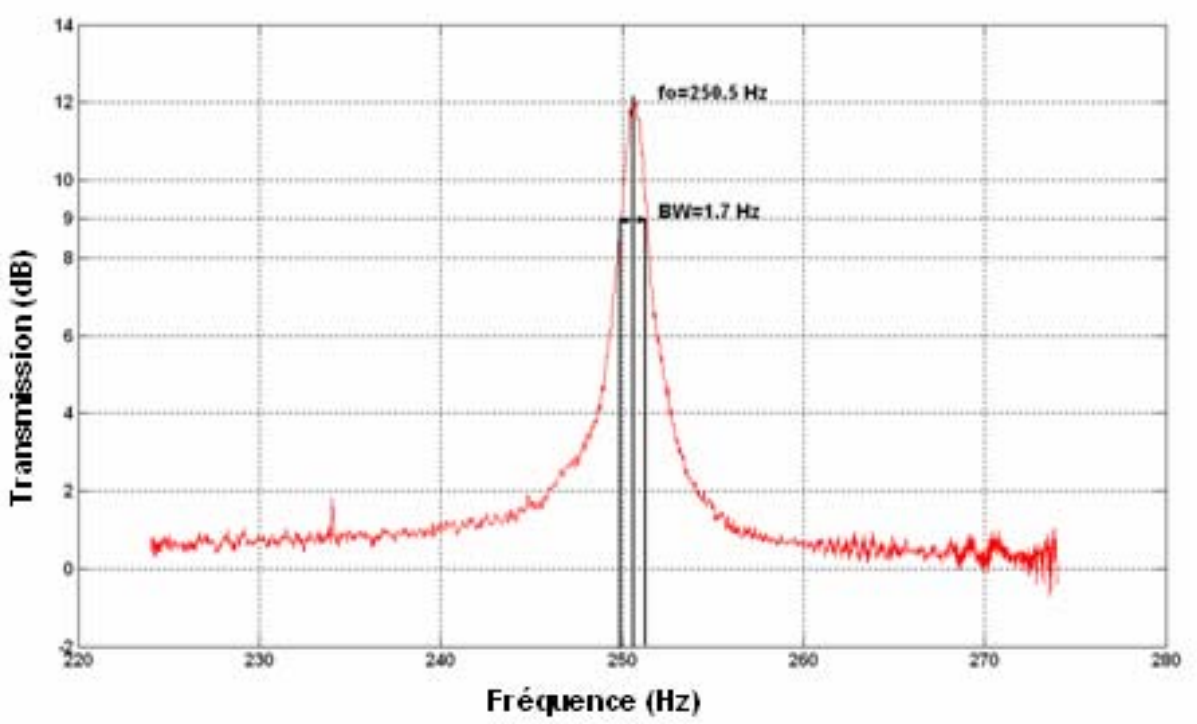

Fig. 20 Réponse fréquentiel du résonateur

9.0 Mesure de la puissance convertie en utilisant la pompe de charge

Le circuit de pompe de charge utilisé est donné dans la Fig. 21. C_{res} C_{var} et C_{store} sont d'abord pré-chargés avec la tension DC V_o. Ensuite, la source de tension est coupée et le système devient électriquement autonome. Le circuit électrique a trois sources d'énergie : C_{res} et C_{store} qui se déchargent, et le capteur capacitif qui transforme l'énergie mécanique en énergie électrique. Cette énergie se dissipe dans la charge résistive et dans les diodes. L'équation du bilan de la puissance électrique correspondante est:

$$P_{mec} + P_{Cres} + P_{Cstore} = P_{Rload} + P_{diodes}, \quad (15)$$

où P_{mec} est la puissance générée par les vibrations mécaniques, P_{Rload} et P_{diodes} sont les puissances dissipées par la charge et les diodes, et P_{Cres} et P_{Cstore} sont les puissances fournies

par les décharges de C_{res} et C_{store}. P_{Cres}, P_{Cstore} et P_{Rload} peuvent être considérées comme constantes sur un petit intervalle de temps Δt et mesurées directement. P_{diodes} est estimée par le produit de la chute de tension dans les diodes et le courant moyen (C'est la même pour les deux diodes). Il est calculé comme :

$$\bar{I}_{diodes} = -\frac{\Delta Q_{res}}{\Delta t} = \frac{C_{res}\left[V_0 - V_{res}(\Delta t)\right]}{\Delta t}, \quad (16)$$

où ΔQ_{res} est la variation de la charge électrique dans C_{res} pendent Δt et $V_{res}(\Delta t)$ est la tension aux bornes de C_{res} après un intervalle de temps Δt.

Dans notre expérience, le système est pré-chargé avec V_0 = 6 V, correspondant à environ la moitié de la tension de pull-in. Ainsi, à chaque période de la variation de C_{var}, la pompe de charge transfère la quantité de charge $(C_{max}\text{-}C_{min})V_0$ ~ 420 pC de C_{res} vers C_{store}, ce qui correspond à un courant moyen de ~210 nA. Les courants de fuite doivent être beaucoup plus petits pour réaliser des mesures exactes. Dans notre configuration de mesure, nous avons utilisé JPAD5 diode qui n'a que 5 pA de fuite. Cette faible valeur de courant impliquent pas que les tensions directes des diodes sont plus basses que l'habituel 0,6-0,7V. Notre modélisation et des mesures indirectes indique un V_d de 0,4 V pour ces niveaux de courants.

La mesure sans R_{load} identifie la tension de saturation de la pompe de charge V_{store_sat} à 8,4 V. De la théorie, $V_{store\_sat} = (V_0\text{-}V_d)\ C_{max}/C_{min}\ \text{-}V_d$ soit près de 8.45 V pour C_{max}/C_{min} =1,45 et V_d= 0,1V. Cette tension faible de la diode s'explique par le fait qu'il n'y a presque pas de charge transférée une fois de la pompe de charge saturée.

Ces mesures sont également modélisées en utilisant un modèle en langage VHDL-AMS présenté dans [19][1], avec C_{max}/C_{min} de 1.45 et avec un modèle exponentiel de diode. La différence entre la mesure et la simulation est de 3% [20].

On a testé le transducteur avec des résistances de charge de 30 à 150 MΩ.La Fig. 22 montre les valeurs de P_{mec}, calculées à partir des évolutions de tension mesurées et simulées.

[1] Cette partie du travail est faite par M. D. Galayko de LIP-6 Paris

Lorsque la puissance dissipée dans les diodes est calculée à partir de (16), avec V_d = 0,4V constant, on obtient la puissance de 61 nW pour une charge de 60 MΩ. La puissance extraite par la modélisation nous donne une puissance maximale de 79 nW pour une charge optimale de 90 MΩ. L'écart résulte de la difficulté à rendre compte correctement des pertes dans les diodes dans le calcul de la puissance à partir de l'expérimentation.

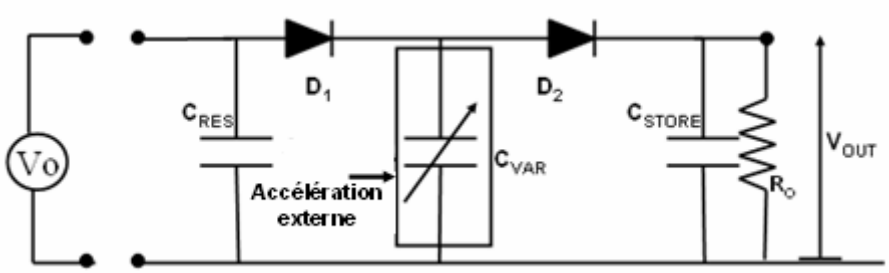

Fig. 21 Pompe de charge utilisée pour la mesure de la puissance convertie

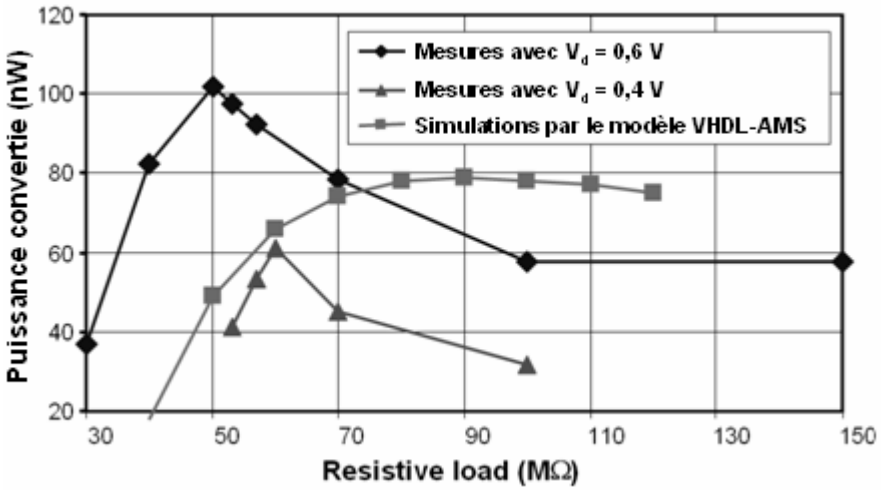

Fig. 3.22 Mesures des puissances récupérées tension de diodes 0.4 et 0.6 V et comparaison avec la simulation

9.0 Conclusions

Ce dispositif est le premier convertisseur de l'énergie électrostatique fabriqué avec un processus compatible avec CMOS sans l'aide d'un électret. Après une pré-charge du capteur à 6 V, les mesures ont été effectuées en mode autonome (aucune source de tension n'est connectée au système). La puissance convertie est comprise entre 61 nW et 100 nW, avec des vibrations extérieures à 250 Hz et une amplitude d'accélération de 0,25 g. Si l'on compare ces résultats avec la puissance disponible maximale calculée avec l'équation (6), elle n'est beaucoup plus faible. En fait, l'équation (6) ne prend en compte que le système mécanique, et comme un transducteur idéal sans tenir compte du mécanisme de transduction. Pour récupérer la puissance calculée par l'équation (6) par notre système, la tension initial devrait être d'environ 50 V. Cela montre que le principal problème réside au niveau de la tension de pull-in.

La puissance de notre convertisseur est inférieure aux chiffres qui se trouvent dans la littérature. Toutefois, une comparaison adéquate avec les travaux existants implique aussi une considération des autres facteurs : la taille, la tension de fonctionnement, etc… Par exemple, la puissance de 1,8 μW, rapportée par Yen a été obtenue avec une capacité d'aluminium de 6,6 cm de côté et à une fréquence de 1,5 kHz. Notre structure est 30 fois plus petite en surface, et fonctionne à une fréquence de 7 fois inférieure (qui est plus réaliste pour les applications en pratique). Donc, pour faire une comparaison adéquate de notre travail avec les autres dispositifs qui utilisent la transduction électrostatique, nous proposons une figure de mérite (FOM) qui est définie comme une puissance convertie normalisée :

$$FOM = \frac{P_h}{U^2 f A} \tag{17}$$

Où P_h est la puissance convertie, U est la tension maximale, f est la fréquence externe et A est la surface de la masse mobile. Le tableau 1 présente le calcul de ce FOM pour plusieurs dispositifs. Nous pouvons voir que notre travail a l'un des meilleurs facteurs de mérite. Mais

la puissance n'est pas assez importante pour alimenter un microsystème réel à cause de tension de pull-in très basse. Donc à l'avenir il faudra prendre en compte la tension de pull-in comme un paramètre principal pour l'amélioration du dispositif.

Author *[ref]*	*f* *(Hz)*	*A* *(mm²)*	*V* *(V)*	P_{conv} *(µW)*	*FOM* *(10^8µW/(mm²HzV²))*
Despesse [7]	50	1800	120	1050	81
B. Yen [18]	1560	4356	6	9,47	3,87
Ma [22]	4100	25.9	15 E*	0,065	0,27
Suzuki [23]	37	900	450 E*	0,28	0,0034
This work	250	66	8	0,061	5,68

E avec Electret*

Tableau 1. Comparaison de différents dispositifs utilisant FOM

Référence :

[1] Jean-Christophe Eloy, "MIS-07 Status of the MEMS industry", Yole development report, latest update June 2007

[2]R. Amirtharajah *et al.,* "Self-Powered Signal Processing Using Vibration-Based Power Generation", *Proc. of IEEE Journal of Solid-State Circuits,* vol. 33, no. 5, May 1998, *pp. 687-695*

[3] Paradiso *et al.,* "Energy scavenging for mobile and wireless electronics", *Pervasive computing,* pp. 18-27, 2005

[4] P. Basset *et al.*, "Chip-size antennas for implantable sensors and smart dusts", *Proc. of Transducers'05*, Seoul, Korea, 2005

[5] Shadrach Joseph Roundy, "Energy Scavenging for Wireless Sensor Nodes with a Focus on Vibration to Electricity Conversion", PhD thesis, 2003, University of California Berkeley

[6] Warneke *et al.,* "Exploring the Limits of System Integration with Smart Dust", *Proc. of IMEC'02*, New Orleans, USA, 2002

[7] G. Despesse *et al.,* "Fabrication and Characterization of High Damping Electrostatic Micro Devices for Vibration Energy Scavenging", *Proc. of DTIP'05*, pp. 386-390, 2005

[8] Jesse Depriest, "Aircraft Engine Attachment and Vibration Control", *Lord Library of Technical Articles*, LL-6505

[9] http://www.mellesgriot.com/pdf/CatalogX/X_31_3-7.pdf, "Sources of Vibration", *Catalogue on Fundamentals of vibration isolation*, pp. 31.3-31.7

[10] S. P. Beeby *et al.,* "Energy Harvesting Vibration Sources for Microsystems Applications", *Review Article Proc. of Measurement Science and Technology (IOP),* pp.R175-R195, 2006

[11] Paul D. Mitcheson *et al.,* "Architectures for Vibration-Driven Micropower Generators", *Proc. of Journal of Microelectromechanical Systems,* vol. 13, no. 3, June 2004, pp. 429-440

[12] C. B. Williams and R. B. Yates, "Analysis of a micro-electric generator for Microsystems*", Sens. and Act. A: Phys.,* Vol. 52, No 1, pp. 8-11, 1996

[13] A. Mahmood Paracha *et al.,* "MEMS DC/DC converter for 1D and 2D vibration-to-electricity power conversion", Transducers 2009, pp. 2098-2101, 2009

[14] M. Marzencki *et al.*, "Design and fabrication of piezoelectric micro power generators for autonomous microsystems", *Proc. of DTIP'05*, pp. 299-302, 2005

[15] Wang L, Yuan FG, "Energy harvesting by magnetostrictive material (MsM) for powering wireless sensors in SHM", *SPIE Smart Structures and Materials & NDE and Health Monitoring, 14th International Symposium (SSN'07)*, 2007

[16] S. Meninger *et al.*, "Vibration-to-electric energy conversion", *IEEE Trans. on VLSI*, vol. 9, no. 1, pp. 64-76, 2001

[17] S. Roundy *et al.*, "Micro-electrostatic vibration-to-electricity converters", *Proc. of IMEC'02*, New Orleans, USA, 2002

[18] B. C. Yen, H. L. Jeffery, "A variable capacitance vibration-to-electric energy harvester", *IEEE trans. on circuits and systems*, vol. 53, no. 2, *pp. 288-295* Feb. 2006,.

[19] D. Galayko, *et al.*, "AMS modeling of controlled switch for design optimization of capacitive vibration energy harvester", *Proc. of IEEE Int. Behavioral Modeling and Simulation Conf. (BMAS'07),* pp. 115-120, 2007

[20] A. Mahmood Paracha *et al.*, "A MEMS DC/DC Converter for autonomous vibration-to-electrical energy harvester", *Trans. on Electron Device Letters*, Vol-30, no.5, pp. 481-483, 2009

[21] T. Tsutsumino, Y. Suzuki, N. Kasagi, Y. Sakane, "Seismic Power Generator Using High-Performance Polymer Electret", *Proc. of MEMS '06*, pp. 98-101, 2006

[22] W. Ma, R. Zhu, L. Rufer, Yitshak Zohar, M. Wong, An Integrated Floating-Electrode Electric Microgenerator, *IEEE J. of MEMS*, vol. 16 no. 1, 2007

[23] Y. Suzuki, M. Edamoto, N. Kasagi, K. Kashwagi, Y. Morizawa, "Micro Electrets Energy Harvesting Device with Analogue Impedance Conversion Circuit", *Proc. of PowerMEMS'08*, pp. 7-10, 2008

Résumé

Les micro-technologies utilisées pour la réalisation des micro-capteurs ont permis grâce à un effet d'échelle, une réduction drastique de la consommation d'énergie électrique ; ceci a contribué à faire émerger le concept de capteurs autonomes qui ont la capacité de puiser l'énergie nécessaire à leur fonctionnement à partir de l'environnement dans lequel ils se trouvent. Parmi les sources d'énergie envisageables, notre choix s'est porté sur les vibrations mécaniques ambiantes. La conversion électromécanique est effectuée au sein d'un transducteur intégré dans une microstructure mécanique. Dans ce travail, nous avons conçu et réalisé un transducteur électrostatique utilisant une technologie qui a nécessité le développement d'un procédé *ad hoc* de gravure DRIE. Le dispositif a été testé expérimentalement et nous avons obtenu une conversion d'énergie mécanique en énergie électrique correspondant à une puissance de 61 nW, au moyen d'un dispositif dont la surface est de seulement 66 mm². Ce dispositif est le premier convertisseur miniature d'énergie en silicium basé sur une transduction électrostatique et sans l'adjonction d'un électret.
Mots clés : Transduction électrostatique, Power MEMS, récupération de l'énergie, IPOP, Pompe de charge

Summary

Due to size effects, the microtechnologies that are used to manufacture micro-sensors, allowed a drastic reduction of electrical power consumption. This feature contributed to the emergence of the concept of autonomous sensors, which have the ability to take the energy needed for their operation from the environment where they are located. Among the different energy sources, our choice was made on ambient mechanical vibrations. The electromechanical conversion is done within a transducer integrated with a micromechanical structure. In this work, we have designed and fabricated an electrostatic transducer based on silicon-glass technology, which required the development of a dedicated deep etching process. The device was tested experimentally and we have obtained a conversion of mechanical energy into electrical energy, corresponding to a power of 61 nW, with a device whose surface area is only 66 mm². This device is the first miniaturized silicon converter based on electrostatic transduction which does not use an electret.
Keywords: Electrostatic transduction, Power MEMS, Energy harvesting, IPOP, Charge pump circuit